SLAC-383
UC-414
(T/E)

MEASURING W PHOTON COUPLINGS IN A 500 GEV E+E- COLLIDER*

ERAN YEHUDAI

Stanford Linear Accelerator Center
Stanford University, Stanford, California 94309

August 1991

Prepared for the Department of Energy
under contract number DE–AC03–76SF00515

Printed in the United States of America. Available from the National Technical Information Service, U. S. Department of Commerce, 5285 Port Royal Road, Springfield, Virginia 22161. Price: Copy A05, Microfiche A01.

⋆ Ph.D. thesis

Abstract

The Standard Model gives definite predictions for the W-photon couplings. Measuring them would test an important ingredient of the model. In this work we study the capability of a 500 GeV e^+e^- collider to measure these couplings.

We study the most general C and P conserving $WW\gamma$ vertex. This vertex contains two free parameters, κ and λ. We look at three processes: $e^+e^- \to W^+W^-$, $e\gamma \to W\nu$ and $\gamma\gamma \to W^+W^-$. For each process we present analytical expressions of helicity amplitudes for arbitrary values of κ and λ.

We consider three different sources for the initial photon(s). The first two are breamsstrahlung and beamstrahlung (photon radiation induced by the collective fields of the opposite bunch). Both occur naturally in the collider environment. The third is a photon beam generated by scattering low energy laser light off a high energy electron beam.

We examine potential observables for each process, calculating their sensitivity to κ and λ, and estimating the accuracy with which they can be measured. Assuming Standard Model values are actually measured, we present the region in the κ - λ plane to which the W couplings can be restricted with a given confidence level. We find that combining the three processes, one can measure κ and λ with accuracy of 0.01-0.02.

Acknowledgments

With great pleasure, I would like to express my gratitude to the people who have made this work possible and my years at Stanford enjoyable.

To my advisor, Michael Peskin, who had an answer (or, at least, a reference) to each of my questions, for his help and encouragement, and for demonstrating what being a physicist is really all about.

To the members of the SLAC community, past and present, with whom I have had many fruitful discussions: Dick Blankenbecler, Dave Burke, Yossi Nir, Tim Barklow and my fellow students Claudio Dib, Russel Kauffman, Dan Schroeder, Steve Selipsky, Yael Shadmi, Matt Strassler and Andreas Weigend.

To Alex Hsieh, for his hard work and for coming up with the name HIP.

To Yossi Friedman and Marvin Weinstein, for teaching me, through many enthusiastic conversations, much of what I know about computers.

To my parents, Moshe and Atara, and my sisters, Rinat and Ella, who want the best for me, yet always supported the choices I have made.

To my son, Bar, who reminds me daily that there is more to life than work.

And, above all, to my wife, Maya, who suspended her own career to come with me to Stanford, for providing me with friendship, encouragement, support and love.

Table of Contents

1. Introduction

The Standard Model is widely accepted as the framework of contemporary high-energy physics. The spinor-vector couplings of the theory have been rigorously tested and verified. The vector-vector couplings, however, have hardly been subject to direct experimental test so far.[1] The vector-vector couplings are completely determined within the Standard Model. Measuring their value is one of the most important tasks of the next generation of high energy colliders.

An important role in this task will be played by e^+e^- colliders, which have always been invaluable in making precision high-energy measurments. In this thesis, we present a complete analysis of the constraints on the $W\gamma$ couplings possible from an e^+e^- collider. We concentrate on a particular design, NLC, currently under extensive study.

In this introduction we outline the major points discussed in the thesis. We start with the theory of $W\gamma$ couplings. Next we discuss current and future bounds on these couplings. In sect. 1.3 we briefly introduce the experimental setting. Sect. 1.4 deals with the three processes we consider. In sect. 1.5 we discuss in general terms the observables associated with the different processes. We conclude the introduction with an outline of the rest of the thesis.

1.1 W Couplings — theoretical considerations

In this section we outline some theoretical considerations regarding the $WW\gamma$ vertex. We discuss C and P transformations, scale dependence and imaginary components in the various couplings. We give the simplifying assumptions used in this work. Finally we discuss the expected values of the various couplings in the Standard Model and in a few other models.

The three vector vertex WWV, V being either γ or Z, has been thoroughly studied.[2] The vertex receives contributions from seven independent terms in the

Lagrangian.* Of these terms, three conserve both C and P, one violates both C and P but conserves CP, and three violate CP. The CP violating terms are not expected to receive significant radiative corrections in the Standard Model. Stringent bounds can be imposed on these parameters due to the smallness of CP violation observed in low energy physics. The fermion sector of the Standard Model violates C and P separately. It is, therefore, not surprising that fermionic loop corrections induce C and P violation in the boson sector.[3] In this work, however, we do not consider this C and P violating term.

One of the three C and P conserving terms in the $WW\gamma$ interaction is fixed by the W charge renormalization. The remaining two terms are written in terms of the parameters κ and λ. In the Standard Model, $\kappa = 1$ and $\lambda = 0$ at the tree level. κ and λ are related to the W magnetic dipole moment and electric quadrupole moment. We deal mainly with the $WW\gamma$ vertex. At some points we also need to refer to the WWZ vertex. In these cases we use κ_z and λ_z as the analogues of κ and λ.

Coefficients of individual Lorentz structures in the vertex function are called form factors. To first order in a weakly coupled theory such as the Standard Model, there is a simple tree-level relation between κ and λ and the form factors with which actual cross section calculations are carried out. It is clear on general principles that the $WW\gamma$ form factors must have a non-trivial momentum dependence. One must be very cautious when measuring their values, or even comparing potential bounds, at different energy scales.

Only the Standard Model values of the $WW\gamma$ couplings preserve tree level unitarity. In order for loop corrections not to violate unitarity, they have to drop like $1/s$ at asymptotically high energies. However, this is an asymptotic result, which need only start at energies higher than the mass of the most massive particle running in the loops.

$\star$ We neglect the scalar component of all vector bosons: $\partial_\mu V^\mu = 0$, $\partial_\mu W^\mu = 0$. This condition is automatic for on-shell particles, and holds for virtual vectors if we ignore the fermion masses.

The imaginary parts of the form factors are essentially the absorptive part of the $WW\gamma$ vertex function. Such effects are proportional to small coupling constants in a weakly coupled theory such as the Standard Model. However, they can be substantial if the W boson is strongly interacting in the relevant energy scale. Further, this energy scale must be such that new, strongly interacting particles can be created on-shell. We expect that in this case, the entire experimental picture is dramatically affected.

In this work, we make several simplifying assumptions. First, we only consider the two C and P conserving terms κ and λ. Second, we concentrate on $W\gamma$ rather than WZ couplings. WZ couplings inevitably enter the process $e^+e^- \to W^+W^-$ which we examine here. In that case, we make the working assumptions $\kappa_z = 1$ and $\lambda_z = \lambda$, which are suggested from low energy experiments.[4] All the experiments we consider run at, or below, 500 GeV. We assume the underlying scale of new physics is significantly higher, so that we can ignore the scale dependence of κ and λ. We also ignore the small Standard Model contributions to the imaginary component of κ and λ.

Couture and Ng[5] have calculated the loop corrections to the W anomalous couplings in the Standard Model, including the effects of a heavy top quark. The results depend both on the top quark and Higgs boson masses. For a heavy top quark ($m_t > m_Z$), this dependence is not steep. Neither κ nor λ are very sensitive to the Higgs boson mass. For a Higgs mass of 500 GeV and top mass of 150 GeV, the corrections are $\Delta\kappa = 5.5 \times 10^{-3}$ and $\lambda = 8.5 \times 10^{-5}$. It should be stressed that these corrections were calculated with all three bosons on-shell. At asymptotically high energies, one expects these corrections to drop as $1/s$. Some extensions of the Standard Model which do not significantly increase these corrections include two-Higgs-doublet models[6] and supersymmetry.[7]

Some "new physics" scenarios consistent with low-energy experiments do, however, suggest significant deviations from the Standard Model tree level values. These include composite W's[8] and non-decoupling effects of heavy quark loops.[3]

Composite W models can give particularly large corrections to the W couplings. These corrections are typically scale dependent, and become large at scales approaching the scale of compositeness.

1.2 W Couplings — bounds

Next we outline some of the major sources of bounds on $WW\gamma$ couplings. Current bounds are derived from unitarity considerations, loop effects on low energy experiments and, recently, CDF data. We also outline the bounds that can be extracted from experiments in future colliders.

A theory differing from the Standard Model only in the value of the W couplings violates unitarity at high energy unless the anomalous couplings drop to their Standard Model value fast enough at high energies. Assuming fixed couplings, one can calculate the maximal allowed deviation from the Standard Model such that unitarity is not violated below some scale Λ. This is the unitarity bound, and it is based entirely on theoretical considerations. For $\Lambda = 1$ TeV, the bounds on $\Delta\kappa = \kappa - 1$ and λ are of order 1.[9,4]

Fixing the anomalous couplings, one can also calculate their effect on low energy experiments through loops involving the W boson. As the theory with anomalous couplings is necessarily non-renormalizable, one has to explicitly cutoff the loop integral at some energy scale Λ. The result of the calculation typically depend not only on Λ, but also on the method used for cutting off the integral. With few exceptions, low energy experiments also give bounds of order 1 for $\Lambda =$ 1 TeV.[4,10–12]

On shell W production at the Tevatron allowed, for the first time, to impose scale independent bounds on $\Delta\kappa$ and λ. Due to low statistics, these bounds are very weak, of order 10.[1] With a luminosity upgrade, these bounds can be significantly improved.[13]

A major improvement on the Tevatron results is expected when the Large Electron Positron facility (LEP) II starts producing W pairs through $e^+e^- \rightarrow$

W^+W^-. Several authors have calculated that bounds of order 0.4-1.0 on the W couplings can be expected from these experiments.[15,16,14]

Several authors considered measuring the W couplings in lepton-hadron colliders.[17,18] HERA, with a center of mass energy of about 300 GeV is not very sensitive to κ and λ. In the LEP-LHC collider, however, a center of mass energy of 1.4 TeV allows relatively sensitive bounds, of order 0.1-0.2, on both couplings.

The Superconducting Super Collider (SSC) offers a very powerful tool for examining W interactions at very high energies. The complex environment of a hadron collider makes precision measurements difficult. Due to the s/m_W^2 enhancement the total cross section for $q\bar{q}' \to W\gamma$ very sensitive to λ, less so to $\Delta\kappa$. Bounds of order 0.01 for λ and 0.1 for κ are possible from that process.[4,19] Because of the possible scale dependence of the W couplings, one should be cautious when comparing SSC bounds with those of lower energy machines.

1.3 Experimental Setting

In this section we discuss the experimental setting considered in this work. We describe the underlying e^+e^- collider and the various photon spectra used.

In this work we concentrate on a machine design commonly termed the Next Linear Collider (NLC).[20,21] NLC is a linear e^+e^- collider with center of mass energy of 500 GeV. We assume an integrated luminosity of 9 fb^{-1} $= 3000R^{-1}$.

Radiated photons play a very important role in high energy electron colliders. We consider three potential sources of photons. Any e^+e^- collision exhibits a radiated photon spectrum through bremsstrahlung. This radiation depends only on the electron energy. It is approximated to first order by the Weizsacker-Williams distribution.

In high-energy linear colliders with very small spot size, a different mechanism accounts for what is potentially an even more important source of photons. As the electrons of one beam are passing through the other beam, they experience

a very strong electromagnetic field. The synchrotron radiation induced by that field is called "beamstrahlung".[22,23] The actual beamstrahlung spectrum depends sensitively on machine parameters. We work with one particular set of parameters that nearly maximizes this effect.[23]

Ginzburg *et al.*[24,25] have suggested a scheme for converting a single-pass e^+e^- collider into an $e\gamma$ or $\gamma\gamma$ collider. The conversion of high-energy electrons to photons is done by backward Compton scattering of high intensity laser light off the electron beams. This mechanism entails loosing very little luminosity; it reduces the center of mass energy by 20-30%. In such a $\gamma\gamma$ collider built on top of a 500 GeV e^+e^- collider, the average center of mass energy is about 350 GeV.

1.4 Processes

We examine in detail three processes: $e^+e^- \to W^+W^-$, $e\gamma \to W\nu$ and $\gamma\gamma \to W^+W^-$. The first is the traditional W pair production $e^+e^- \to W^+W^-$.[2] In the Standard Model, unitarity is maintained by a delicate cancellation between the t-channel neutrino exchange and the s-channel annihilation diagrams. Only the latter involves three vector boson couplings. Due to this cancellation, the process is particularly sensitive to deviations from the Standard Model. That makes it a powerful tool for exploring new physics. One disadvantage of $e^+e^- \to W^+W^-$ is that it involves both $W\gamma$ and WZ couplings. Separating the effects of the two channels is not easy.

A different process occurring at NLC is $e^+e^- \to W^+e^-\overline{\nu}$. The amplitude for this process is dominated by the diagram in which the positron emits a collinear, almost on-shell photon. In that case, the positron is likely to escape detection by going down the beam pipe. The cross section in this case can be approximated by that of the reaction $e\gamma \to W\nu$. While the complete calculation of the entire process is essential for comparison with actual experimental results, it is not crucial for estimating the process' sensitivity to anomalous couplings. The simpler $e\gamma \to W\nu$ is the second process we consider. The process $e\gamma \to W\nu$ has several advantages

that make it an important complement to $e^+e^- \to W^+W^-$.[26–29] First, it only involves $W\gamma$ couplings, avoiding the complications associated with separating Z and γ couplings. Second, its total cross section approaches a constant rather than dropping like $1/s$. Even at NLC energies it has a very large cross section, allowing excellent statistics even with modest integrated luminosity. Finally, since the W decays to a muon and a neutrino, the experimental signature is extremely simple — a single muon scattering against nothing. Backgrounds for this signature are virtually nonexistent.

The third process we consider is W pair production via photon fusion, $\gamma\gamma \to W^+W^-$.[26,30,31] The $\gamma\gamma$ luminosity in an ordinary e^+e^- collider is small for high energy photons. The process can better be utilized in the setting of a dedicated $\gamma\gamma$ collider. In such a collider, $\gamma\gamma \to W^+W^-$ is one of the dominant processes. Like $e\gamma \to W\nu$, it only involves $W\gamma$ couplings. But unlike the two previous processes, $\gamma\gamma \to W^+W^-$ also involves the four vector vertex $WW\gamma\gamma$. That vertex has not been fully analyzed. In this work we use its simplest form which still consistent with arbitrary values for κ and λ. In order for the process to satisfy the electromagnetic Ward identity, the $WW\gamma\gamma$ vertex has to depend on λ in a form first suggested (for different reasons) by Aronson.[32]

1.5 Observables

In this section we consider in general terms some of the observables associated with the different processes. These include the total cross section, the angular distribution, the ratio between longitudinal and transverse W production and asymmetries associated with photon polarization. Finally, we outline the method used to calculate potential bounds.

The total cross section, with minimal cuts, is a simple, yet very sensitive measure for anomalous couplings. Measuring the total cross section requires knowledge of the total luminosity, as well as backgrounds, triggering and detector efficiencies. Systematic errors in this measurement are relatively large. Many of these errors

are canceled by measuring the ratio of different cross sections. One such ratio is the forward-backward asymmetry. Another, which we call IO is the 'in/out' ratio between production at low and high values of $|\cos\theta|$.

One of the most sensitive measures to the anomalous couplings is the ratio between longitudinal and transverse W polarizations. By the equivalence theorem, in the high energy limit, the longitudinal W degree of freedom behaves like the Higgs Goldstone boson it absorbed. As such, its interactions are more sensitive to anomalous behavior originating in the Higgs sector. More generally, it is the (s/m_W^2)-like term in the longitudinal polarization vector which has particularly 'bad' high energy behavior. In the Standard Model, delicate cancellations prevent that bad behavior. Any deviation from Standard Model couplings potentially violates these cancellations, increasing dramatically the total cross section for longitudinal W production.

Both $e^+e^- \to W^+W^-$ and $\gamma\gamma \to W^+W^-$ allow the determination of the direction of one W's decay products with respect to the W direction of motion. This can be done most easily in semi-leptonic decay events, *i.e.* events in which one W decays leptonically, while the other decays hadronically. Summing the visible momentum in the hadronic showers gives the total momentum of the W. Comparing the direction of the charged lepton to the direction of the hadronically decaying W, one can calculate the leptonic decay direction in the W center of mass frame. From that angular distribution, one can extract the ratio between transverse and longitudinal W production.

Table 1 compares the three processes we examine in this work in terms of their advantages and disadvantages as probes of the W anomalous couplings.

It has been suggested that precision analysis of experimental data should be done by direct fitting to the theory.[33] However, in this work we only try to assess the general sensitivity one can expect in future experiments. The method we use is as follows. We calculate the theoretical expectation value of various observable (*e.g.* total cross section or forward-backward asymmetry) as a function of κ and

Table 1. Advantages and disadvantages of the three processes.

	Advantages	Disadvantages
$e^+e^- \to W^+W^-$	• Particularly sensitive due to SM cancellations. • W polarization can be extracted.	• Both $W\gamma$ and WZ couplings are involved. Separating their different effects can be difficult. • Relatively small cross section.
$e\gamma \to W\nu$	• Large cross section allows good statistics with modest luminosity. • Simple experimental signature, with very little background.	• Relatively insensitive to anomalous couplings. • W direction is not reconstructible in leptonic decays.
$\gamma\gamma \to W^+W^-$	• Anomalous couplings enter twice, increasing sensitivity. • In an dedicated $\gamma\gamma$ collider, photon polarization adds important information. • W polarization can be extracted.	• Involves the four vector vertex, complicating analysis. • Cross section small in traditional e^+e^- collider. Requires a dedicated $\gamma\gamma$ collider.

λ. Then, we give a very rough estimate of the experimental precision with which one can expect to measure the same observable. We mainly consider systematic errors. The cross sections of all the processes involved are large, and systematic errors usually out-weigh statistical ones. Finally, assuming Standard Model values are actually *measured*, we estimate what bounds can be extracted on the values of the anomalous couplings.

1.6 Outline

This dissertation proceeds as follows. Chapter 2 examines in detail the W couplings. We present the complete Lagrangian and derive an expression for the vertex. We then examine other bounds on the W anomalous couplings, from

unitarity considerations, low energy experiments, and potential bounds from other high-energy experiments.

Chapter 3 concentrates on W pair production via $e^+e^- \to W^+W^-$. We start with a detailed derivation the helicity amplitudes for the process. Next we examine which quantities are experimentally observable, estimate the accuracy with which they can be measured, and calculate their dependence on κ and λ. We discuss the principles used for extracting bounds on the anomalous couplings, and finally present these bounds.

Chapter 4 follows a similar route analyzing the single W production $e\gamma \to W\nu$. After deriving expressions for the helicity amplitudes, we discuss the three photon sources mentioned above: bremsstrahlung, beamstrahlung and Compton backscattered laser light. The effective luminosity and its use in calculating cross sections are discussed. We use the effective luminosity to calculate experimental observables, and extract from them potential bounds on κ and λ.

Chapter 5 deals with W pair production via photon fusion, $\gamma\gamma \to W^+W^-$. The chapter follows much of the same steps of the previous two, deriving expressions for the helicity amplitudes, using the effective luminosity to calculate observables and extracting from them potential bounds on κ and λ. We present our conclusions in chapter 6.

Results for all the calculations are presented as helicity amplitudes. For processes involving fermions this is conveniently done using the 'Vector-Equivalence' technique which provides simple *analytic* matrix element level expressions. This technique is described in appendix A. All the calculations presented here were assisted by HIP[34] — a set of packages for performing high-energy calculations using *Mathematica*.[35] *Mathematica* is a program for performing mathematical calculations, both symbolic and numeric, on the computer. HIP is described in detail in appendix B.

2. Anomalous Couplings

In this chapter we discuss the anomalous couplings in the $WW\gamma$ vertex. In the first section we present the most general Lagrangian for the $WW\gamma$ vertex. The Feynman rule for the vertex is derived. The discussion follows closely sect. 2 of the very useful paper of Hagiwara, Hikasa, Peccei and Zeppenfeld.[2] Our presentation is slightly more general in that we do not consider any particular kinematics. We then restrict ourselves to the C and P conserving components of the vertex.

In the second section we discuss current bounds on κ and λ. Until very recently, two sources for these bounds were generally available: theoretical unitarity bounds and low energy experiments in which the vertex appears in loop corrections. Samuel *et al.* have analyzed results from CDF to give the first tree level (albeit very weak) bounds on κ and λ.[1]

The third section outlines the potential of other high-energy colliders. The colliders under consideration are lower energy e^+e^- colliders (LEP-II), high-energy hadron colliders (SSC and LHC) and electron-proton colliders (HERA and LEP-LHC).

2.1 Lagrangian and definitions

The general coupling of two charged vector bosons with a neutral vector bosons can be derived from the following effective Lagrangian:[2]

$$\begin{aligned}\mathcal{L}_{WWV} = ig_V\Big[&g_1^V(W^\dagger_{\mu\nu}W^\mu V^\nu - W^\dagger_\mu V_\nu W^{\mu\nu}) + \kappa_V W^\dagger_\mu W_\nu V^{\mu\nu} + \frac{\lambda_V}{m_W^2}W^\dagger_{\lambda\mu}W^\mu{}_\nu V^{\nu\lambda}\\ &-g_4^V W^\dagger_\mu W_\nu(\partial^\mu V^\nu + \partial^\nu V^\mu) - ig_5^V\varepsilon^{\mu\nu\rho\sigma}(W^\dagger_\mu \overleftrightarrow{\partial_\rho} W_\nu)V_\sigma\\ &+\tilde{\kappa}_V W^\dagger_\mu W_\nu \tilde{V}^{\mu\nu} + \frac{\tilde{\lambda}_V}{m_W^2}W^\dagger_{\lambda\mu}W^\mu{}_\nu\tilde{V}^{\nu\lambda}\Big],\end{aligned} \tag{2.1}$$

where V stands for either the photon ($V=\gamma$) or the Z ($V=Z$) fields, W is the W^- field, $A_{\mu\nu} = \partial_\mu A_\nu - \partial_\nu A_\mu$, $\tilde{V}_{\mu\nu} = \frac{1}{2}\varepsilon_{\mu\nu\rho\sigma}V^{\rho\sigma}$, and $(A\overleftrightarrow{\partial_\mu}B) = A(\partial_\mu B) - (\partial_\mu A)B$.

The seven operators in (2.1) exhaust all possible Lorentz structures if we neglect the scalar components of all vector bosons: $\partial_\mu V^\mu = \partial_\mu W^\mu = 0$. This condition is satisfied automatically for on-shell W's and Z's and for both real and virtual photons. If a virtual W or a Z couples to a fermion line, the scalar component is proportional to the mass of the fermion. In the processes we consider, the term is of order the mass of the electron, and we may safely neglect it.

The corresponding Feynman rule with momenta as in fig. 1 is[2]

$$\begin{aligned} i\Gamma_V^{\alpha\beta\mu}(q,\overline{q},P) = ig_V \Big[& f_1^V (q-\overline{q})^\mu g^{\alpha\beta} - \frac{f_2^V}{m_W^2}(q-\overline{q})^\mu P^\alpha P^\beta + f_3^V (P^\alpha g^{\mu\beta} - P^\beta g^{\mu\alpha}) \\ & + i f_4^V (P^\alpha g^{\mu\beta} + P^\beta g^{\mu\alpha}) + i f_5^V \varepsilon^{\mu\alpha\beta\rho}(q-\overline{q})_\sigma \\ & - f_6^V \varepsilon^{\mu\alpha\beta\rho} P_\sigma - \frac{f_7^V}{m_W^2}(q-\overline{q})^\mu \varepsilon^{\alpha\beta\rho\sigma} P_\rho (q-\overline{q})_\sigma \Big]. \end{aligned} \tag{2.2}$$

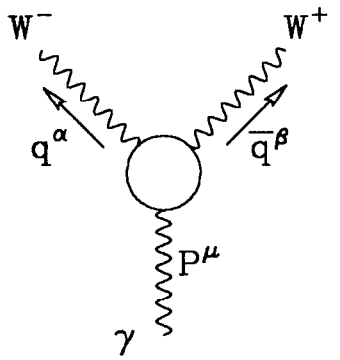

Figure 1. The general WWV vertex.

All the form factors f_i^V are dimensionless functions of P^2, q^2 and $\overline{q}^2$. To lowest

order, the form factors are related to the Lagrangian parameters via

$$
\begin{aligned}
f_1^V &= g_1^V + \frac{P^2}{2m_W^2}\lambda_V, & f_2^V &= \lambda_V, \\
f_3^V &= g_1^V + \kappa_V + \frac{q^2+\overline{q}^2}{2m_W^2}\lambda_V, & & \\
f_4^V &= g_4^V - \frac{q^2-\overline{q}^2}{2m_W^2}i\lambda_V, & f_5^V &= g_5^V + \frac{q^2-\overline{q}^2}{2m_W^2}i\tilde{\lambda}_V, \\
f_6^V &= \tilde{\kappa}_V - \frac{q^2+\overline{q}^2}{2m_W^2}\tilde{\lambda}_V, & f_7^V &= -\frac{1}{2}\tilde{\lambda}_V.
\end{aligned}
\tag{2.3}
$$

Contributions from higher dimensional operators in the Lagrangian give a P^2, q^2 and $\overline{q}^2$ dependence of the form factors. The form factors are real for $P^2 < 0$, $q^2 < 0$ or $\overline{q}^2 < 0$. The form factors may have imaginary parts above threshold.

Without losing generality, we fix the overall coupling constants to be

$$g_\gamma = -e, \qquad g_Z = -e\cot\theta_W, \tag{2.4}$$

where $-e$ is the electron charge and θ_W is the weak mixing angle. The W charge determines $g_1^\gamma = 1$. κ_γ and λ_γ are related to the magnetic dipole moment μ_W and electric quadrupole moment Q_W of the W^+ by

$$\mu_W = \frac{e}{2m_W}(1+\kappa_\gamma+\lambda_\gamma), \qquad Q_W = -\frac{e}{m_W^2}(\kappa_\gamma-\lambda_\gamma). \tag{2.5}$$

The three couplings g_1, κ and λ are even under both C and P transformation.

Two couplings, $\tilde{\kappa}$ and $\tilde{\lambda}$, conserve C but violate P. They are related to the electric dipole moment d_W and the magnetic quadrupole moment $\tilde{Q}_W$ of the W^+ by

$$d_W = \frac{e}{2m_W}(\tilde{\kappa}_\gamma+\tilde{\lambda}_\gamma), \qquad \tilde{Q}_W = -\frac{e}{m_W^2}(\tilde{\kappa}_\gamma-\tilde{\lambda}_\gamma). \tag{2.6}$$

The remaining two couplings of eqn. (2.1), g_4 and g_5, violate C. g_4 respects P

Table 2. Properties of the couplings of eqn. (2.1) under C and P.

	P	C	CP
g_1, κ, λ	+	+	+
$\tilde{\kappa}$, $\tilde{\lambda}$	−	+	−
g_4	+	−	−
g_5	−	−	+

whereas g_5 violates P and is thus CP conserving. The properties of the various couplings under C and P are summarized in table 2.

The imaginary parts of the form factors are essentially the absorptive part of the vertex function. Such effects are proportional to small coupling constants in a weakly interacting theory such as the Standard Model. A strongly interacting theory could contribute significantly to the imaginary parts, but only if new particles can be produced on-shell. In that event, the entire experimental picture is dramatically affected.

In this work we only consider the C and P conserving couplings g_1, κ and λ, though it should be noted that fermion loops contribute directly to g_5 as well. We also neglect the imaginary components of κ and λ.

2.2 Unitarity and low energy constraints

A $WW\gamma$ interaction Lagrangian with fixed, non Standard Model couplings violates unitarity at sufficiently high energies. Unitarity bounds on the value of the anomalous couplings are calculated by demanding the tree level unitarity is not violated below a fixed energy scale Λ. The assumption is that since the Lagrangian is a low energy effective approximation, there exists an underlying high energy theory which unitarizes amplitudes at the scale Λ. Baur and Zeppenfeld[9] give the bounds

$$|\Delta\kappa| < \frac{1.86}{\Lambda^2} \qquad \text{for} \quad \lambda = 0, \tag{2.7}$$

and

$$|\lambda| < \frac{0.99}{\Lambda^2} \qquad \text{for} \quad \kappa = 1, \tag{2.8}$$

where $\Delta\kappa = \kappa - 1$ and Λ is in TeV. Here and henceforth, we use κ and λ for κ_γ and λ_γ.

Most current experimental bounds on κ and λ arise from loop effects, because so far almost no particle accelerator possesses sufficient energy or luminosity to produce on-shell W's directly. The one exception is discussed below. If the $WW\gamma$ vertex deviates from its Standard Model value, the resulting theory is not renormalizable. Therefore, the theory is not fundamental, but rather is a low energy approximation of a more basic theory characterized by some (high) energy scale Λ. Results of loop calculations typically depend on that energy scale. The exact result also depends on the regularization scheme used in doing the loop integral. Since loop effects from different sources can interfere destructively, these estimates also assume that the non standard couplings are the only source of new physics in the loop diagram. Further, another basic assumption is that the value of the couplings is independent of the loop momentum. This assumption is particularly questionable in integrals dominated by the cutoff scale, which is also the scale of the physics giving rise to the anomalous couplings.

Some of the more stringent bounds derived from low energy experiments are the following: Calculating the effects of non Standard Model values for κ and λ on the $(g-2)$ factor of the muon, and comparing to current experimental results, Grau and Grifols get[10]

$$-2.09 < \Delta\kappa \log(\Lambda^2/m_W^2) - \lambda < 5.54. \tag{2.9}$$

Using $e^+e^- \to f\bar{f}$ cross-section data from PETRA, and taking $\lambda = 0$, van der Bij deduces[11]

$$|\Delta\kappa(\Lambda/m_W)| < 33. \tag{2.10}$$

Alcorta *et al.* rely[12] on results from the polarization asymmetry in e-D scattering

at SLAC, and taking $\lambda = 0$ again, give

$$\left|0.6\Delta\kappa - 0.4(\Delta\kappa)^2\right| < \frac{1}{\Lambda^2} \tag{2.11}$$

(Λ in TeV.)

Neutrino-nucleon scattering experiments give[4] strong correlation between κ and κ_Z:

$$\left|\Delta\kappa_Z + (\cos\theta_W^2 + \frac{1}{2})\Delta\kappa_Z^2 + \sin\theta_W^2\Delta\kappa^2\right| < 0.015\frac{m_W^2}{\Lambda^2}. \tag{2.12}$$

The allowed values form a narrow ellipse-shaped strip in the κ-κ_Z plane.

Data on the heavy boson mass ratio were used by Kane, Vidal and Yuan to strongly correlate[4] λ and λ_Z. They find (for $\Lambda = 1$ TeV) that one may approximately take $\lambda = \lambda_Z$ for $\lambda, \lambda_Z > 0.15$. This restriction enforces an approximate custodial SU(2) symmetry relating the $W^\pm$ and W^3 fields. A term of the form $\epsilon^{abc}W^a_{\mu\nu}W^{b\nu}_\tau W^{c\tau\mu}$ in the unbroken Lagrangian is explicitly custodial SU(2) symmetric. Expressed in terms of the γ and Z fields, in gives rise to the condition $\lambda = \lambda_Z$.

To summarize, the strongest independent bound on κ from low energy experiments is of order 100%, while the best result on λ is $|\lambda| < 0.6$ (eqn. (2.8)) coming from unitarity considerations.

2.3 Other high-energy bounds

In this section we discuss bounds from future high-energy colliders. Baur and Berger considered a luminosity upgrade of the Tevatron to 100 pb^{-1}.[13] Using the process $q\overline{q}' \to W\gamma$ they predict bounds of 1.1-1.5 on $|\Delta\kappa|$ and 0.38-0.47 on $|\lambda|$ (90% confidence limit).

The first significant on-shell W production in a e^+e^- collider is planned in LEP-II. With center-of-mass energy of 190-200 GeV, the collider is designed for precision study of the interaction $e^+e^- \to W^+W^-$. Hagiwara *et al.* examined

the process in detail, but gave only a brief discussion of potential bounds from LEP-II.[2] Kane, Vidal, and Yuan calculated the dependence of the total cross section on κ and λ, and assuming it can be measured to 10%, concluded the bounds $-0.54 < \Delta\kappa < 0.94$ and $|\lambda| < 0.5$. Zeppenfeld studied the sensitivity of the process to κ and κ_z, ignoring the couplings λ and λ_z.[16] His conclusion is that bounds of order 0.5 can be imposed on both $|\Delta\kappa|$ and $|\Delta\kappa_z|$. Argyres *et al.* considered the total cross section for $e^+e^- \to W^+W^-\gamma$.[15] In a 200 GeV e^+e^- collider, κ can be measured with accuracy of order 1.

Layssac *et al.* have studied a more complete set of observables associated with the process $e^+e^- \to W^+W^-$.[14] Two scenarios where studied for discovery limits. In the first, $\Delta\kappa = \Delta\kappa_z = 0$ and $\lambda = \lambda_z$ were chosen, and a 1σ bound $|\lambda| < 0.1$ was deduced. In the second scenario, the choices $\lambda = \lambda_z = 0$ and $\Delta\kappa = \Delta\kappa_z$ led to the potential bound $|\Delta\kappa| < 0.05$. In all cases, the authors assumed a uniform experimental accuracy of 3-4% on all integrated quantities. In the case of a 500 GeV collider, these bounds would improve by a factor of 3 to 4.

Baur and Zeppenfeld calculated the sensitivity of the process $eq \to eWq'$ in the context of an ep collider.[17] Two collider designs were considered. In HERA, a 30 GeV electron beam collides with an 800 GeV proton beam. In a proposed LEP-LHC collider, the corresponding energies are 60 GeV and 8 TeV. Assuming the standard WWZ vertex, bounds of order 0.5 (0.2) on $\Delta\kappa$ and 1.2 (0.1) on λ can be extracted with 90% confidence limit from the experiment at HERA (LEP-LHC). Zeppenfeld obtained slightly weaker potential bounds in the same colliders by considering the process $eq \to \nu\bar{q}'\gamma$.[18] This process has the advantage in that only $W\gamma$ and not WZ couplings contribute.

Baur and Zeppenfeld also carefully calculated the sensitivity of the process $q\bar{q}' \to W\gamma$ in the context of the very high energy hadron colliders SSC and LHC with center-of-mass energies of 40 and 20 TeV respectively. Since the process can occur with a wide range of energy scales, they use scale dependent anomalous

couplings, varying like

$$a(\hat{s}) = \frac{a_0}{(1+\hat{s}/\Lambda^2)^2}, \tag{2.13}$$

where $\hat{s}$ is the center-of-mass energy of the $q\overline{q}'$ system squared. Their bounds, therefore, depend on a choice for Λ. $\Lambda = 1$ TeV gives (with 99.99% confidence level) the bounds $|\Delta\kappa_0| < 0.26(0.34)$ and $|\lambda_0| < 0.039(0.054)$ for SSC (LHC). Kane, Vidal and Yuan used fixed couplings, resulting in much stricter bounds, of order 0.1 (0.2) for $\Delta\kappa$ and 0.01 (0.02) on λ in SSC (LHC).[4]

The bounds derivable from different future colliders are summerized in table 3. In comparing these results, it should be kept in mind that the various authors differ on several important points in their analysis. In sampling the multi-dimensional space of the various couplings, some authors fix all but one of the couplings, while others allow independent or partially independent variation of each coupling. Considering experimental errors, some authors consider only statistical errors, others include systematic errors. Typically, systematic errors of 5% in measuring total cross sections are used. The confidence limit (C. L.) used in calculating the bounds varies from 68% to 99.99%. Finally, while all authors consider the total cross section as one observable, some but not all also consider angular distributions.

Table 3. Bounds possible at different future colliders.

	Tevatron upgrade	LEP II	HERA (LEP-LHC)	SSC (LHC)
Type	$p\overline{p}$	e^+e^-	ep	$p\overline{p}$
C.M. Energy	1.8 TeV	190 GeV	314 (1400) GeV	40 (20) TeV
Process	$q\overline{q}' \to W\gamma$	$e^+e^- \to W^+W^-$	$eq \to eWq'$	$q\overline{q}' \to W\gamma$
Bounds: $\Delta\kappa$	1.3	0.7	0.5 (0.2)	0.26 (0.34)
λ	0.4	0.5	1.2 (0.1)	0.039 (0.054)
C. L.	68%	68%	90%	99.99%
References	13	2, 4, 14, 15	17, 18	4, 19

In conclusion, colliders scheduled for operation in the next decade or so can increase our sensitivity to κ to order 0.3, while measuring λ with accuracy of order 0.04.

3. $e^+e^- \rightarrow W^+W^-$

3.1 Introduction

$e^+e^- \rightarrow W^+W^-$ is undoubtedly the most thoroughly studied process occurring in an NLC-type collider. The reason is that this process offers a combination of reasonable statistics and particular sensitivity to unknown parameters both within and outside the Standard Model.

Analyzing the process $e^+e^- \rightarrow W^+W^-$ is complicated because both the photon and the Z couplings of the W are involved. For each neutral boson V, the number a priori independent C and P conserving parameters in WWV vertex is two. As both the photon and the Z take part in $e^+e^- \rightarrow W^+W^-$, the total number of parameters is four. To simplify the analysis, and allow comparison with other processes, we reduce this number to two by assuming

$$\kappa_Z = 0, \qquad \lambda_Z = \lambda_\gamma. \tag{3.1}$$

As we described in sect. 2.2, these assumptions are suggested by low energy experiments.[4] The constraint $\lambda_z = \lambda_\gamma$ also follows from custodial SU(2).

In the next section, we rederive expressions for the helicity amplitudes for this process. We then calculate the cross sections for creating W's of specific polarization. These cross sections cannot be measured directly, but give an insight into the physics of this process. Section 3 examines which quantities can actually be measured, and estimate the accuracy of these measurements. We calculate these observable quantities, estimating their sensitivity to κ and λ. In sect. 4 we discuss principles for estimating experimental bounds on κ and λ using data. We apply these principles to give the regions in the κ-λ plane corresponding to specific confidence limits.

The three Feynman diagrams contributing to $e^+e^- \to W^+W^-$ are shown in fig. 2.

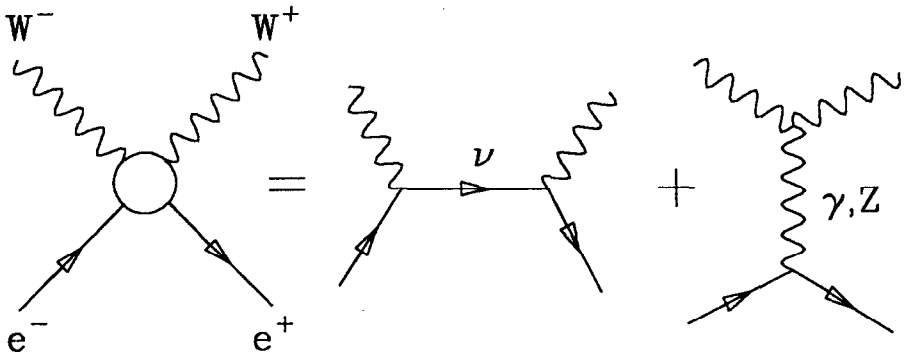

Figure 2. Feynman diagrams for $e^+e^- \to W^+W^-$.

With both W's on shell, and momenta labeled as in fig. 3, the general WWV vertex (2.2) takes the form

$$\begin{aligned} i\Gamma_V^{\tau\mu\nu} &= ig_V\Bigg[\left(1+\frac{s}{2m_W^2}\lambda_V\right)(p_3-p_4)^\tau g^{\mu\nu} - \frac{\lambda_V}{m_W^2}(p_3-p_4)^\tau p_3^\nu p_4^\mu \\ &\qquad + (1+\kappa_V+\lambda_V)(p_4^\mu g^{\nu\tau} - p_3^\nu g^{\mu\tau})\Bigg] \\ &= ig_V\Bigg[2\left(1+\frac{2\lambda_V}{r}\right)p_3^\tau g^{\mu\nu} - \frac{8\lambda_V}{rs}p_3^\tau p_3^\nu p_4^\mu \\ &\qquad + (1+\kappa_V+\lambda_V)(p_4^\mu g^{\nu\tau} - p_3^\nu g^{\mu\tau})\Bigg], \end{aligned} \tag{3.2}$$

where $g_\gamma = e$, $g_z = e\cot\theta_W$ and $r = 4m_W^2/s$.

As we ignore the electron mass, here and throughout this work, the electron and the positron have the same helicity. The matrix element for this process is

given by

$$\mathcal{M}_\sigma^{\lambda^-\lambda^+} = \mathcal{M}_\sigma^{\lambda^-\lambda^+}(\nu) + \mathcal{M}_\sigma^{\lambda^-\lambda^+}(\gamma) + \mathcal{M}_\sigma^{\lambda^-\lambda^+}(Z) \tag{3.3}$$

where σ is the electron helicity ($\sigma = 1(-1)$ corresponding to right (left) handed particles), λ^- and λ^+ are the helicities of the W^- and W^+ respectively,

$$\begin{aligned}
i\mathcal{M}_\sigma^{\lambda^-\lambda^+}(\nu) &= \varepsilon^{\mu*}(p_3,\lambda^-)\,\varepsilon^{\nu*}(p_4,\lambda^+)\overline{v}_\sigma(p_2)\left(\frac{ig}{\sqrt{2}}P_L\gamma_\nu\right)\frac{i(\not{p}_1-\not{p}_3)}{t} \\
&\quad\times\left(\frac{ig}{\sqrt{2}}P_L\gamma_\mu\right)u_\sigma(p_1) \\
&= \frac{-ie^2}{2t\sin^2\theta_W}\delta_{\sigma L}\overline{v}_L(p_2)\;\not{\varepsilon}^*(p_4,\lambda^+)(\not{p}_1-\not{p}_3)\;\not{\varepsilon}^*(p_3,\lambda^-)u_L(p_1) \\
\mathcal{M}_\sigma^{\lambda^-\lambda^+}(\gamma) &= \varepsilon^{\mu*}(p_3,\lambda^-)\,\varepsilon^{\nu*}(p_4,\lambda^+)\overline{v}_\sigma(p_2)(-ie\gamma_\alpha)u_\sigma(p_1)\left(\frac{-ig^{\alpha\tau}}{s}\right)(i\Gamma^\gamma_{\tau\mu\nu}) \\
&= \frac{-ie^2}{s}\,\varepsilon^{\mu*}(p_3,\lambda^-)\,\varepsilon^{\nu*}(p_4,\lambda^+)\overline{v}_\sigma(p_2)\gamma^\tau u_\sigma(p_1)\left(\frac{\Gamma^\gamma_{\tau\mu\nu}}{e}\right) \\
\mathcal{M}_\sigma^{\lambda^-\lambda^+}(Z) &= \varepsilon^{\mu*}(p_3,\lambda^-)\,\varepsilon^{\nu*}(p_4,\lambda^+)\overline{v}_\sigma(p_2)(ieg_\sigma\gamma_\alpha)\left(\frac{-ig^{\alpha\tau}}{s-m_Z^2}\right)(i\Gamma^Z_{\tau\mu\nu}) \\
&= \frac{ie^2\cot\theta_W g_\sigma}{s-m_Z^2}\,\varepsilon^{\mu*}(p_3,\lambda^-)\,\varepsilon^{\nu*}(p_4,\lambda^+)\overline{v}_\sigma(p_2)\gamma^\tau u_\sigma(p_1)\left(\frac{\Gamma^Z_{\tau\mu\nu}}{e\cot\theta_W}\right),
\end{aligned} \tag{3.4}$$

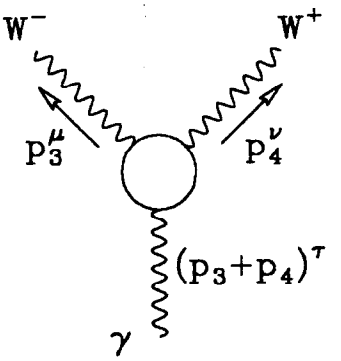

Figure 3. The WWV vertex for $e^+e^- \to W^+W^-$.

$\varepsilon^{\mu*}(p_3,\lambda^-)$ and $\varepsilon^{\nu*}(p_4,\lambda^+)$ are the polarization vectors of the W^- and W^+ respectively, $P_L = (1-\gamma_5)/2$, $s = (p_1+p_2)^2$, $t = (p_1-p_3)^2$, and eg_σ is the Z-electron coupling:

$$g_\sigma = \frac{\sin\theta_W}{\cos\theta_W} - \frac{\delta_{\sigma L}}{2\sin\theta_W\cos\theta_W} \tag{3.5}$$

In the e^+e^- center-of-mass frame, the momenta in the process take the following values:

$$\begin{aligned} p_1 &= \frac{\sqrt{s}}{2}(0,0,1,1) \qquad & p_3 &= \frac{\sqrt{s}}{2}(\beta\sin\theta,0,\beta\cos\theta,1) \\ p_2 &= \frac{\sqrt{s}}{2}(0,0,-1,1) \qquad & p_4 &= \frac{\sqrt{s}}{2}(-\beta\sin\theta,0,-\beta\cos\theta,1) \end{aligned} \tag{3.6}$$

where $\beta = \sqrt{1-r}$. The W polarization vectors are:

$$\begin{aligned} \varepsilon^*(p_3,\pm) &= \frac{1}{\sqrt{2}}(\cos\theta,\pm i,-\sin\theta,0) \qquad & \varepsilon^*(p_4,\pm) &= \frac{1}{\sqrt{2}}(\cos\theta,\mp i,-\sin\theta,0) \\ \varepsilon^*(p_3,0) &= \frac{1}{\sqrt{r}}(\sin\theta,0,\cos\theta,\beta) \qquad & \varepsilon^*(p_4,0) &= \frac{1}{\sqrt{r}}(-\sin\theta,0,-\cos\theta,\beta). \end{aligned} \tag{3.7}$$

In evaluating the spinor expressions, let us define a four vector

$$v_\pm = \mathcal{V}_\pm(p_2,p_1) = \sqrt{s}(1,\mp i,0,0) \tag{3.8}$$

(see Appendix A). We then have the following useful identities:

$$\begin{aligned} \bar{v}_\sigma(p_2)\,\not{k}u_\sigma(p_1) &= k\cdot v_\sigma \\ \bar{v}_\sigma(p_2)\,\not{k}_1\,\not{k}_2\,\not{k}_3 u_\sigma(p_1) &= (k_1\cdot k_2)(k_3\cdot v_\sigma) + (k_2\cdot k_3)(k_1\cdot v_\sigma) \\ &\quad - (k_1\cdot k_3)(k_2\cdot v_\sigma) + i\sigma\epsilon_{\mu\nu\tau\alpha}k_1^\mu k_2^\nu k_3^\tau v_\sigma^\alpha. \end{aligned} \tag{3.9}$$

This is a special case of a more general mechanism discussed in Appendix A.

With the aid of these identities, the expressions for the matrix elements take the form:

$$
\begin{aligned}
i\mathcal{M}_\sigma^{\lambda^-\lambda^+}(\nu) &= \frac{-ie^2}{2t\sin^2\theta_W}\delta_{\sigma L}\big[-p_2\cdot\varepsilon^*(p_4,\lambda^+)\,\varepsilon^*(p_3,\lambda^-)\cdot v_L \\
&\quad + p_1\cdot\varepsilon^*(p_3,\lambda^-)\,\varepsilon^*(p_4,\lambda^+)\cdot v_L + (\varepsilon^*(p_4,\lambda^+)\cdot\varepsilon^*(p_3,\lambda^-))(p_3\cdot v_L) \\
&\quad - i\epsilon_{\mu\nu\tau\alpha}\,\varepsilon^{\mu *}(p_4,\lambda^+)(p_1-p_3)^\nu\,\varepsilon^{\tau *}(p_3,\lambda^-)v_L^\alpha\big] \\
i\mathcal{M}_\sigma^{\lambda^-\lambda^+}(\gamma) &= \frac{ie^2}{s}\,\varepsilon^{\mu *}(p_3,\lambda^-)\,\varepsilon^{\nu *}(p_4,\lambda^+)v_\sigma^\tau\frac{\Gamma^\gamma_{\mu\nu\tau}}{e} \\
i\mathcal{M}_\sigma^{\lambda^-\lambda^+}(Z) &= \frac{ie^2 g_\sigma}{s-m_Z^2}\,\varepsilon^{\mu *}(p_3,\lambda^-)\,\varepsilon^{\nu *}(p_4,\lambda^+)v_\sigma^\tau\frac{\Gamma^Z_{\mu\nu\tau}}{e\cot\theta_W},
\end{aligned}
\tag{3.10}
$$

where we have used $\varepsilon^*(p_4,\lambda^+)\cdot(p_1-p_3) = \varepsilon^*(p_4,\lambda^+)\cdot(p_4-p_2) = -\varepsilon^*(p_4,\lambda^+)\cdot p_2$.

Substituting eqns. (3.2) and (3.1) we get

$$
\begin{aligned}
i\mathcal{M}_\sigma^{\lambda^-\lambda^+}(\gamma) &= \frac{ie^2}{s}\Bigg[2\left(1+\frac{2\lambda}{r}\right)(p_3\cdot v_\sigma)\,\varepsilon^*(p_3,\lambda^-)\cdot\varepsilon^*(p_4,\lambda^+) \\
&\quad - \frac{8\lambda}{rs}(p_3\cdot v_\sigma)p_3\cdot\varepsilon^*(p_4,\lambda^+)p_4\cdot\varepsilon^*(p_3,\lambda^-) \\
&\quad + (1+\kappa+\lambda)\big[(p_4\cdot\varepsilon^*(p_3,\lambda^-))(\varepsilon^*(p_4,\lambda^+)\cdot v_\sigma) \\
&\quad - (p_3\cdot\varepsilon^*(p_4,\lambda^+))(\varepsilon^*(p_3,\lambda^-)\cdot v_\sigma)\big]\Bigg] \\
i\mathcal{M}_\sigma^{\lambda^-\lambda^+}(Z) &= \frac{ie^2\cot\theta_W g_\sigma}{s-m_Z^2}\Bigg[2\left(1+\frac{2\lambda}{r}\right)(p_3\cdot v_\sigma)(\varepsilon^*(p_3,\lambda^-)\cdot\varepsilon^*(p_4,\lambda^+)) \\
&\quad - \frac{8\lambda}{rs}(p_3\cdot v_\sigma)(p_3\cdot\varepsilon^*(p_4,\lambda^+))(p_4\cdot\varepsilon^*(p_3,\lambda^-)) \\
&\quad + (2+\lambda)\big[(p_4\cdot\varepsilon^*(p_3,\lambda^-))(\varepsilon^*(p_4,\lambda^+)\cdot v_\sigma) \\
&\quad - (p_3\cdot\varepsilon^*(p_4,\lambda^+))(\varepsilon^*(p_3,\lambda^-)\cdot v_\sigma)\big]\Bigg].
\end{aligned}
\tag{3.11}
$$

The component along the $\hat{z}$ axis of the total angular momentum of the incoming particles is σ. The component along the W^- direction of motion of the total angular momentum of the final state is $\Delta\lambda = \lambda^- - \lambda^+$. It is natural to factor out of the matrix elements the functions corresponding to this rotation.[36] The appropriate factor is $d^{J_0}_{\sigma,\Delta\lambda}(\theta)$, where $J_0 = \max(1, |\Delta\lambda|)$ is the *minimum* angular momentum transferred. The d functions used here are given in table 4. For future use we give some expressions not used for $e^+e^- \to W^+W^-$.

In the s-channel diagrams, only $J = 1$ is possible, and therefore $\mathcal{M}^{-+}(\gamma, Z) = \mathcal{M}^{+-}(\gamma, Z) = 0$. Substituting the explicit four vectors from eqns. (3.6) and (3.7), and extracting some overall factors

$$\mathcal{M}^{\lambda^-\lambda^+}_\sigma = \sqrt{2}e^2 \tilde{\mathcal{M}}^{\lambda^-\lambda^+}_\sigma d^{J_0}_{\sigma,\Delta\lambda}(\theta) \tag{3.12}$$

the matrix elements take the form

$$\begin{aligned}
\tilde{\mathcal{M}}^{\lambda^-\lambda^+}_\sigma(\nu) &= \frac{1}{\sin^2\theta_W(2 - r - 2\beta\cos\theta)}\delta_{\sigma L}A^{\lambda^-\lambda^+} \\
\tilde{\mathcal{M}}^{\lambda^-\lambda^+}_\sigma(\gamma) &= -\beta B^{\lambda^-\lambda^+}_\gamma \\
\tilde{\mathcal{M}}^{\lambda^-\lambda^+}_\sigma(Z) &= \beta g_\sigma \cot\theta_W \frac{s}{s - m_Z^2} B^{\lambda^-\lambda^+}_Z .
\end{aligned} \tag{3.13}$$

The coefficients A and B are shown in table 5.

While the individual matrix elements have a bad high-energy behavior, some diverging as $O(1/r)$, their sum is $O(1)$ in the Standard Model. This behavior requires some delicate cancellations. These cancellations are evident from the table. In the Standard Model (and more generally whenever the photon and Z couplings to the W are identical), $B^{\lambda^-\lambda^+}_\gamma = B^{\lambda^-\lambda^+}_Z$. For right-handed electrons, $g_R \cot\theta_W = 1$ (eqn. (3.5)), and the photon contribution directly cancels the Z contribution in the limit $s/(s - m_Z^2) \to 1$. For left handed electrons, the photon contribution again

Table 3. The functions $d^{J_0}_{\Delta\lambda_1,\Delta\lambda_2}(\theta)$

$d^2_{\pm1,\pm2} = d^2_{\mp2,\mp1}$	$\pm\frac{1}{2}(1+\cos\theta)\sin\theta$
$d^2_{\pm1,\mp2} = d^2_{\mp2,\pm1}$	$\pm\frac{1}{2}(1-\cos\theta)\sin\theta$
$d^2_{\pm2,0} = d^2_{0,\pm2}$	$\frac{\sqrt{3}}{2\sqrt{2}}\sin^2\theta$
$d^1_{\pm1,\pm1}$	$\frac{1}{2}(1+\cos\theta)$
$d^1_{\pm1,\mp1}$	$\frac{1}{2}(1-\cos\theta)$
$d^1_{0,\pm1} = d^1_{\mp1,0}$	$\pm\sqrt{\frac{1}{2}}\sin\theta$
$d^{3/2}_{3/2,3/2}$	$\frac{1}{2\sqrt{2}}(1+\cos\theta)^{3/2}$
$d^{3/2}_{\mp1/2,3/2} = d^{3/2}_{3/2,\pm1/2}$	$\frac{\sqrt{3}}{2\sqrt{2}}\sin\theta\sqrt{1\mp\cos\theta}$
$d^{1/2}_{-1/2,\pm1/2}$	$\frac{1}{\sqrt{2}}\sqrt{1\mp\cos\theta}$

cancels the first part of g_L. The bad high-energy behavior multiplying the second part of g_L is canceled by the neutrino diagram contribution:

$$\frac{A^{\lambda^-\lambda^+}}{\sin^2\theta_W(2-r-2\beta\cos\theta)} \longrightarrow \frac{1}{2\sin^2\theta_W}\cdot\frac{A^{\lambda^-\lambda^+}}{1-\cos\theta} \longrightarrow \frac{B_Z^{\lambda^-\lambda^+}}{2\sin^2\theta_W} \qquad (r\to 0) \tag{3.14}$$

Table 5. The coefficients A^{λ_1,λ_2} and $B_V^{\lambda_1,\lambda_2}$ of eqn. (3.13).

$(\lambda^-\lambda^+)$	$A^{\lambda^-\lambda^+}$	$B_\gamma^{\lambda^-\lambda^+}$	$B_Z^{\lambda^-\lambda^+}$
$(+-),(-+)$	$\sqrt{2}$	0	0
$(0+),(-0)$	$(2\beta - 2\cos\theta + r)/\sqrt{r}$	$(1+\kappa+\lambda)/\sqrt{r}$	$(2+\lambda)/\sqrt{r}$
$(+0),(0-)$	$(2\beta - 2\cos\theta - r)/\sqrt{r}$	$(1+\kappa+\lambda)/\sqrt{r}$	$(2+\lambda)/\sqrt{r}$
$(++),(--)$	$\beta - \cos\theta$	$1 + 2\lambda/r$	$1 + 2\lambda/r$
(00)	$(2\beta - 2\cos\theta + \beta r)/r$	$2\kappa/r + 1$	$2/r + 1$

Using couplings outside the Standard Model, this good high-energy behavior is not maintained for arbitrary values of κ and λ. In the high-energy limit, the leading terms (at the matrix element level) arise from two sources: the κ term of $\tilde{\mathcal{M}}^{00}(\gamma)$ and the λ term of $\tilde{\mathcal{M}}_L^{++,--}(Z)$ which is not canceled by the photon diagram contribution. The leading terms at the matrix element level are $O(\Delta\kappa/r)$ and $O(\lambda/r)$, where $\Delta\kappa = \kappa - 1$. Squared, these terms are $O(\Delta\kappa^2/r^2)$ and $O(\lambda^2/r^2)$. The next-to-leading terms, $O(\Delta\kappa/r)$ and $O(\lambda/r)$, are cross-terms between the leading and $O(1)$ terms in the matrix element. The relevant matrix elements are:

$$\begin{aligned}
\mathcal{M}_R^{00} &= e^2 \sin\theta \left(\frac{2\Delta\kappa}{r} - \frac{1}{2\cos^2\theta_W} \right) + O(r) \\
\mathcal{M}_L^{00} &= -e^2 \sin\theta \left(\frac{2\Delta\kappa}{r} - \frac{1}{4\cos^2\theta_W \sin^2\theta_W} \right) + O(r) \\
\mathcal{M}_L^{++,--} &= \frac{-e^2 \sin\theta}{\sin^2\theta_W} \frac{\lambda}{r} + O(r).
\end{aligned} \tag{3.15}$$

Squaring and summing over polarizations, the leading behavior is

$$\begin{aligned}
\sum_{\lambda^-,\lambda^+,\sigma} \left| \mathcal{M}_\sigma^{\lambda^-\lambda^+} \right|^2 =& e^4 \sin^2\theta \left[\frac{1}{r^2} \left(8\Delta\kappa^2 + \frac{2\lambda^2}{\sin^2\theta_W} \right) - \frac{\Delta\kappa}{r} \frac{1 + 2\sin^2\theta_W}{\cos^2\theta_W \sin^2\theta_W} \right] \\
&+ O\left(\frac{\Delta\kappa^2}{r} \right) + O\left(\frac{\lambda^2}{r} \right) + O(1)
\end{aligned} \tag{3.16}$$

An important point to notice is that the angular dependence factors out of the leading terms in the expression. If we draw the curve on the κ-λ plane on which the the differential cross section is equal to its Standard Model value, its shape (to leading order in $1/r$) does not depend on θ. This shape is shown schematically in fig. 4.

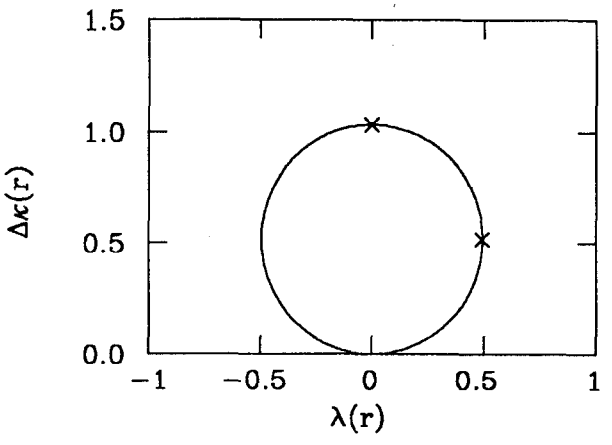

Figure 4. Schematic shape of the curve corresponding to a Standard Model value of the differential cross section The top and right ×'s correspond to the points $(0, x_0/\sin\theta_W)$ and $(x_0, x_0/2\sin\theta_W)$ respectively, where $x_0 = \left[(1+2\sin^2\theta_W)/(8\cos^2\theta_W\sin\theta_W)\right] r$. Note that the entire shape scales like r.

The differential cross section for producing a W pair of specific polarization is:

$$\sigma^{\lambda^-\lambda^+} = \frac{1}{4}\int d\Omega \frac{(2\pi)^4}{2s}|\mathcal{M}_\sigma^{\lambda^-\lambda^+}|^2 \frac{\sqrt{1-4m_W^2/s}}{8(2\pi)^6} = \frac{\beta}{128\pi s}\int_{-1}^{1} d(\cos\theta)|\mathcal{M}_\sigma^{\lambda^-\lambda^+}|^2$$

$$= \frac{3R}{32}\beta\int_{-1}^{1} d(\cos\theta)\left|\frac{\mathcal{M}_\sigma^{\lambda^-\lambda^+}}{e^2}\right|^2, \tag{3.17}$$

where

$$R = \frac{4\pi\alpha^2}{3s} = 347\text{fb}\left(\frac{E_{CM}}{500\text{GeV}}\right)^{-2}. \tag{3.18}$$

Figure 5 shows the differential cross section for producing W's of various helicitiy combinations. Figure 6 shows the dependence on κ and λ of the total cross section for producing W's of various helicitiy combinations. These figures are the idealized cross sections, assuming monochromatic beams of perfectly polarized electrons. Note the strong dependence of the (00) combination on κ, and of the $(++)+(--)$ combination on λ.

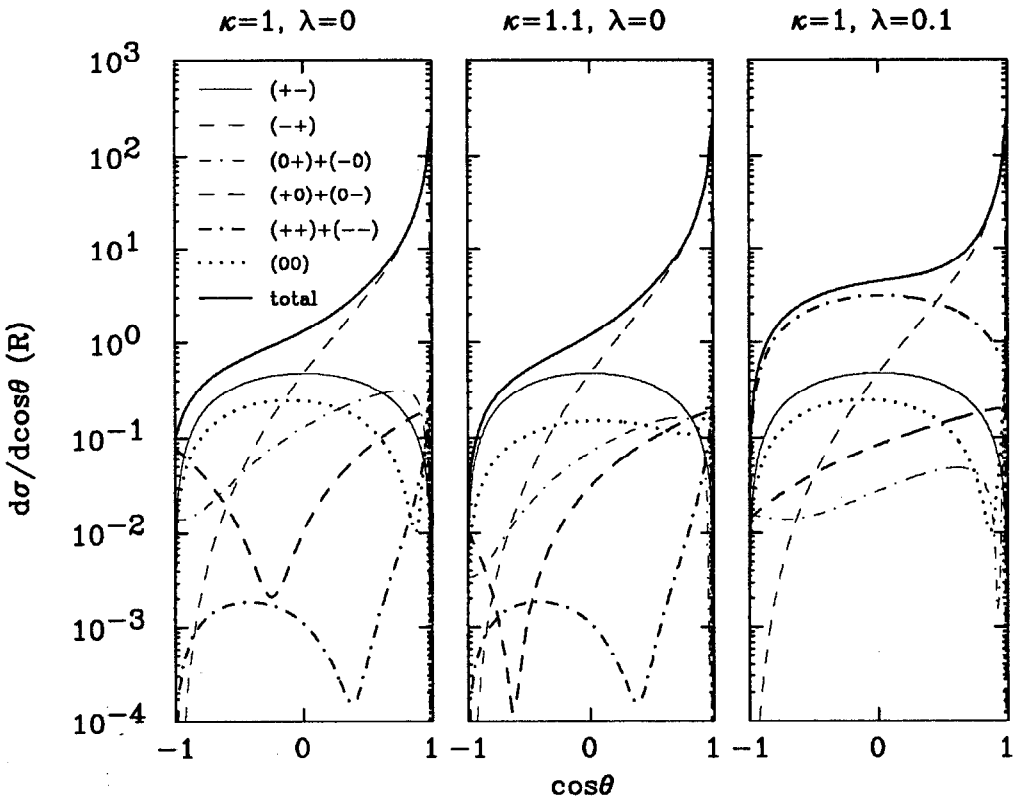

Figure 5. Differential cross sections for producing W pairs of specific helicity combination with center-of-mass energy of 500 GeV as a function of $\cos\theta$. Here and henceforth, cross sections are given in units of R.

The polarization of the individual W's cannot be measured directly. The direction of the decay products of the W, however, carries with it important information from which the polarized production cross sections can be extracted.

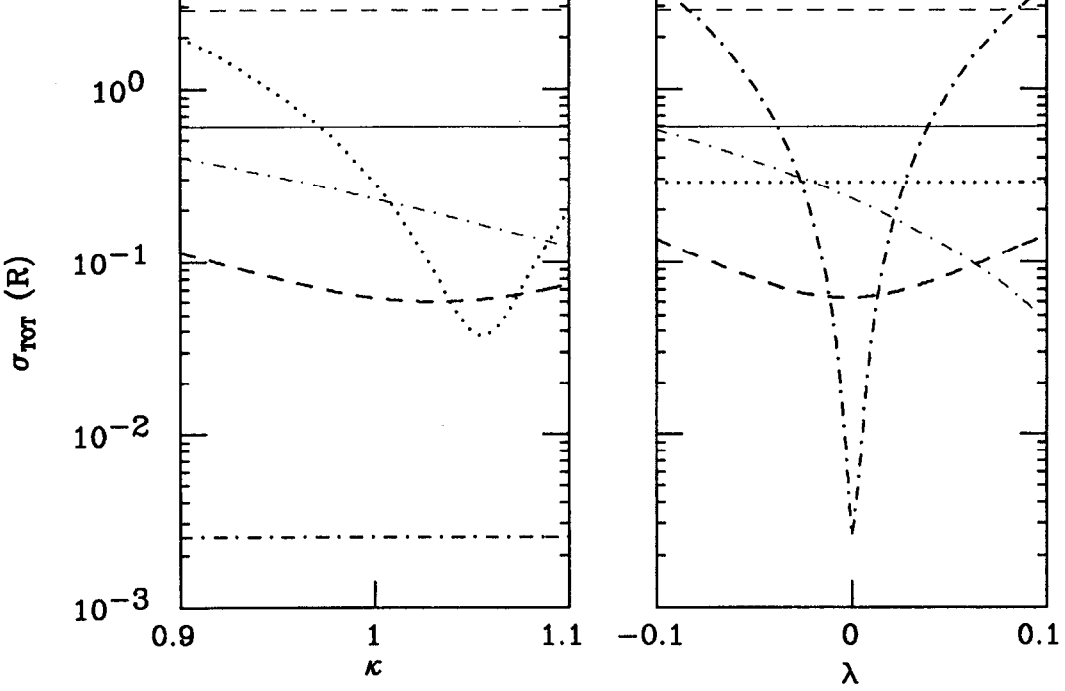

Figure 6. Total cross sections with center-of-mass energy of 500 GeV ($|\cos\theta < 0.8|$). The left frame shows the dependence on κ. The right frame shows the dependence on λ. The meaning of the lines is the same as in fig. 5.

A priori one has to consider interference terms between the production amplitudes of W's with different helicities. In practice, these interference terms vanish upon integration over the azimuthal angle of the W decay.

Let us concentrate on the decay $W^- \to l^-\overline{\nu}$. Let χ be the angle between the charged lepton momentum and the W direction of motion, as measured in the W rest frame. The χ distribution is then given by

$$\frac{d\sigma}{d\cos\chi} = \sum_{\lambda} \sigma_\lambda P_\lambda(\chi), \tag{3.19}$$

where

$$\sigma_\lambda = \sum_{\lambda'} \sigma(e^+e^- \to W_{\lambda'}W_\lambda) \tag{3.20}$$

and

$$\begin{aligned} P_{\pm 1}(\chi) &= \frac{3(1 \mp \cos\chi)^2}{4} \\ P_0(\chi) &= \frac{3(1 - \cos^2\chi)}{4}. \end{aligned} \tag{3.21}$$

Using these formulas, one can use the χ distribution to calculate the production rates of the various polarizations.

3.3 Observables

In this section we discuss the various observables and assess their sensitivity to κ and λ. All the calculations in this section are performed for a 500 GeV e^+e^- collider, assuming perfectly monochromatic electron beams. Two types of errors are associated with each experimental measurement: statistical and systematic. As we show below, the total cross section for $e^+e^- \to W^+W^-$ in the Standard Model ($|\cos\theta| < 0.8$) is about 4 R. With an integrated luminosity of 9fb^{-1}, the total number of events is approximately 1.25×10^4. Statistical errors on the full event sample are less than 1%. Systematic errors are more difficult to estimate. A detailed study can only be done using Monte Carlo techniques. Factors entering into the systematic errors include particle misidentification, uncertainty in the size of backgrounds, calorimeter accuracy, etc. In estimating systematic errors we rely on related Monte Carlo studies,[37] as well as on the accuracy reported from the recent SLC and LEP[38] experiments. As most systematic errors are 0.03-0.05, we simplify our analysis by ignoring the smaller statistical errors. This step is not allowed if the integrated luminosity is significantly smaller than the one we assume here.

The most straightforward observable is the total cross section σ_{TOT}. To reduce uncertainties associated with particles escaping detection by going near the beam

pipe, we cut the angular integration at $|\cos\theta| = 0.8$. We assume a systematic error of 5% in total cross section measurements. Figure 7 shows the total cross section for $e^+e^- \to W^+W^-$ as a function of κ for several values of λ, while fig. 8 shows its dependence on λ for several values of κ.

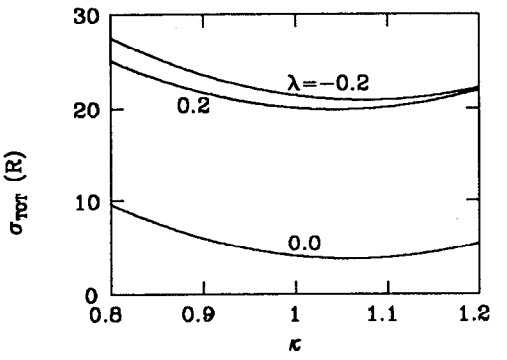

Figure 7. $\sigma_{\rm TOT}$ for $e^+e^- \to W^+W^-$ as a function of κ for $\lambda = -0.2, 0, 0.2$.

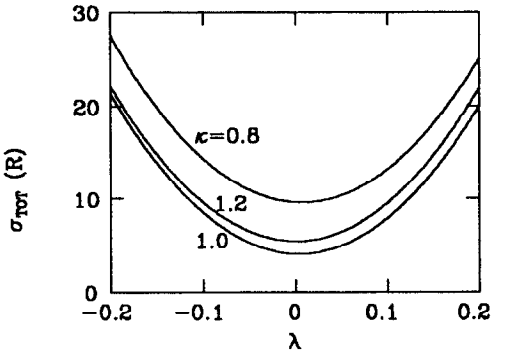

Figure 8. $\sigma_{\rm TOT}$ for $e^+e^- \to W^+W^-$ as a function of λ for $\kappa = 0.8, 1, 1.2$.

Systematic errors associated with total cross section measurement may be reduced by looking at ratios of cross sections. The first ratio we look at is the forward-backward asymmetry FB defined as

$$\mathrm{FB} = \frac{\sigma(\cos\theta > 0) - \sigma(\cos\theta < 0)}{\sigma(\cos\theta > 0) + \sigma(\cos\theta < 0)}. \tag{3.22}$$

Measuring the forward-backward asymmetry FB relies on charge identification of the W's. Charge identification in events in which both W's decay hadronically is challenging, though by no means impossible. Semi-leptonic events (*i.e.* events in which one W decays leptonically while the other decays hadronically), however, provide for precise charge identification. These constitute about 44% of the total event sample. With these events, we assume that FB can be measured with a

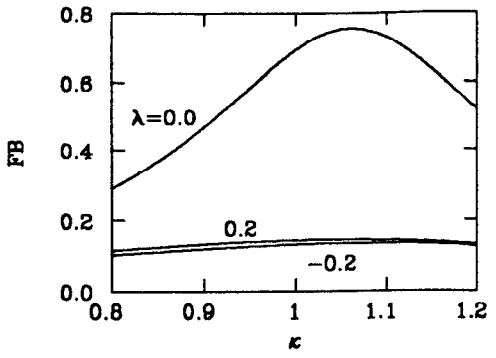

Figure 9. FB as a function of κ for $\lambda = -0.2, 0, 0.2$.

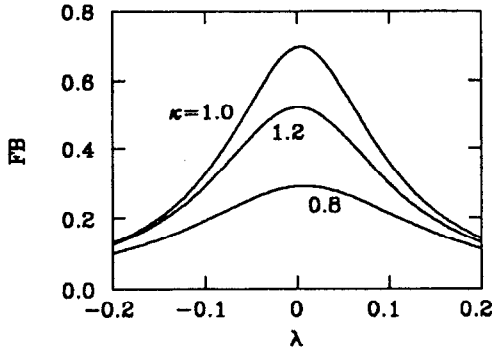

Figure 10. FB as a function of λ for $\kappa = 0.8, 1, 1.2$.

systematic error of 0.03. Figures 9 and 10 show the dependence of the forward-backward asymmetry on κ and λ.

Additional information can be extracted from the W angular distribution by looking at the ratio

$$\mathrm{IO} = \frac{\sigma(|\cos\theta| < 0.4)}{\sigma(|\cos\theta| < 0.8)}. \tag{3.23}$$

Charge identification is not necessary for the determination of IO, and thus one can safely use the entire event sample. Here we assume that IO can be measured with a systematic error of 0.03. Figures 11 and 12 shows IO's on κ and λ.

The angle χ between one of the W decay products' momentum and the W direction of motion, as measured in the W rest frame can be measured for the leptonically decaying W in a semi-leptonic event. Measuring the total momentum of the hadronic jets and the momentum of the charged lepton, one is left with the three unknown parameters of the missing neutrino. Imposing the constraints that the total momentum equals that of the colliding electrons, and that the invariant mass of the neutrino-lepton system equals that of the W, one can over-determine the neutrino momentum. Even allowing arbitrary energy loss to beamstrahlung

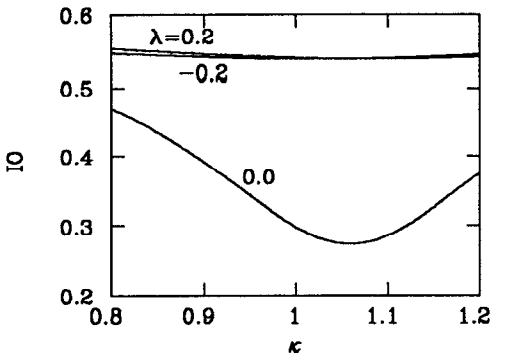

Figure 11. IO as a function of κ for $\lambda = -0.2, 0, 0.2$.

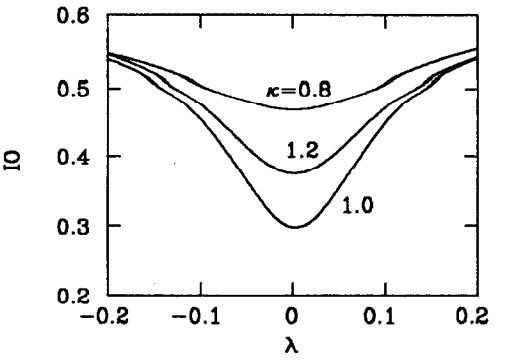

Figure 12. IO as a function of λ for $\kappa = 0.8, 1, 1.2$.

(which we do not consider in this chapter), one can calculate the neutrino momentum up to a twofold ambiguity. Monte Carlo studies suggest that consistantly selecting the more probable solution does not significantly degrade the sensitivity of the measured quantities to the anomalous couplings.[37] By measuring the χ distribution one can easily derive the ratio L/T defined as

$$L/T = \frac{\sum_\lambda \sigma(e^+e^- \to W_\lambda W_L)}{\sum_\lambda \sigma(e^+e^- \to W_\lambda W_T)}, \tag{3.24}$$

where L and T refer to longitudinally and transversly polarized W's respectively. Here we assume that the L/T ratio can be measured with a systematic error of 0.03. Figures 13 and 14 show the L/T ratio's dependence on κ and λ.

3.4 Discovery limits

In assessing the discovery potential of an experiment, we always assume that Standard Model results are actually measured. We then ask what region in the κ-λ plane is still allowed based on the measured results.

The individual measurements are assumed to have a normal distribution with standard deviation σ equal to the systematic error. Let $f_i(\kappa, \lambda)$ be the theoretical

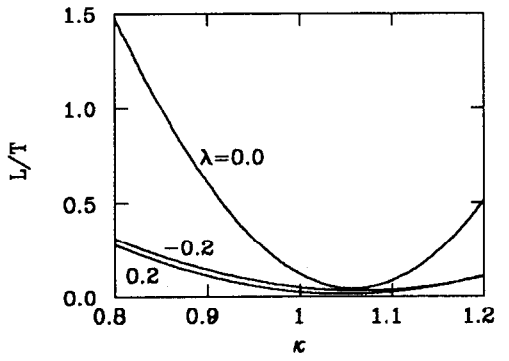

Figure 13. L/T as a function of κ for $\lambda = -0.2, 0, 0.2$.

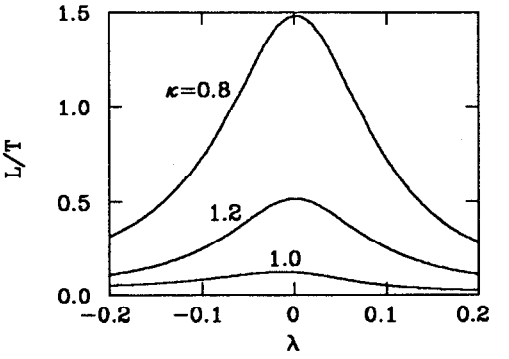

Figure 14. L/T as a function of λ for $\kappa = 0.8, 1, 1.2$.

dependence of the observable i on κ and λ, with error σ_i. The probability that we actually measure the value $\hat{f}_i$ is given by

$$P(\hat{f}_i) = \exp\left(-\frac{(f_i(\kappa,\lambda) - \hat{f}_i)^2}{2\sigma_i^2}\right) \Big/ \sigma_i\sqrt{2\pi}. \tag{3.25}$$

While strictly speaking it only makes sense to talk about the probability of measuring $\hat{f}_i$ *given* a certain κ-λ combination, we interpret that same value as the probability for a given κ-λ combination given that $\hat{f}_i$ was actually measured. As we assume Standard Model values are measured, each observable i defines a probability function on the κ-λ plane given by

$$P_i(\kappa,\lambda) = \exp\left(-\frac{(f_i(\kappa,\lambda) - f_i(1,0))^2}{2\sigma_i^2}\right) \Big/ \sigma_i\sqrt{2\pi}. \tag{3.26}$$

Note that this probability function is not normalized, *i.e.* $\int P_i(\kappa,\lambda)d\kappa d\lambda \neq 1$.

One can get a good idea of the kind of bounds derivable from the observable i by plotting the region of all (κ,λ) such that $|f_i(\kappa,\lambda) - f_i(1,0)| < n\sigma_i$ for some n. In this work we always display the 2σ regions corresponding to $n = 2$.

To combine the results of several observables we assume that their measurement is independent. The probability for a given point in the κ-λ plane is given by taking the products over all probability functions $P_i(\kappa, \lambda)$:

$$\begin{aligned} P(\kappa,\lambda) &= \prod_{i=1}^{k} P_i(\kappa,\lambda) \\ &= \frac{1}{(2\pi)^{k/2}\prod_i \sigma_i} \exp\left(-\frac{1}{2}\sum_i \left(\frac{f_i(\kappa,\lambda) - f_i(1,0)}{\sigma_i}\right)^2\right) \\ &= \frac{1}{(2\pi)^{k/2}\prod_i \sigma_i} \exp\left(-\frac{1}{2}\sum_i \tilde{f}_i(\kappa,\lambda)\right), \end{aligned} \tag{3.27}$$

where $\tilde{f}_i(\kappa,\lambda) = (f_i(\kappa,\lambda) - f_i(1,0))/\sigma_i$ is the normalized observable.

The probability function $P(\kappa,\lambda)$ has to be normalized:

$$\hat{P}(\kappa,\lambda) = \frac{P(\kappa,\lambda)}{\int d\kappa' d\lambda' P(\kappa',\lambda')}. \tag{3.28}$$

The new function $\hat{P}(\kappa,\lambda)$ is evidently maximized at $\kappa = 1$, $\lambda = 0$. Unless all the observables have the same κ and λ dependence (*i.e.* $f_i(\kappa,\lambda) = f_i(c(\kappa,\lambda))$ with the same c for all i), the function $\hat{P}(\kappa,\lambda)$ drops to zero as either κ or λ approaches infinity. Based on that, let us define for every α $(0 < \alpha < 1)$ a cutoff value $P_0(\alpha)$ such that

$$\int\limits_{\hat{P}(\kappa,\lambda) > P_0(\alpha)} d\kappa d\lambda \hat{P}(\kappa,\lambda) = \alpha. \tag{3.29}$$

The region to which a set of measurements can restrict κ and λ with a specific confidence level α is then the region of all points (κ,λ) such that $\hat{P}(\kappa,\lambda) > P_0(\alpha)$. Typical confidence levels are 68% and 90%.

Figure 15 shows the 2σ regions for each observable discussed in the previous section. The central regions are the 68% and 90% confidence level bounds obtained by combining all the measurements. Note that the allowed region in each case is disconnected. One has to rely on other experiments to distinguish the $\Delta\kappa = 0$ and the $\Delta\kappa \approx 0.115$ regions.

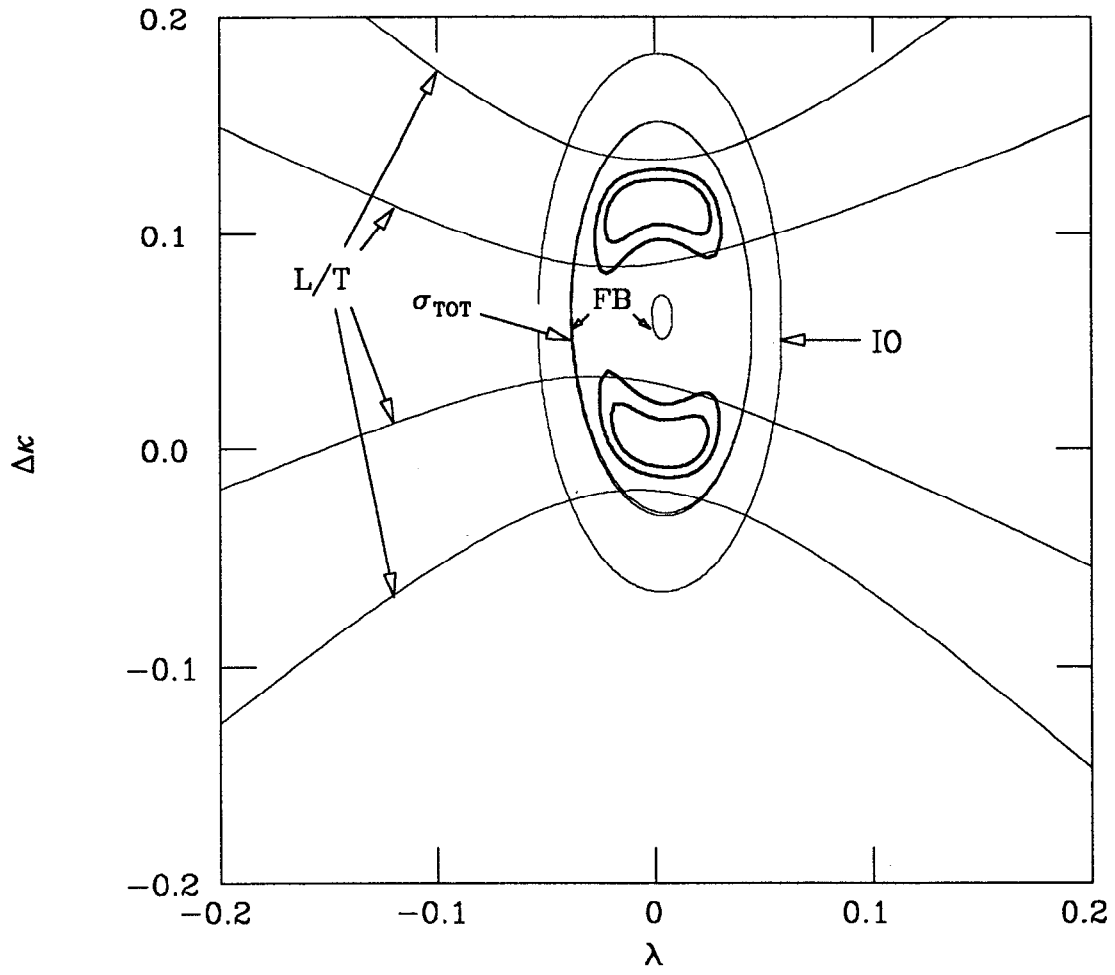

Figure 15. The (2σ) regions in the κ-λ plane from various measurements of $e^+e^- \rightarrow W^+W^-$. The regions in the center correspond to 68% and 90% confidence level bounds from the combination of all measurements.

4. $e\gamma \rightarrow W\nu$

4.1 Introduction

The second process we study is $e\gamma \rightarrow W\nu$. This process does not exhibit the same delicate cancellations as $e^+e^- \rightarrow W^+W^-$, and is, therefore, generally less sensitive to non-Standard Model couplings. Since one of the diagrams involves the t-channel exchange of a heavy vector boson, the total cross section for this process remains constant rather than drop like $1/s$. At high energies ($s \gg m_W^2$), the process has a relatively large total cross section, allowing reasonable statistics with smaller effective $e\gamma$ luminosity. Only $W\gamma$ couplings contribute, and so we avoid the complications associated with the Z couplings.

This chapter proceeds as follows. In the next section, we calculate the helicity amplitudes and the 'idealized' production cross section, assuming a perfectly monochromatic $e\gamma$ collider. This calculation follows the same general lines as the one carried out in section 3.2. In sect. 3 we consider the three potential photon sources. We introduce the effective luminosity and show how it is used in calculating cross sections. Section 4 evaluates potential observables, presenting their dependence on κ and λ. Section 5 assesses possible bounds on κ and λ from the individual measurements, and combines them to given specific confidence limits in the κ-λ plane.

4.2 Cross-section calculation

Two Feynman diagrams contribute to the process $e\gamma \rightarrow W\nu$ (fig. 16). Note that only left-handed electrons take part in the interaction.

With one W and the photon being on-shell, and momenta labeled as in fig. 17,

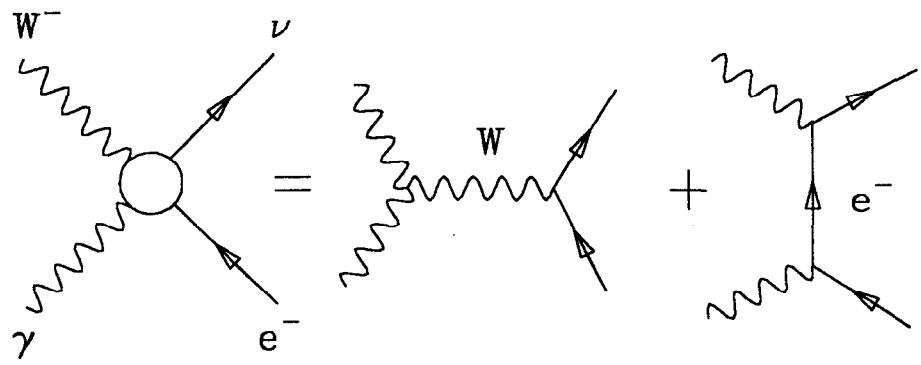

Figure 16. Feynman diagrams for $e\gamma \to W\nu$.

the $WW\gamma$ vertex (2.2) takes the form

$$\begin{aligned}\Gamma^{\mu\nu\alpha} &= ie\Big[2g^{\alpha\nu}p_4^{\mu} + 2g^{\alpha\mu}p_2^{\nu} - g^{\mu\nu}\,(p_4+p_2)^{\alpha} + (\kappa{+}\lambda{-}1)\,(g^{\mu\alpha}p_2^{\nu} - g^{\mu\nu}p_2^{\alpha}) \\ &\qquad - \frac{\lambda}{m_W^2}(p_2+p_4)^{\alpha}\,(p_4^{\mu}p_2^{\nu} - (p_4\cdot p_2)\,g^{\mu\nu})\Big]. \\ &= ie\Big[2g^{\alpha\nu}p_4^{\mu} + 2g^{\alpha\mu}p_2^{\nu} - g^{\mu\nu}\,(p_4+p_2)^{\alpha} + (\kappa{+}\lambda{-}1)\,(g^{\mu\alpha}p_2^{\nu} - g^{\mu\nu}p_2^{\alpha}) \\ &\qquad - \frac{\lambda}{rs}(p_2+p_4)^{\alpha}\,(p_4^{\mu}p_2^{\nu} - (p_4\cdot p_2)\,g^{\mu\nu})\Big],\end{aligned} \tag{4.1}$$

where $r = m_W^2/s$.

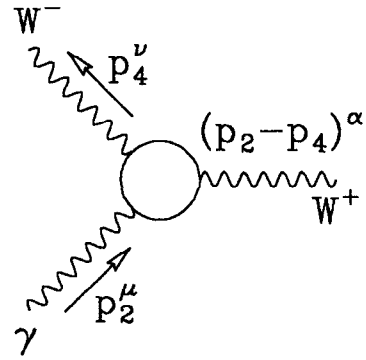

Figure 17. The $WW\gamma$ vertex for $e\gamma \to W\nu$.

Only left-handed electrons take part in this process. The matrix element is given by

$$\mathcal{M}^{\lambda\lambda'} = \mathcal{M}^{\lambda\lambda'}(\nu) + \mathcal{M}^{\lambda\lambda'}(W) \tag{4.2}$$

where λ and λ' are the helicities of the photon and W^- respectively,

$$\begin{aligned}
i\mathcal{M}^{\lambda\lambda'}(\nu) &= \varepsilon^{\mu}(p_2,\lambda)\varepsilon^{\nu *}(p_4,\lambda')\overline{u}_L(p_3)\left(\frac{ig}{\sqrt{2}}P_L\gamma_\nu\right)\frac{i(\not{p}_1+\not{p}_2)}{s}(-ie\gamma_\mu)u_L(p_1) \\
&= \frac{ie^2}{\sqrt{2}s\sin\theta_W}\overline{u}_L(p_3)\ \not{\varepsilon}^*(p_4,\lambda')(\not{p}_1+\not{p}_2)\ \not{\varepsilon}(p_2,\lambda)u_L(p_1) \\
i\mathcal{M}^{\lambda\lambda'}(W) &= \varepsilon^{\mu}(p_2,\lambda)\varepsilon^{\nu *}(p_4,\lambda')\overline{u}_L(p_3)\left(\frac{ig}{\sqrt{2}}P_L\gamma_\rho\right)u_L(p_1)\frac{-ig^{\rho\alpha}}{t-m_W^2}(i\Gamma_{\alpha\mu\nu}) \\
&= \frac{ie^2}{\sqrt{2}(t-m_W^2)\sin\theta_W}\varepsilon^{\mu}(p_2,\lambda)\varepsilon^{\nu *}(p_4,\lambda')\overline{u}_L(p_3)\gamma^\alpha u_L(p_1)\left(\frac{\Gamma_{\alpha\mu\nu}}{e}\right),
\end{aligned} \tag{4.3}$$

and $\varepsilon(p_2,\lambda)$ and $\varepsilon^*(p_4,\lambda')$ are the polarization vectors of the photon and the W^- respectively.

In the $e\gamma$ center-of-mass frame, the momenta in the process take the following values:

$$\begin{aligned}
p_1 &= \frac{\sqrt{s}}{2}(0,0,1,1) \qquad & p_3 &= \frac{\sqrt{s}(1-r)}{2}(\sin\theta,0,\cos\theta,1) \\
p_2 &= \frac{\sqrt{s}}{2}(0,0,-1,1) \qquad & p_4 &= \frac{\sqrt{s}}{2}(-(1-r)\sin\theta,0,-(1-r)\cos\theta,1+r)
\end{aligned} \tag{4.4}$$

The two polarization vectors are:

$$\begin{aligned}
\varepsilon^*(p_4,\pm) &= \frac{1}{\sqrt{2}}(\cos\theta,\pm i,-\sin\theta,0) \qquad & \varepsilon(p_2,\pm) &= \frac{1}{\sqrt{2}}(1,\mp i,0,0) \\
\varepsilon^*(p_4,0) &= \frac{1}{2\sqrt{r}}((1+r)\sin\theta,0,(1+r)\cos\theta,1-r)
\end{aligned} \tag{4.5}$$

As in eqn. (3.8), we define the four vector

$$v_L = \mathcal{V}_L(p_3, p_1)$$
$$= \sqrt{s(1-r)}(\sqrt{1-\cos\theta}, i\sqrt{1-\cos\theta}, \sqrt{1+\cos\theta}, \sqrt{1+\cos\theta}) \tag{4.6}$$

(see Appendix A), which obeys

$$\begin{aligned} \overline{u}_L(p_3)\, \not{p} u_L(p_1) &= p \cdot v \\ \overline{u}_L(p_3)\, \not{k}_1\, \not{k}_2\, \not{k}_3 u_L(p_1) &= (k_1 \cdot k_2)(k_3 \cdot v_\sigma) + (k_2 \cdot k_3)(k_1 \cdot v_\sigma) \\ &\quad - (k_1 \cdot k_3)(k_2 \cdot v_\sigma) + i\sigma\epsilon_{\mu\nu\tau\alpha} k_1^\mu k_2^\nu k_3^\tau v_\sigma^\alpha. \end{aligned} \tag{4.7}$$

Next, we repeat the same steps as in section 3.2, substituting the vertex expression from eqn. (4.1) and the explicit four vectors from eqns. (4.4) and (4.5). Again we factor the d function $d^{J_0}_{\Delta\lambda,\Delta\lambda'}(\theta)$ where $\Delta\lambda = \lambda + 1/2$, $\Delta\lambda' = \lambda' + 1/2$ and $J_0 = \max(|\Delta\lambda|, |\Delta\lambda'|)$. The d functions are given in table 4. We then get the following expressions for the matrix elements:

$$\mathcal{M}^{\lambda\lambda'} = \frac{\beta e^2}{\sin\theta_W} d^{J_0}_{\Delta\lambda,\Delta\lambda'}(\theta) \left(\tilde{\mathcal{M}}^{\lambda\lambda'}(\nu) + \tilde{\mathcal{M}}^{\lambda\lambda'}(W) \right), \tag{4.8}$$

where $\beta = \sqrt{1-r}$ and

$$\begin{aligned} \tilde{\mathcal{M}}^{\lambda\lambda'}(\nu) &= A^{\lambda\lambda'} \\ \tilde{\mathcal{M}}^{\lambda\lambda'}(W) &= \frac{B^{\lambda\lambda'}}{1 - \cos\theta + r(1+\cos\theta)}. \end{aligned} \tag{4.9}$$

The coefficients A and B are given in table 6.

The cross section for producing a W with helicity λ' from a photon with helicity

Table 6. The coefficients A_{λ_1,λ_2} and B_{λ_1,λ_2} of eqn. (4.9). $r = m_W^2/s$ and $\beta = \sqrt{1-r}$.

$(\lambda\lambda')$	$A^{\lambda\lambda'}$	$B^{\lambda\lambda'}$
$(--)$	$\sqrt{2}$	$-\big(2(3-\cos\theta) - 2r(1-\cos\theta) + 2\Delta\kappa + \lambda(1-\cos\theta)\big)/\sqrt{2}$
(-0)	$-1/\sqrt{r}$	$\big(1-\cos\theta + r(1+\cos\theta) + \Delta\kappa - \lambda\cos\theta\big)/\sqrt{r}$
$(-+)$	0	$-\sqrt{2/3}\,\lambda/r$
$(+-)$	0	$\sqrt{2/3}\,(2r^2 + \Delta\kappa r - \lambda(1-r))/r$
$(+0)$	0	$(-4r - \Delta\kappa(1+r) + \lambda(1+r))/\sqrt{3r}$
$(++)$	0	$-\sqrt{2}\,(2+\Delta\kappa)$

λ is:

$$\sigma^{\lambda\lambda'} = \frac{1}{4}\int d\Omega \frac{(2\pi)^4}{2s}\left|\mathcal{M}^{\lambda\lambda'}\right|^2 \frac{1-m_W^2/s}{8(2\pi)^6} = \frac{1-r}{128\pi s}\int_{-1}^{1} d(\cos\theta)\left|\mathcal{M}^{\lambda\lambda'}\right|^2$$

$$= \frac{3R}{32}(1-r)\int_{-1}^{1} d(\cos\theta)\left|\frac{\mathcal{M}^{\lambda\lambda'}}{e^2}\right|^2 .$$

Figure 18 shows the differential cross section for producing a W of various helicitiy combinations.

Figure 19 shows the dependence on κ and λ of the total cross section. These figures are the idealized cross sections, assuming monochromatic beams of perfectly polarized electrons and photons.

The most striking feature of the differential cross section for $e\gamma \to W\nu$ is the radiation zero which occurs in the Standard Model. The cross section for all helicity combinations is exactly zero when the W scatters backwards (*i.e.* in the direction of the incoming electron). The differential cross section in the $e\gamma$ center-of-mass frame is very strongly peaked for W's scattering in the forward direction (fig. 20). Since this radiation zero exists only for Standard Model couplings, the cross section for

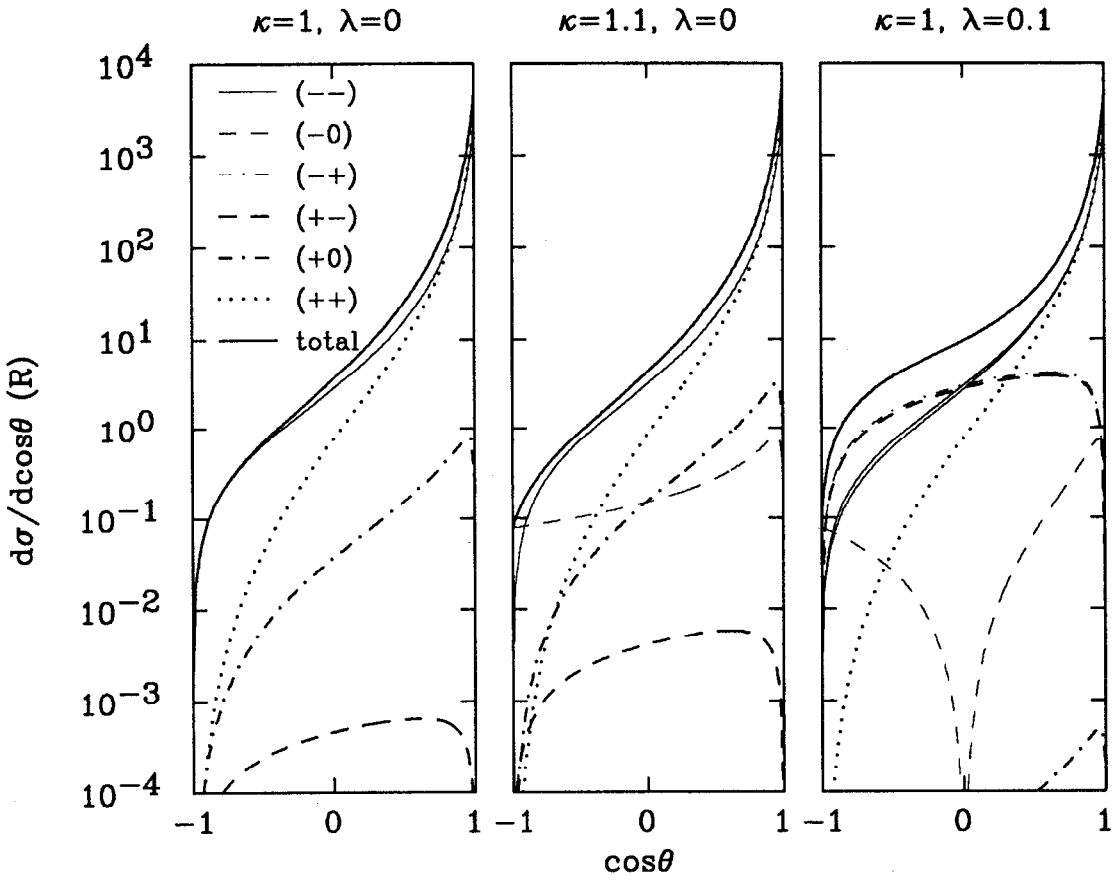

Figure 18. Differential cross sections for producing a W of specific helicity with center of mass energy of 500 GeV as a function of $\cos\theta$. In a combination $(\lambda_1\lambda_2)$, λ_1 and λ_2 are the helicities of the γ and W respectively.

backward scattering W's could be a very sensitive probe for non-Standard Model couplings.

However, in an $e\gamma$ collider, the average electron energy is significantly larger than the average photon energy, and thus the laboratory frame is boosted in the electron's direction with respect to the $e\gamma$ center-of-mass frame. The entire W angular distribution is shifted in the backward direction, completely obscuring the radiation zero. The amount of this shift is sensitive to the actual photon spectrum. An additional smearing effect is caused by the fact that, considering only the leptonic W decay mode, its momentum is not reconstructible; only the

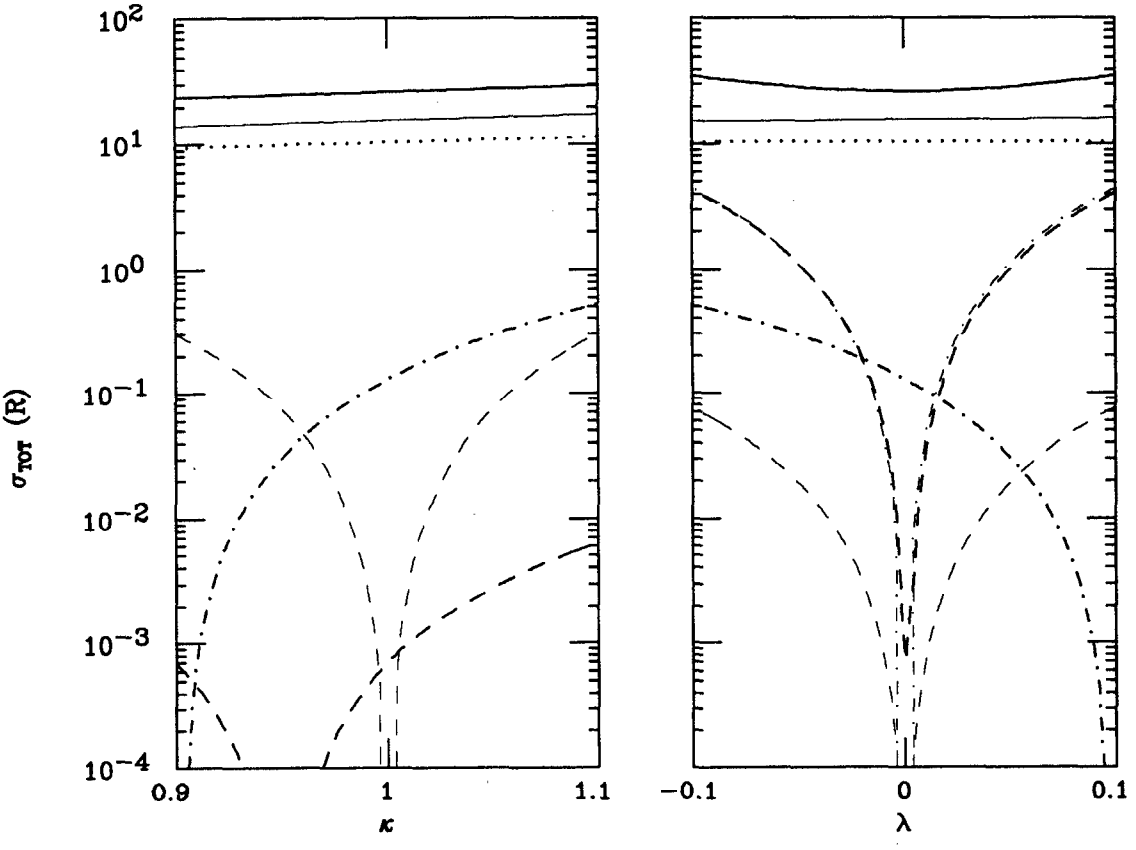

Figure 19. Total cross sections for various helicity combinations with center-of-mass energy of 500 GeV. The meaning of the lines is the same as in fig. 18.

muon's momentum is known.

Because the W momentum is not reconstructible in leptonic decay events, the relative direction of the decay products cannot be established (unlike in $e^+e^- \to W^+W^-$). While the total W momentum can be fixed with reasonable accuracy in hadronic decay events, it is questionable whether the same is true of the individual decay products. Thus, unlike $e^+e^- \to W^+W^-$, we assume here that the W polarization cannot be determined experimentally.

As we mentioned above, the total cross section for $e\gamma \to W\nu$ approaches a constant rather than dropping like $1/s$. It is interesting to note that when one imposes a fixed cut on the direction of the W accounting for the fact that particles

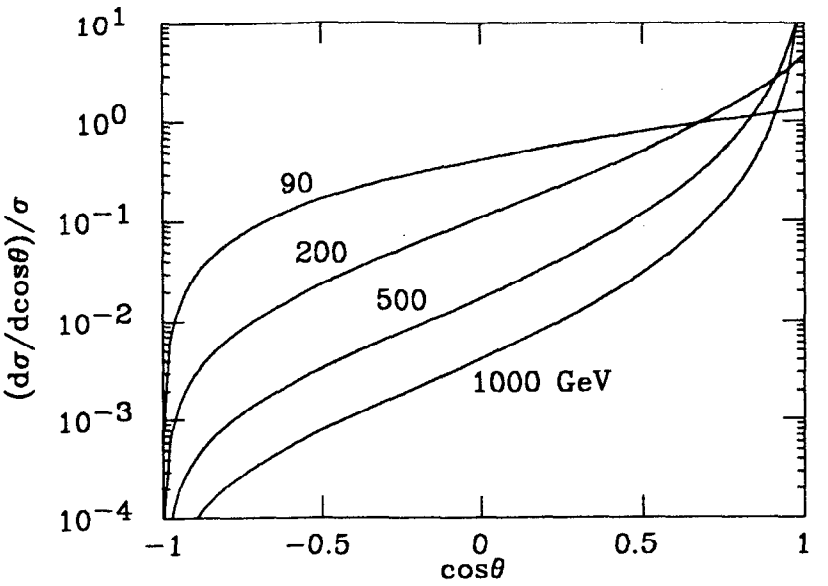

Figure 20. Differential cross section for $e\gamma \to W\nu$ in the $e-\gamma$ center-of-mass frame, for different values of center-of-mass energy. The area under each curve is 1.

near the beam pipe escape detection, the $1/s$ asymptotic behaviour is restored. This is because the cross section at higher energies becomes dominated by higher partial waves, which are improtant in the low-momentum-transfer region, making the differential cross section sharply peaked in the backward direction. Figure 21 compares the energy dependence of the cross sections of $e\gamma \to W\nu$ and $e\gamma \to e\gamma$ for cutoff angles of 20° (solid) and 2° (dashed). Note that the cross section for $e\gamma \to e\gamma$ is equally sensitive to the cutoff angle at all energies, whereas the one for $e\gamma \to W\nu$ becomes more sensitive at higher energies.

4.3 Photon Spectra

The calculations in the previous section were carried out in the setting of an 'idealized' electron-photon collider in which the photon beam is perfectly monochromatic, and is carrying the same energy as the electron beam. In this section we show how to account for the inevitable energy spread associated with realistic photon colliders.

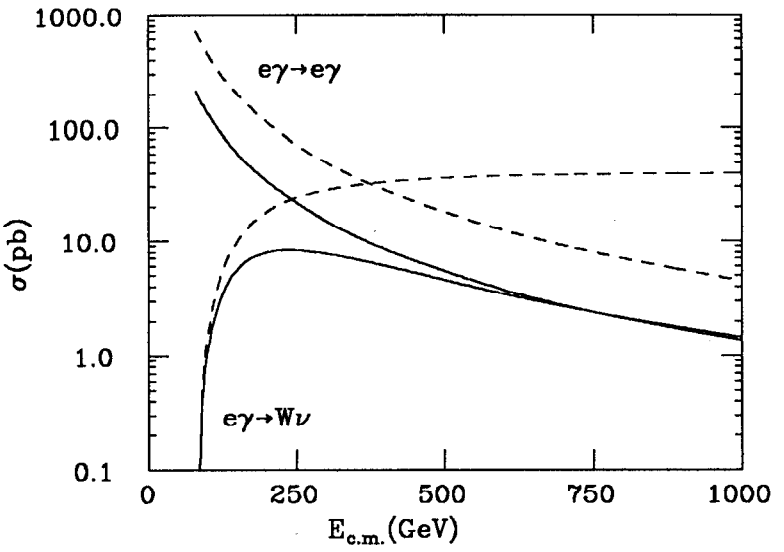

Figure 21. Total cross section for the processes $e\gamma \to W\nu$ and $e\gamma \to e\gamma$ as a function of center-of-mass energy, and subject to cuts of 37° (solid) and 2° (dashed) on the scattering angle.

To account for the distribution of electron-photon center-of-mass energy, we introduce the effective luminosity $\mathcal{L}_{e\gamma}(\hat{s})$. $\mathcal{L}_{e\gamma}(\hat{s})$ is a *dimensionless* quantity, defined as follows: the luminosity for an electron-photon collision with center-of-mass energy squared between $\hat{s}$ and $\hat{s}+d\hat{s}$ is equal to $\mathcal{L}_{e\gamma}(\hat{s})(d\hat{s}/s)$ times the overall collider luminosity.

In terms of the effective luminosity $\mathcal{L}_{e\gamma}(\hat{s})$, the cross section for $W\nu$ production is

$$\sigma = \int_0^s (d\hat{s}/s)\mathcal{L}_{e\gamma}(\hat{s})\sigma(\hat{s}). \tag{4.10}$$

We consider three potential photon sources. First, we have classical bremstrahlung. This radiation depends only on the beam energy, and is parametrized to first order by the Weizsacker-Williams distribution function

$$f(x) = \frac{\alpha \ln(s/m_e^2)}{2\pi} \cdot \frac{1+(1-x)^2}{x}, \tag{4.11}$$

where x is the fraction of the electron energy carried by the photon. To first

order in $(\alpha/2\pi)\ln(s/m_e^2) \approx 0.032$, we can ignore the electron beam energy loss, and assume it remains monochromatic. The effective luminosity function $\mathcal{L}_{e\gamma}(\hat{s})$ is then given simply by

$$\mathcal{L}_{e\gamma}(\hat{s}) = f(\hat{s}/s). \tag{4.12}$$

The second source for photons is the synchrotron radiation emitted by electrons in one beam due to the electric field it experiences as it passes through the other beam; this radiation is termed "beamstrahlung."[22,23] The effect of beamstrahlung cannot be decomposed into distribution functions. We parameterize it in terms of the luminosity function $\mathcal{L}_{e\gamma}(\hat{s})$ discussed above. Beamstrahlung depends strongly on machine parameters such as luminosity, pulse rate and bunch geometry.[22,23] Here we use the following set of accelerator parameters (designated machine G by Palmer[21]):

$$\begin{aligned} &E_{\rm cm} = 500\ {\rm GeV}, \quad \mathcal{L} = 9 \times 10^{33}{\rm cm}^{-2}{\rm sec}^{-1}, \quad N = 1.67 \times 10^{10}, \\ &B_x = 3.4 \times 10^{-5}{\rm cm}, \quad B_y = 1.3 \times 10^{-6}{\rm cm}, \end{aligned} \tag{4.13}$$

where $E_{\rm cm}$ is the center-of-mass energy, $\mathcal{L}$ is the effective luminosity, N is the number of particles per bunch and B_x and B_y are respectively the large and small radii of the elliptic pulse. This luminosity corresponds to $9 \times 10^{-3}{\rm pb}^{-1}{\rm sec}^{-1}$. In a 10^6sec year, the integrated luminosity is 9 ${\rm fb}^{-1}$ or about 3000 events per unit of R.

The third potential photon source is a deliberately constructed $e\gamma$ collider. Ginzburg *et al.*[24,25] have suggested a scheme for converting a single-pass e^+e^- collider into a $e\gamma$ (or a $\gamma\gamma$) collider. The conversion of high-energy electrons to photons is done by backward Compton scattering of high intensity laser light off the electron beam. This mechanism entails losing very little luminosity; it reduces the energy of each beam by 10-20%.

In describing the machine parameters, we use the dimensionless variables*

$$x_p = \frac{4E\omega_0}{m_e^2}, \qquad x = \frac{\omega}{E}, \tag{4.14}$$

where E is the electron beam energy (here taken to be 250 GeV), ω_0 is the energy of the laser photon and ω is the energy of the scattered photon. The parameter x_p is just (s/m_e^2) for the Compton scattering process. The maximum energy of a scattered photon is given by

$$x \leq x_m = \frac{x_p}{x_p + 1}. \tag{4.15}$$

Due to the onset of e^+e^- pair production between backscattered and laser photons, conversion efficiency drops considerably for $x_p > 2 + 2\sqrt{2} \approx 4.82$.[24,39] We assume $x_p = 2 + 2\sqrt{2}$, which, given 250 GeV electrons, corresponds to laser energy ω_0 of about 1.2 eV.

The photon spectrum depends sensitively on $\lambda_e P_c$, where λ_e is the mean electron helicity and P_c is the mean laser photon helicity. Larger negative values of $\lambda_e P_c$ give a harder, more monochromatic photon spectrum, resulting in larger effective cross sections. See ref. 39 for a thorough discussion of the experimental consequences of electron beam polarization. The sensitivity to anomalous couplings, however, does not increase significantly with a harder photon spectrum, while measuring the actual λ_e introduces new systematic errors. Therefore, we assume that the electron beam is unpolarized. On the other hand, the laser can be easily polarized almost completely, and this polarization can serve as an important experimental tool. We assume that $|P_c| = 1$. The effective luminosity is given

---

⋆ Our x_p and x correspond to ref. 24's x and y respectively. For simplicity we use $k = 1$, $\alpha_0 = 0$ and $\theta_0 = 0$ (which implies $\rho = 0$.)

by[24]

$$\begin{aligned}\mathcal{L}_{e\gamma}(\hat{s}) =& \mathcal{L}_{e\gamma}(xs) \\ =& \frac{2(1+x_p)^2}{(1-x)^2}\left(2x_p^2 - 4x_p x - 4x_p^2 x + 4x^2 + 4x_p x^2 + 3x_p^2 x^2 - x_p^2 x^3\right) \Big/ \\ & \Big[x_p\left(16 + 32x_p + 18x_p^2 + x_p^3\right) \\ & - 2\left(8 + 20x_p + 15x_p^2 + 2x_p^3 - x_p^4\right)\log(1+x_p)\Big].\end{aligned} \tag{4.16}$$

Fig. 22 shows the three photon spectra used here.

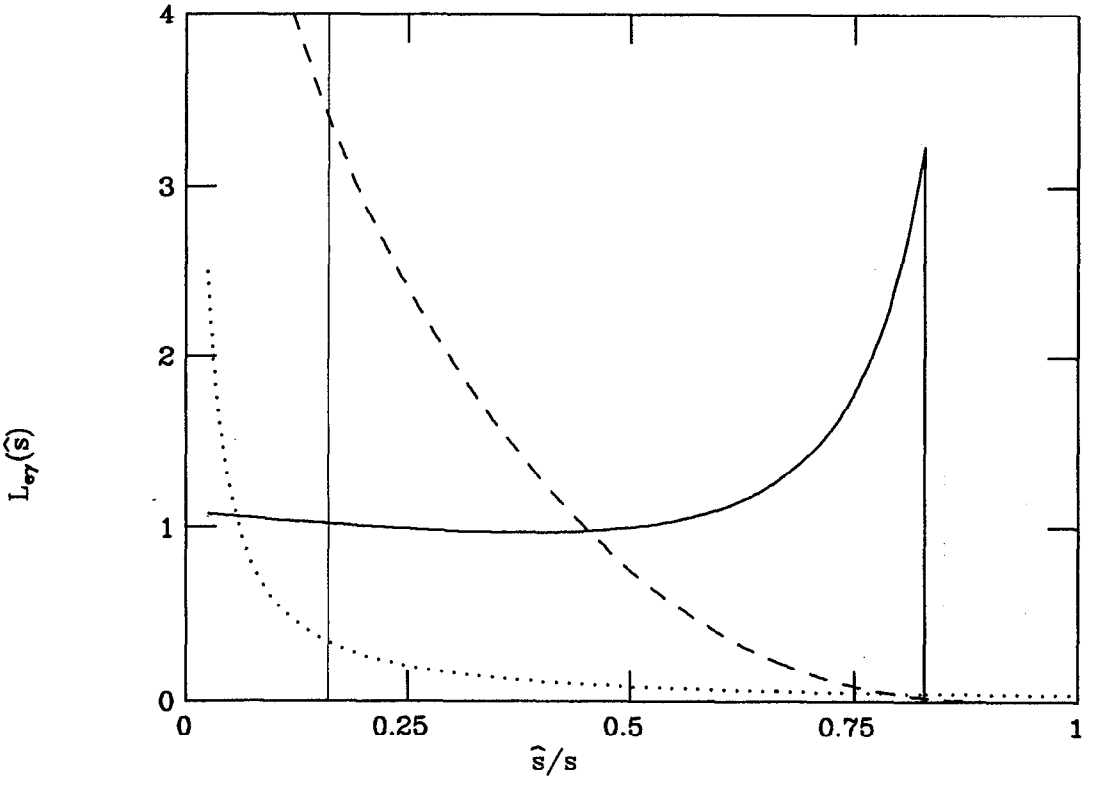

Figure 22. Effective luminosity $\mathcal{L}_{e\gamma}$ as a function of $\hat{s}/s$, where $\hat{s}$ is the center-of-mass energy squared of the $e-\gamma$ system. The solid curve is the Compton backscattered effective luminosity. The dashed curve is the beamstrahlung effective luminosity. The dotted curve is the classical Weizsacker-Williams spectrum. The the thin vertical line represents the W production threshold.

The various measureables associated with $e\gamma \to W\nu$ are sensitive to the actual photon luminosity. Therefore, the question of measuring this luminosity with sufficient accuracy becomes prominent. As it turns out, ordinary Compton scattering provides a simple yet effective method for measuring the photon spectrum. It provides both a large cross section and therefore good statistics, and a virtually background-free event topology. The process $e\gamma \to e\gamma$, with both final particles visible and no missing perpendicular momentum has no background beyond radiative corrections. Furthermore, the momenta of the incoming particles can be reconstructed completely. The cross section for $e\gamma \to e\gamma$ is

$$d\sigma = \frac{2\pi\alpha\ 2\mathcal{L}_{e\gamma}(\hat{s})(d\hat{s}/s)}{\hat{s}} \int \frac{5 + 2\cos\theta + \cos\ 2\theta}{1 + \cos\theta} d(\cos\theta). \tag{4.17}$$

The infrared divergence is avoided by cutting off the θ integral at some finite θ_0. This is justified since, experimentally, no detection is possible for small beam particle angles.

In units of R, one gets

$$d\sigma(\hat{s}) = \mathcal{L}_{e\gamma}(\hat{s})\frac{d\hat{s}}{\hat{s}} \cdot 3\left(\cos\theta_0 + 2\log\left(\frac{1+\cos\theta_0}{1-\cos\theta_0}\right)\right), \tag{4.18}$$

where θ_0 is the minimal angle from the beam direction in which particles can be detected. Equation (4.18) allows a straightforward determination of $\mathcal{L}_{e\gamma}(\hat{s})$ by measuring the cross section for $e\gamma$ production in a given $\hat{s}$ bin.

In the case of a Compton backscattered $e\gamma$ collider, we also consider the question of photon polarization. Using a polarized laser beam results in a polarized backscattered beam. The amount of polarization is energy dependent. If the laser beam polarization does not have linear component, coherence between left- and right- handed photons is lost upon integration over the azimuthal angle of the Compton scattering process. Since the photons are emitted within 0.1 mrad of the electron direction, the angle is unobservable, and the integration is done automat-

ically. The average helicity ξ_2 of the photon beam is then given by[24]

$$\xi_2 = -\frac{x_p(x_p - 2x - x_p x)(2 - 2x + x^2)}{2x_p^2 - 4x_p x - 4x_p^2 x + 4x^2 + 4x_p x^2 + 3x_p^2 x^2 - x_p^2 x^3}. \tag{4.19}$$

Fig. 23 compares the total photon spectrum to that of photons with helicity $-P_c$.

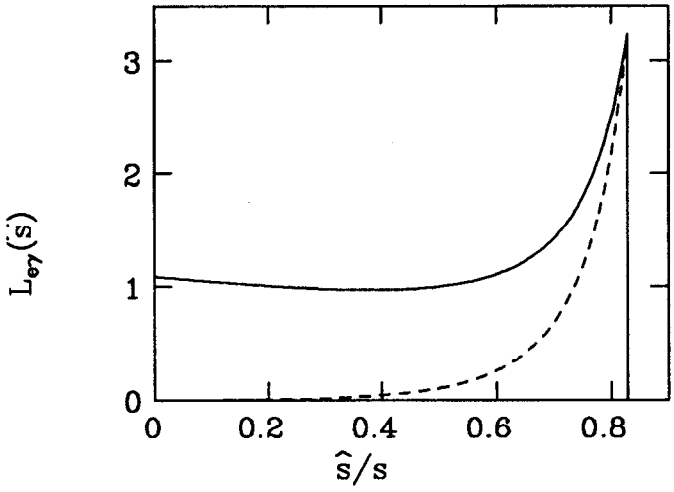

Figure 23. Spectrum of photons with helicity $-P_c$ (dashes) and the total spectrum (solid).

4.4 Observables

In this section we discuss the various observables and assess their sensitivity to κ and λ. All the calculations in this section are performed for machines based on a 500 GeV e^+e^- collider. We repeat the calculations using the three photon spectra discussed in the previous section. In the case of a Compton backscattered photon beam, we also use the partial polarization of the photon beam (eqn. (4.19)) induced by the polarization of the incident laser beam.

As with $e^+e^- \to W^+W^-$, we start with the total cross section. The angular integration over the direction of the W in the $e\gamma$ center-of-mass frame is cut at $|\cos\theta| = 0.8$. We assume systematic errors in measuring the total cross section

to be 5%. The total cross section depends on the photon spectra used, but even the Weizsacker-Williams spectrum gives 5.8 R, corresponding to over 17000 events. Statistical errors are, thus, negligible compared with systematic ones. Figure 24 shows the total cross section for $e\gamma \to W\nu$ as a function of κ for several values of λ. The calculations were performed using the three photon spectra. Figure 25 shows its dependence on λ for several values of κ.

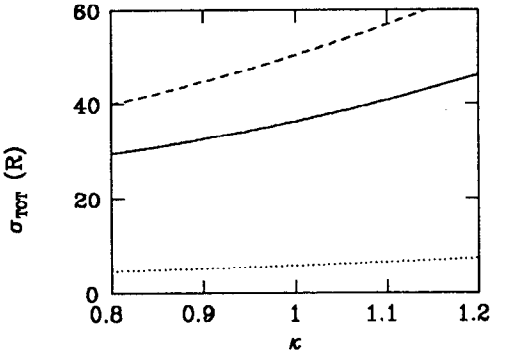

Figure 24. $\sigma_{\rm TOT}$ for $e\gamma \to W\nu$ as a function of κ for $\lambda = 0$. Here and henceforth, the solid curves correspond to the Compton backscattered spectrum. The dashed curves are computed using the beamstrahlung effective luminosity. The dotted curves correspond the the Weizsacker-Williams distribution.

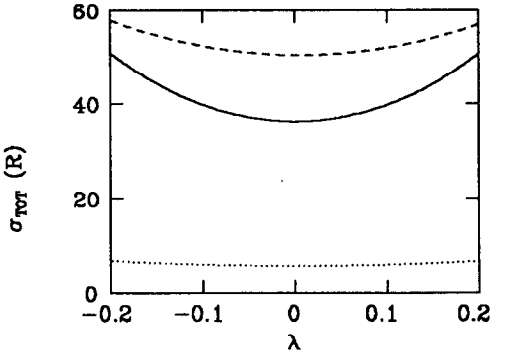

Figure 25. $\sigma_{\rm TOT}$ for $e\gamma \to W\nu$ as a function of λ for $\kappa = 1$.

The forward-backward asymmetry, defined in eqn. (3.22), can be measured with the entire event sample. We assume that FB can be measured with systematic error of 0.03. Figures 26 and 27 show its dependence on κ and λ.

IO (eqn. (3.23)) gives a complementary parameter of the W production angular distribution. Here we assume that IO can be measured with systematic error of 0.03. Figures 28 and 29 show its dependence on κ and λ.

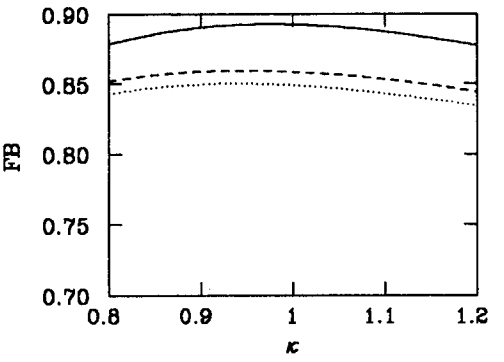

Figure 26. FB as a function of κ for $\lambda = 0$.

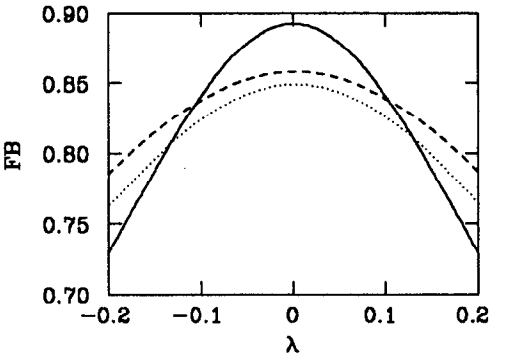

Figure 27. FB as a function of λ for $\kappa = 1$.

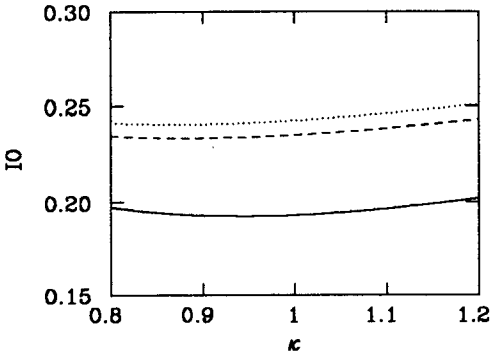

Figure 28. IO as a function of κ for $\lambda = 0$.

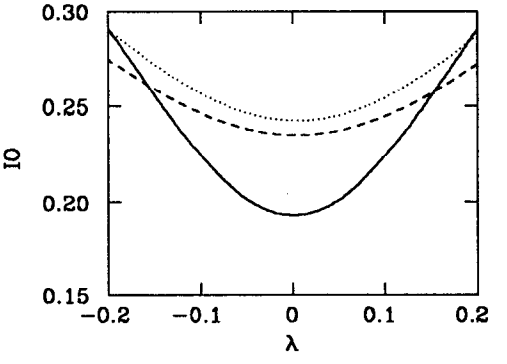

Figure 29. IO as a function of λ for $\kappa = 1$.

In a dedicated $e\gamma$ collider constructed by the Compton backscattering mechanism discussed in the previous section, a circular polarization of the incident laser beam results in a partial, energy-dependent polarization of the high-energy photon beam (eqn. (4.19)). The most energetic photons are always polarized with opposite helicity with respect to the laser photons. We define the two configurations corresponding to the two possible laser polarizations as $J_z = 3/2$ and $J_z = 1/2$ dominated, according to the combined spin of the left-handed electrons and the

most energetic photons. We emphasize that the J_z tag holds only for the most energetic photons. Lower energy photons have both possible helicities. The cross section calculations are carried out with the actual helicity spectrum of eqn. (4.19).

The ratio

$$(1/3) = \frac{\sigma(J_z = 1/2 \text{ dominated})}{\sigma(J_z = 3/2 \text{ dominated})} \tag{4.20}$$

is another, independent, measureable quantity. Lasers can be easily and accurately polarized, and therefore virtually all systematic errors are canceled in measuring this ratio. We assume it can be measured with systematic error of 0.01. Let us stress that this measurement does not require the electron beam to be polarized. Figures 30 and 31 show the ratio's dependence on κ and λ.

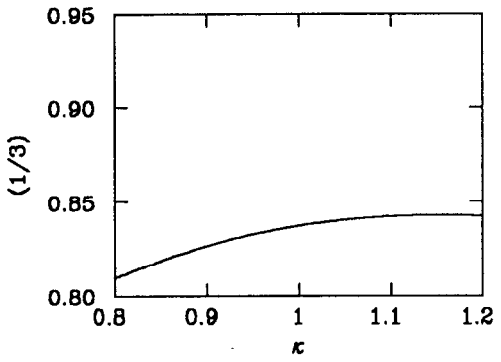

Figure 30. (1/3) as a function of κ for $\lambda = 0$.

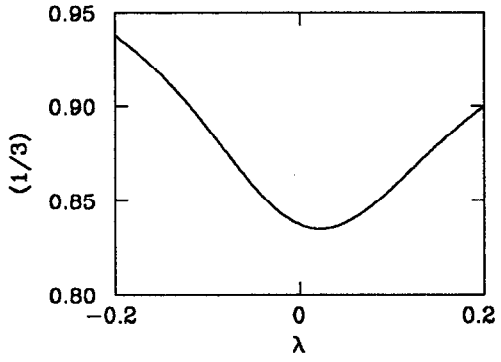

Figure 31. (1/3) as a function of λ for $\kappa = 1$.

4.5 Discovery limits

We repeat the analysis described in section 3.5 to the observables described in the previous section. Figures 32 and 33 show the (2σ) regions for each observable discussed in the previous section, as well as the 68% and 90% confidence level bounds. The calculations were repeated for each of the three photon spectra.

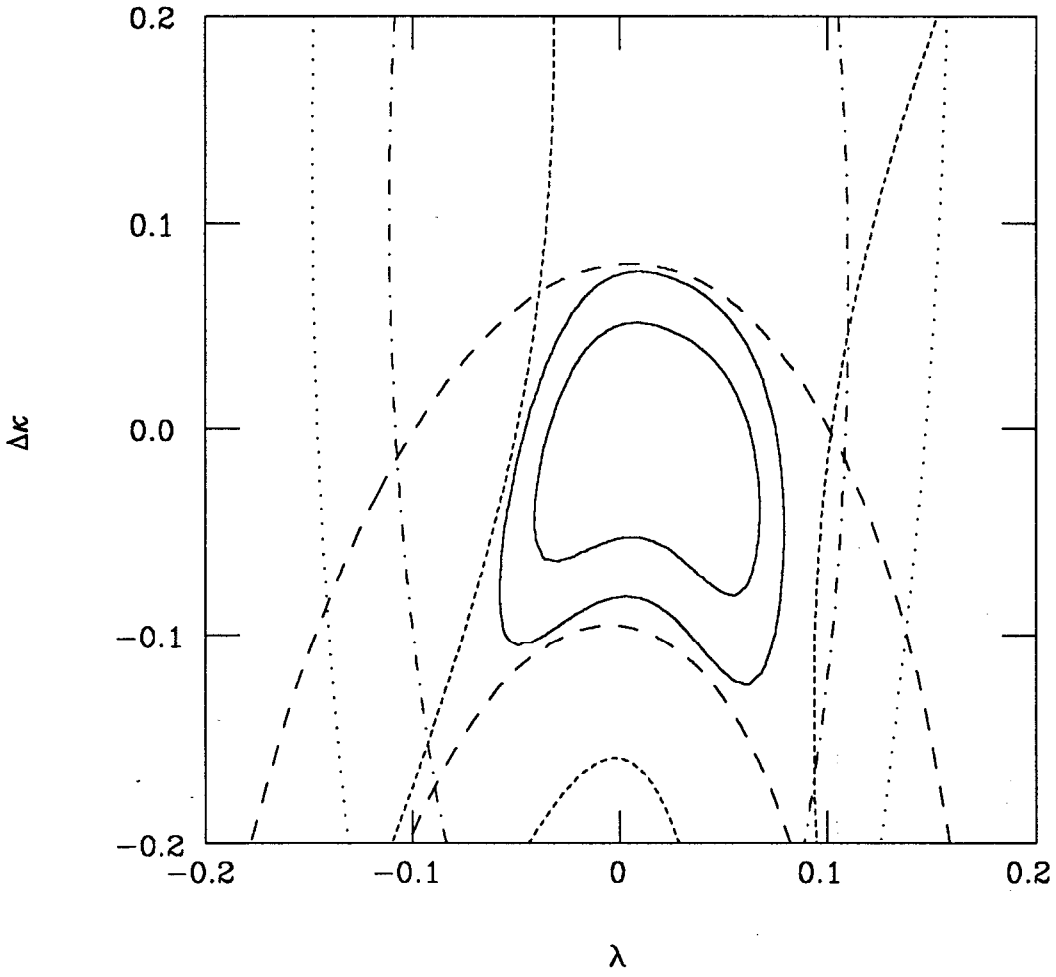

Figure 32. The (2σ) regions in the κ-λ plane from various measurements of $e\gamma \to W\nu$: $\sigma_{\rm TOT}$ (long dashed), FB (dot-dash), IO (dotted) and (1/3) (short dashed). The solid curves correspond to 68% and 90% confidence level bounds from the combination of all measurements. All calculations were done using the Compton backscattered spectrum.

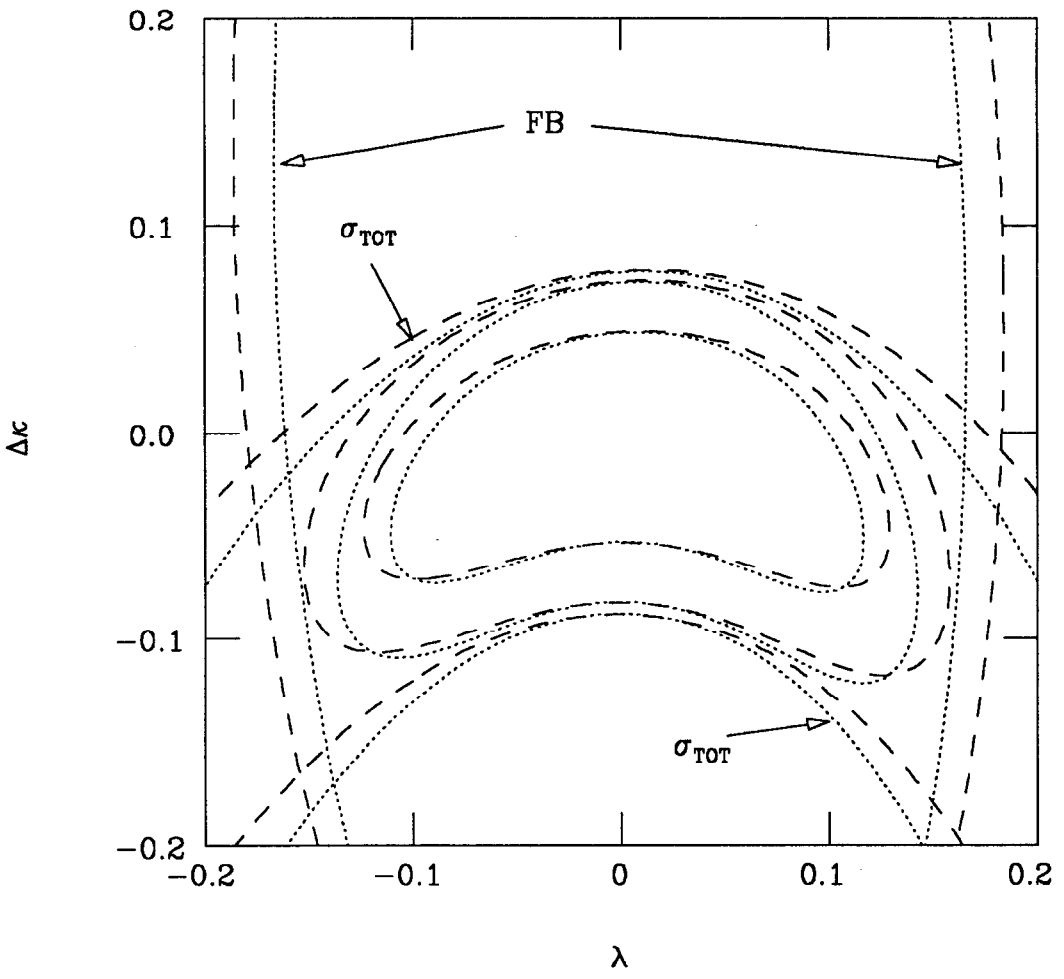

Figure 33. The (2σ) regions in the κ-λ plane from various measurements of $e\gamma \to W\nu$ using the beamstrahlung (dashed) and the Weizsacker-Williams (dotted) spectra. The regions in the center correspond to 68% and 90% confidence level bounds from the combination of all measurements.

5. $\gamma\gamma \rightarrow W^+W^-$

5.1 Introduction

The third process we study is $\gamma\gamma \rightarrow W^+W^-$. While not quite as sensitive as $e^+e^- \rightarrow W^+W^-$ to deviations from the Standard Model, it has many attractive features, making it possibly the most interesting process in a $\gamma\gamma$ collider in the 300 GeV - 1 TeV energy range. Like $e\gamma \rightarrow W\nu$, $\gamma\gamma \rightarrow W^+W^-$ involves a t-channel exchange of a heavy vector boson, and correspondingly a relatively large cross section at higher energies.

Because two $WW\gamma$ vertices appear in the Feynman diagrams for the process, the anomalous couplings can appear to fourth power in the expressions for the cross section. That greatly inhances the sensitivity to large deviations from the Standard Model. Although $\gamma\gamma \rightarrow W^+W^-$ involves only $W\gamma$ couplings, its analysis is complicated because the four vector vertex $WW\gamma\gamma$ as well as the three vector vertex $WW\gamma$ contributes. In this work, we do not consider the most general $WW\gamma\gamma$ vertex. Rather, we use the simplest one satisfying the electromagnetic Ward identity. This simple consistency requirement forces the $WW\gamma\gamma$ vertex to depend on λ.[32]

This chapter proceeds as follows. In the next section we introduce the $WW\gamma\gamma$ vertex, and outline the calculation of the production cross section in the setting of an 'idealized' $\gamma\gamma$ collider. In sect. 3 we describe the effective $\gamma\gamma$ luminosity expected from different sources. Section 4 evaluates potential observables, calculating their dependence on κ and λ. Section 5 assesses possible bounds on κ and λ from the individual measurements, and combines them to give specific confidence limits in the κ-λ plane.

Cross section calculations for $\gamma\gamma \to W^+W^-$ proceed much like those for the previous processes. $\gamma\gamma \to W^+W^-$ is conceptually simpler because no spinors are involved. As the $WW\gamma$ vertex appears twice in two of the Feynman diagrams, the expressions for the helicity amplitudes are quadratic in κ and λ. The three Feynman diagrams contributing to $\gamma\gamma \to W^+W^-$ are shown in fig. 34.

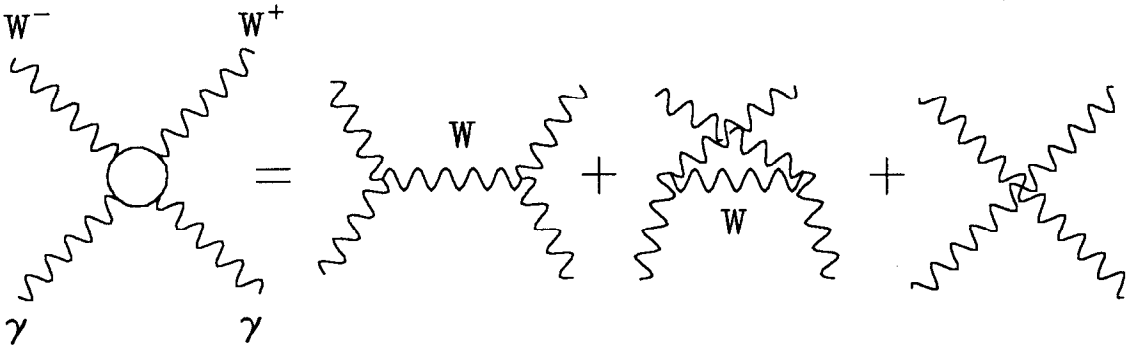

Figure 34. Feynman diagrams for $\gamma\gamma \to W^+W^-$.

The $WW\gamma$ vertices have the same kinematics as the vertex in $e\gamma \to W\nu$ (eqn. (4.1)), with the obvious changes in the assignment of indices and momenta. Unlike the $WW\gamma$ vertex, the $WW\gamma\gamma$ vertex has not been systematically analyzed. Here we do not use its most general form. Instead, we use the simplest form which is still consistent with eqn. (4.1) in the sense of maintaining electromagnetic gauge invariance.[32] This general form, with momenta labeled as in fig. 35, is given by

$$
\begin{aligned}
i\Gamma^{\mu\nu\tau\sigma} = ie^2\Big[& 2g^{\mu\nu}g^{\sigma\tau} - g^{\mu\tau}g^{\nu\sigma} - g^{\mu\sigma}g^{\nu\tau} \\
& + \frac{\lambda}{m_W^2}\Big\{ g^{\mu\tau}g^{\nu\sigma}\big((p_4\cdot p_1)+(p_3\cdot p_2)\big) + g^{\mu\sigma}g^{\nu\tau}\big((p_4\cdot p_2)+(p_3\cdot p_1)\big) \\
& - g^{\mu\nu}g^{\tau\sigma}\big(p_4+p_3\big)^2 + 2g^{\mu\nu}p_4{}^{\tau}p_3{}^{\sigma} + 2g^{\sigma\tau}p_2{}^{\mu}p_1{}^{\nu} \\
& - g^{\mu\tau}\big(2p_4{}^{\nu}p_3{}^{\sigma}+2p_3{}^{\nu}p_2{}^{\sigma}-p_4{}^{\nu}p_2{}^{\sigma}\big) - g^{\mu\sigma}\big(2p_4{}^{\tau}p_3{}^{\nu}+2p_4{}^{\nu}p_2{}^{\tau}-p_3{}^{\nu}p_2{}^{\tau}\big) \\
& - g^{\nu\tau}\big(2p_4{}^{\mu}p_3{}^{\sigma}+2p_3{}^{\mu}p_2{}^{\sigma}-p_4{}^{\mu}p_1{}^{\sigma}\big) - g^{\nu\sigma}\big(2p_4{}^{\tau}p_3{}^{\mu}+2p_4{}^{\mu}p_1{}^{\tau}-p_4{}^{\mu}p_1{}^{\tau}\big)\Big\}\Big].
\end{aligned}
\tag{5.1}
$$

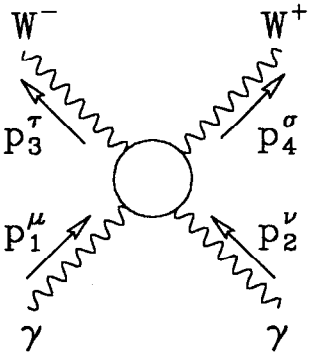

Figure 35. The $WW\gamma\gamma$ vertex.

The matrix element (in unitary gauge) is given by

$$
\begin{aligned}
\mathcal{M}_{\lambda_1,\lambda_2,\lambda_3,\lambda_4} &= \varepsilon^{\mu}(p_1,\lambda_1)\,\varepsilon^{\nu}(p_2,\lambda_2)\,\varepsilon^{\tau *}(p_3,\lambda_3)\,\varepsilon^{\sigma *}(p_4,\lambda_4)\mathcal{M}_{\mu\nu\tau\sigma} \\
i\mathcal{M}_{\mu\nu\tau\sigma} &= (i\Gamma_{\mu\tau\rho_1})\,\frac{-i\left(g^{\rho_1\rho_2}-(p_1-p_3)^{\rho_1}(p_1-p_3)^{\rho_2}/m_W^2\right)}{t-m_W^2}\,(i\Gamma_{\nu\rho_2\sigma}) \\
&\quad + (i\Gamma_{\mu\rho_1\sigma})\,\frac{-i\left(g^{\rho_1\rho_2}-(p_1-p_4)^{\rho_1}(p_1-p_4)^{\rho_2}/m_W^2\right)}{u-m_W^2}\,(i\Gamma_{\nu\tau\rho_2}) \\
&\quad + i\Gamma_{\mu\nu\tau\sigma}.
\end{aligned}
\tag{5.2}
$$

λ_1, λ_2, λ_3 and λ_4 are the helicities of the two photons, the W^- and the W^+

respectively. λ_1 and λ_2 take the values -1 and 1. λ_3 and λ_4 take the values -1, 0 and 1.

The momenta p_{1-4} are the same as in $e^+e^- \to W^+W^-$ (eqn. (3.6)). The photon polarization vectors $\lambda_{1,2}$ are given by

$$\varepsilon(p_1,\pm) = \frac{1}{\sqrt{2}}(1,\pm i,0,0) \qquad \varepsilon(p_2,\pm) = \frac{1}{\sqrt{2}}(1,\mp i,0,0). \tag{5.3}$$

The W polarization vectors are the same as in $e^+e^- \to W^+W^-$ (eqn. (3.7)).

Substituting the vertex expressions from eqns. (4.1) and (5.1) and the explicit four vectors from eqns. (3.6), (3.7) and (5.3), we get the following expressions for the matrix elements:

$$\mathcal{M}_{\lambda_1,\lambda_2,\lambda_3,\lambda_4} = \frac{4\alpha\pi d^{J_0}_{\Delta\lambda_{12},\Delta\lambda_{34}}\tilde{\mathcal{M}}_{\lambda_1,\lambda_2,\lambda_3,\lambda_4}}{1-\cos^2\theta + r\cos^2\theta}, \tag{5.4}$$

where $\Delta\lambda_{12} = \lambda_1 - \lambda_2$, $\Delta\lambda_{34} = \lambda_3 - \lambda_4$ and $J_0 = \max(|\Delta\lambda_{12}|, |\Delta\lambda_{34}|)$, and the d functions are given in table 4.

The helicity amplitudes are:

$$\tilde{\mathcal{M}}_{++00} = \frac{1}{2r}\Big[4r^2 + 8\Delta\kappa(\sin^2\theta + r\cos^2\theta) - 8\lambda r\sin^2\theta$$
$$+ \Delta\kappa^2\left(4\sin^2\theta + r(3\cos^2\theta - 1)\right) - 2\Delta\kappa\lambda r(3\cos^2\theta - 1)$$
$$+ \lambda^2(1+\cos^2\theta)\left(2\sin^2\theta + r(2\cos^2\theta - 1)\right)\Big]$$

$$\tilde{\mathcal{M}}_{++0+} = \frac{\cos\theta}{2\sqrt{r}}\Big[4\Delta\kappa(1-\beta-r) - 4\lambda(1-\beta+r) + \Delta\kappa^2(2-2\beta-r)$$
$$- 2\Delta\kappa\lambda(2+r) - \lambda^2\left(2(1+\beta)(1/r-1)\sin^2\theta + r\right)\Big]$$

$$\tilde{\mathcal{M}}_{+-00} = \frac{\sqrt{3}}{4r\sqrt{2}}\Big[4r(1+r) + 8\Delta\kappa r + \Delta\kappa^2(2+r) - 2\Delta\kappa\lambda(2-r)$$
$$+ \lambda^2\left(2\cos^2\theta + r(1-2\cos^2\theta)\right)\Big]$$

$$\tilde{\mathcal{M}}_{+-++} = \frac{1}{r\sqrt{6}}\Big[8r^2 + 8\Delta\kappa r - 16\lambda(1-r) + 3\Delta\kappa^2 r - 2\Delta\kappa\lambda(4-3r)$$
$$- \lambda^2\left(2\sin^2\theta - (3-2\cos^2\theta)r\right)\Big]$$

$$\tilde{\mathcal{M}}_{+++-} = \frac{\sqrt{3}}{8r\sqrt{2}}\Big[-8\lambda(2-r) + \Delta\kappa^2 r - 2\Delta\kappa\lambda(4-r)$$
$$- \lambda^2\left(2\sin^2\theta + (2\cos^2\theta - 1)r\right)\Big]$$

$$\tilde{\mathcal{M}}_{+-0+} = \frac{-1}{\sqrt{2r}}\Big[8r + 4\Delta\kappa(1+r) - 4\lambda(1-r) + \Delta\kappa^2(3+\cos\theta - r\cos\theta)$$
$$- \Delta\kappa\lambda\left(4(1+\cos\theta)/r - 2(1+3\cos\theta) + 2r\cos\theta\right)$$
$$+ \lambda^2\left(2(1+\cos\theta)^2/r - (1+\cos\theta)(1+2\cos\theta) + r\cos^2\theta\right)\Big]$$

$$
\begin{aligned}
\tilde{\mathcal{M}}_{++++} =& \frac{-1}{4r}\Big[8r(2-2\beta-r) + 8\Delta\kappa r(2-\beta-\beta\cos^2\theta) \\
& - 8\lambda\left(2(1+\beta)\sin^2\theta - r(1-\beta-3\cos^2\theta-\beta\cos^2\theta)\right) \\
& + \Delta\kappa^2\left(2(1+\beta)\sin^2\theta + r(3+3\cos^2\theta-2\beta\cos^2\theta)\right) \\
& - 2\Delta\kappa\lambda\left(2(1+\beta)\sin^2\theta - r(3-5\cos^2\theta-2\beta\cos^2\theta)\right) \\
& + \lambda^2\big(4(1+\beta)\sin^2\theta(1-3\cos^2\theta)/r \\
& - 2(6+3\beta-13\cos^2\theta-9\beta\cos^2\theta+3\cos^4\theta+2\beta\cos^4\theta) \\
& + r(3-11\cos^2\theta-2\beta\cos^2\theta+2\cos^4\theta)\big)\Big] \\
\tilde{\mathcal{M}}_{+-+-} =& \frac{1}{r}\Big[8r + 8\Delta\kappa r + \Delta\kappa^2\left(2(1-\cos\theta) + (1+2\cos\theta)r\right) \\
& - 2\Delta\kappa\lambda\left(2(1-\cos\theta) - (1-2\cos\theta)r\right) + \lambda^2\big(4(1-\cos\theta)(3-\cos\theta)/r \\
& - 2(6-11\cos\theta+3\cos^2\theta) + (1-6\cos\theta+2\cos^2\theta)r\big)\Big],
\end{aligned}
\tag{5.5}
$$

where $r = 4m_W^2/s$ and $\beta = \sqrt{1-r}$.

The other amplitudes are related to those by the following relations:

$$
\begin{aligned}
\mathcal{M}_{\lambda_1,\lambda_2,\lambda_3,\lambda_4} &= \mathcal{M}_{-\lambda_1,-\lambda_2,-\lambda_3,-\lambda_4} \\
\mathcal{M}_{\lambda_1,\lambda_2,\lambda_3,\lambda_4} &= \mathcal{M}_{\lambda_2,\lambda_1,\lambda_3,\lambda_4} \quad (\cos\theta \to -\cos\theta) \\
\mathcal{M}_{\lambda_1,\lambda_2,\lambda_3,\lambda_4} &= \mathcal{M}_{\lambda_1,\lambda_2,\lambda_4,\lambda_3} \quad (\cos\theta \to -\cos\theta) \\
\mathcal{M}_{\lambda_1,\lambda_2,\lambda_3,\lambda_4} &= \mathcal{M}_{\lambda_1,\lambda_2,-\lambda_4,-\lambda_3} \quad (\beta \to -\beta)
\end{aligned}
\tag{5.6}
$$

Figure 36 shows the differential cross section for producing a W pair of various helicity combinations.

Figure 37 shows the dependence on κ and λ of the differential cross section at

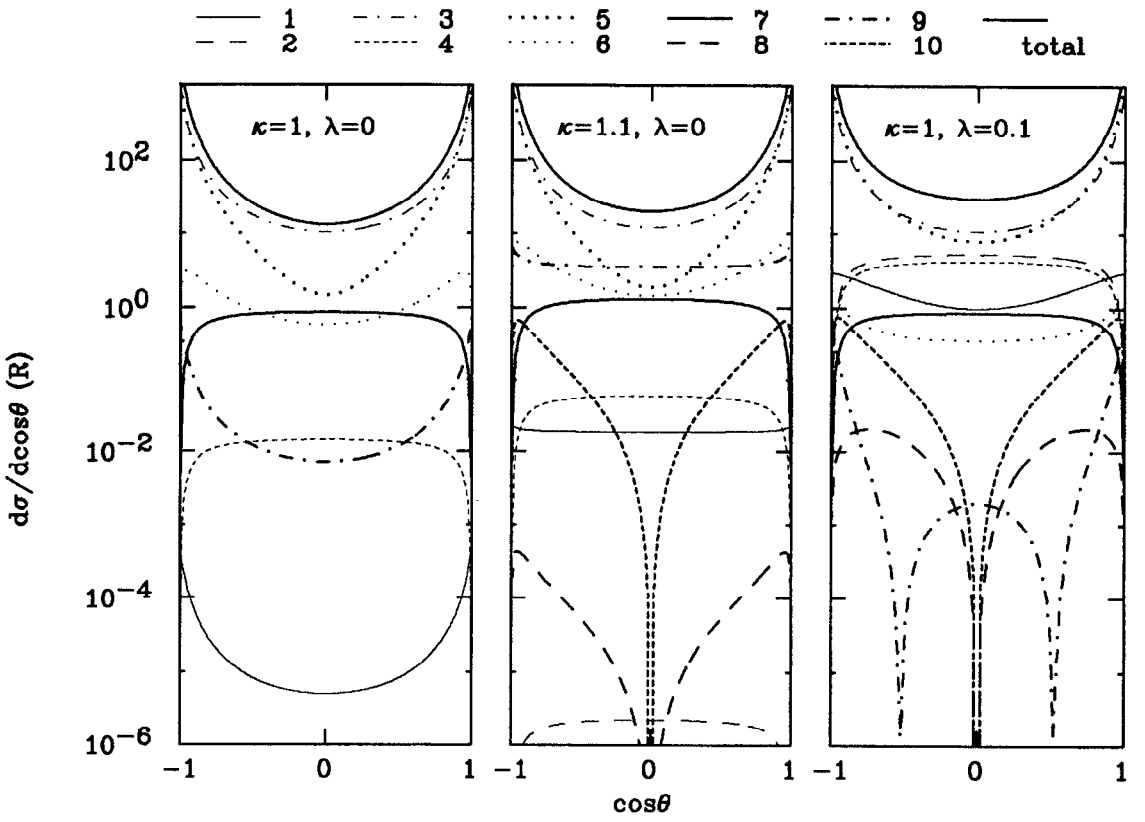

Figure 36. Differential cross sections for producing a W pair of specific helicity combination with center of mass energy of 500 GeV as a function of $\cos\theta$. The curves are:
1: $(++++)+(----)$, 2: $(+++-)+(++-+)+(--+-)+(---+)$,
3: $(++--)+(--++)$, 4: $(+-++)+(-+++)+(+---)+(-+--)$,
5: $(+-+-)+(-+-+)+(-++-)+(+--+)$,
6: $(+-0+)+(-+0-)+(+--0)+(-++0)+(+-+0)+(-+-0)+(+-0-)+(-+0+)$,
7: $(+-00)+(-+00)$, 8: $(++0+)+(--0-)+(+++0)+(---0)$,
9: $(++00)+(--00)$, 10: $(++0-)+(++-0)+(--0+)+(--+0)$.
In a combination $(\lambda_1\lambda_2\lambda_3\lambda_4)$, λ_1, λ_2, λ_3 and λ_4 are the helicities of the two photons, the W^+ and the W^- respectively.

$\cos\theta = 0$. These figures are the idealized cross sections, assuming monochromatic beams of perfectly polarized electrons and photons.

There are several points worth noting:

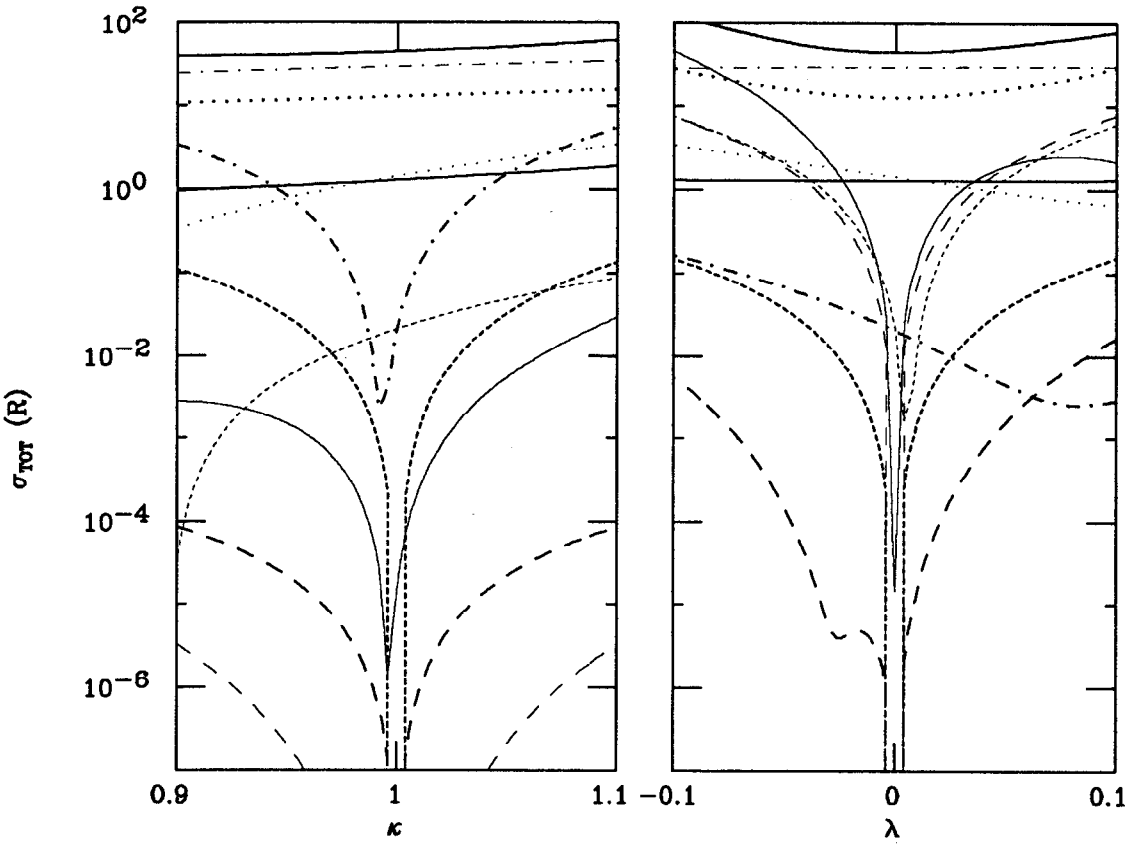

Figure 37. Total cross sections for producing W pairs of specific helicity combination with center of mass energy of 500 GeV. The meaning of the lines is the same as in fig. 36.

1. The cross section for producing two opposite-helicity W's from an initial state with total spin component along beam axis $J_z = 0$ ($(++-)$ term) is exactly zero in the Standard Model.

2. The cross section for producing one longitudinal and one transverse W from a $J_z = 0$ initial state ($(++0+)$ term) is exactly zero in the Standard Model.

3. The differential cross section at $\cos\theta = 0$ for producing one longitudinal and one transverse W from a $J_z = 0$ state ($(++0+)$ term) is exactly zero for all values of κ and λ.*

* The reason for this is as follows. The initial state has to have an even angular momen-

4. The cross section for producing two longitudinal W's from a $J_z = 0$ photon combination is suppressed by a factor of m_W^2/s in the Standard Model. The same factor is known to appear in the production of charged scalars ($\gamma\gamma \to \pi^+\pi^-$.)

5. The cross section for producing two right- (left-) handed W bosons from two left- (right-) handed photons is suppressed by a factor of $(m_W^2/s)^2$.

As in $e^+e^- \to W^+W^-$, information about the polarization of a W boson can be obtained by looking at the angular distribution of its decay products (eqns. (3.19)-(3.21)). The ratio between left- and right-handed W bosons is related to the χ forward-backward asymmetry $\chi_{\rm FB}$ by

$$\chi_{\rm FB} = \frac{\sigma(\cos\chi > 0) - \sigma(\cos\chi < 0)}{\sigma(\cos\chi > 0) + \sigma(\cos\chi < 0)} = \frac{3}{4}\frac{\sigma_{-1} - \sigma_1}{\sigma_{\rm TOT}}. \tag{5.7}$$

5.3 Photon Spectra

The calculations in the previous section were carried out in the setting of an 'idealized' photon-photon collider in which the photon beams are perfectly monochromatic and carry identical energy. In this section we discuss some realistic photon-photon collision schemes.

In analogue to $\mathcal{L}_{e\gamma}$ we define the effective luminosity $\mathcal{L}_{\gamma\gamma}(\hat{s})$ as follows: the luminosity for a photon-photon collision with center-of-mass energy squared between $\hat{s}$ and $\hat{s} + d\hat{s}$ is equal to $\mathcal{L}_{\gamma\gamma}(\hat{s})(d\hat{s}/s)$ times the overall collider luminosity. In terms of that effective luminosity, the cross section for $\gamma\gamma \to W^+W^-$ is

$$\sigma = \int_0^s (d\hat{s}/s)\mathcal{L}_{\gamma\gamma}(\hat{s})\sigma(\hat{s}). \tag{5.8}$$

We consider the same three photon sources of the previous chapter. In the

tum J. The angular dependence of the matrix element is then of the form $d^J_{0,\pm1}(\theta) = d^1_{0,\pm1}(\theta)P(\cos\theta) = \mp\sin\theta P(\cos\theta)/\sqrt{2}$ where P is an odd polynomial, which vanishes at $\cos\theta = 0$. I am grateful to Ken-ichi Hikasa for pointing out this explanation.

case of the classical bremsstrahlung radiation, the effective luminosity is given by folding the distribution function $f(x)$ (eqn.(4.11)) with itself.

$$\sigma = \int_0^1 dx_1 \int_0^1 dx_2 f(x_1) f(x_2) \sigma(x_1 x_2 s). \tag{5.9}$$

Defining $\hat{s} = x_1 x_2 s$ and changing variables gives

$$\sigma = \int_0^s (d\hat{s}/s) \left[\int_{\hat{s}/s}^1 \frac{dx_1}{x_1} f(x_1) f\left(\frac{\hat{s}/s}{x_1}\right) \right] \sigma(\hat{s}), \tag{5.10}$$

from which one can read the expression for $\mathcal{L}_{\gamma\gamma}(\hat{s})$:

$$\mathcal{L}_{\gamma\gamma}(\hat{s}) = \int_{\hat{s}/s}^1 \frac{dx_1}{x_1} f(x_1) f\left(\frac{\hat{s}/s}{x_1}\right). \tag{5.11}$$

Substituting the expression for $f(x)$ one gets

$$\mathcal{L}_{\gamma\gamma}(\hat{s}) = \frac{s}{\hat{s}} \left[\frac{\alpha \ln(s/m_e^2)}{2\pi} \right]^2 \left[-6 + 4\hat{s}/s + 2(\hat{s}/s)^2 + (\hat{s}/s + 2)^2 \log(s/\hat{s}) \right]. \tag{5.12}$$

The second photon source we consider is beamstrahlung. As we mentioned in the previous chapter, the beamstrahlung effects cannot be decomposed into distribution functions. The effective luminosity has to be calculated directly. We use again the parameters of eqn. (4.13).

The third potential photon source is a dedicated $\gamma\gamma$ collider constructed by the Compton backscattering mechanism discussed in sect. 4.3. Folding the spectra of the two photon beams can be done analytically (same as in eqn. (5.11)), but the result is long and unilluminating.

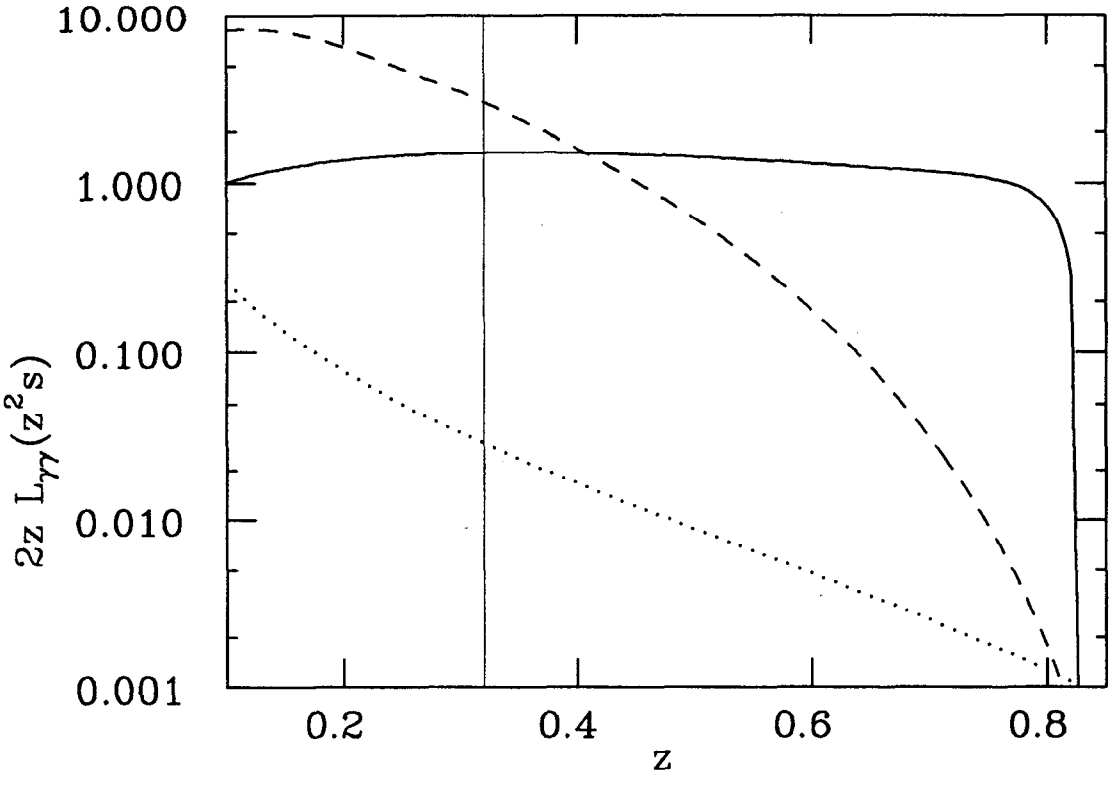

Figure 38. Effective luminosity $2z\mathcal{L}_{\gamma\gamma}(z^2 s)$ as a function of $z = \sqrt{\hat{s}/s}$, where $\hat{s}$ is the center-of-mass energy squared of the $\gamma-\gamma$ system. The solid curve is the Compton backscattered effective luminosity. The dashed curve is the "beamstrahlung" effective luminosity. The dotted curve is the classical Weizsacker-Williams spectrum. The vertical dotted line represents W production threshold.

Fig. 38 shows the effective luminosity associated with each of the three photon spectra used here.

As before, in the case of Compton backscattered beams, the photon beams acquire partial, energy dependent polarization if the incident laser beam is polarized. Figure 39 shows the total effective luminosity, and the effective luminosity for $|J_z| = 0, 2$ where J_z is the spin component along the beam axis.

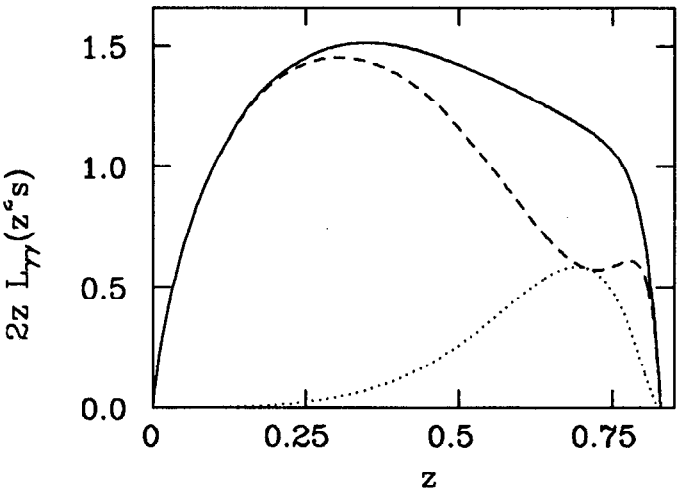

Figure 39. Effective luminosity for collisions with $|J_z| = 2$ (dashed) and 0 (dots). The total effective luminosity is given by the solid curve. The role of the $|J_z| = 2$ and $|J_z| = 0$ cruves can be interchanged by flipping the polarization of one of the laser sources.

5.4 Observables

In this section we discuss the various observables and calculate their dependence on κ and λ. Calculations are performed for machines based on a 500 GeV e^+e^- collider. We repeat the calculations using the three photon sources discussed in the previous section. In the case of a Compton backscattered photon beams, we also use the partial polarization of the photon beam (eqn. (4.19)) induced by the polarization of the incident laser beams.

Again, let us start with the total cross section. The angular integration over the direction of the W in the $e\gamma$ center-of-mass frame is cut at $|\cos\theta| = 0.8$. We assume systematic errors in measuring the total cross section to be 5%. As in $e\gamma \to W\nu$, the total cross section depends on the photon spectrum used. The lowest cross section is obtained by using the Weizsacker-Williams distribution. In that case, the cross section is about $0.37R$ which corresponds to a little over 1000 events. The statistical error in that case is about 3%. With the Compton backscattered and the beamstrahlung spectra, however, the total cross section is 28 and 56 units of R respectively. The statistical errors are much less than 1% in both cases, and are

completely negligible. Figure 24 shows the total cross section for $\gamma\gamma \to W^+W^-$ as a function of κ for several values of λ. The calculations were performed using various photon spectra. Figure 25 shows its dependence on λ for several values of κ.

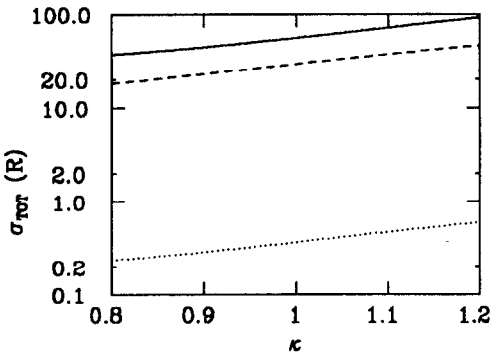

Figure 40. $\sigma_{\rm TOT}$ for $\gamma\gamma \to W^+W^-$ as a function of κ for $\lambda = 0$. Here and henceforth, the solid curves correspond to the Compton backscattered spectrum. The dashed curves are computed using the beamstrahlung spectrum. The dotted curves correspond the the Weizsacker-Williams distribution.

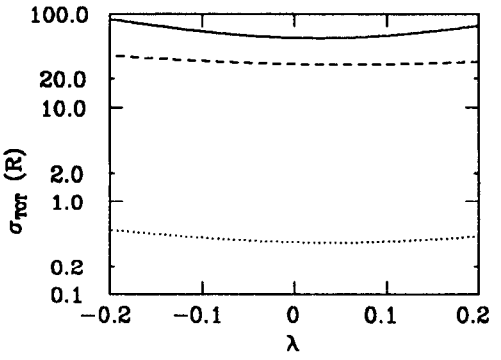

Figure 41. $\sigma_{\rm TOT}$ for $\gamma\gamma \to W^+W^-$ as a function of λ for $\kappa = 1$.

The process $\gamma\gamma \to W^+W^-$ is symmetric with respect to interchanging the two initial photons, so there cannot be any forward-backward asymmetry. The angular distribution of the W does, however, carry important information. We quantify this information by looking at the IO ratio as defined in eqn. (3.23). We assume that IO can be measured with systematic error of 0.03. Figures 42 and 43 show IO's dependence on κ and λ.

As in $e^+e^- \to W^+W^-$, one can extract the L/T ratio (eqn. (3.24)) from the angular distribution of the W decay products. Again, one has to reconstruct the missing neutrino momentum by imposing the constraint that the total momentum

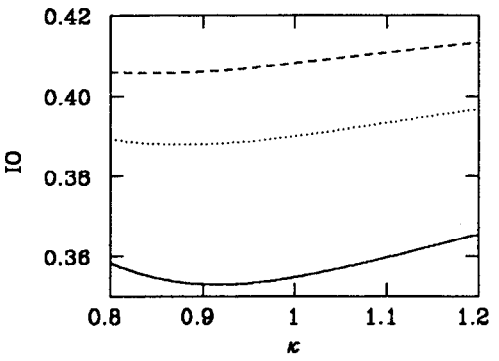

Figure 42. IO as a function of κ for $\lambda = 0$.

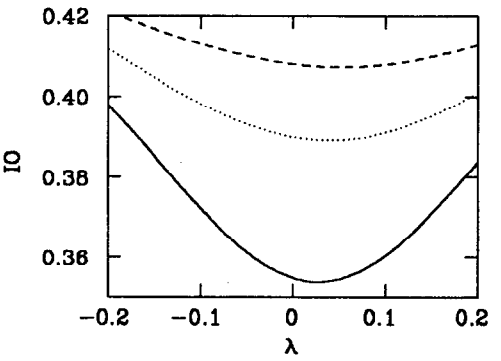

Figure 43. IO as a function of λ for $\kappa = 1$.

perpendicular to the beam direction is zero, and that the invariant mass of the neutrino-lepton system be that of the W. That fixes the neutrino momentum up to a twofold ambiguity. This ambiguity can be practically resolved by consistantly selecting the more probable solution. Monte Carlo studies done for the process $e^+e^- \to W^+W^-$ in an environment with hard beamstrahlung radiation.[37] These studies suggest that the degredation of data quality associated with the resolution of this ambiguity is minimal.

We assume that the L/T ratio can be measured with systematic error of 0.03. Figures 44 and 45 show its dependence on κ and λ.

In the case of a dedicated $\gamma\gamma$ collider constructed using the Compton backscattering mechanism, additional information can be extracted by looking at the dependence of the cross section on the polarization of the laser beams. We define the (0/2) ratio in analogue to (1/3) of eqn. (4.20) as the ratio between the '$J_z = 0$ dominated' and the '$|J_z| = 2$ dominated' configurations. The '$J_z = 0$ dominated' ('$|J_z| = 2$ dominated') configuration corresponds to having the *most energetic* photons of each beam have the same (opposite) helicity. We assume this ratio can be measured with systematic error of 0.01. Again, this measurement does not require the electron beams to be polarized. Figures 46 and 47 show its dependence on κ

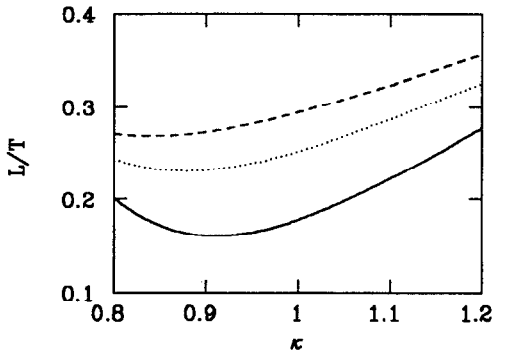

Figure 44. L/T as a function of κ for $\lambda = 0$.

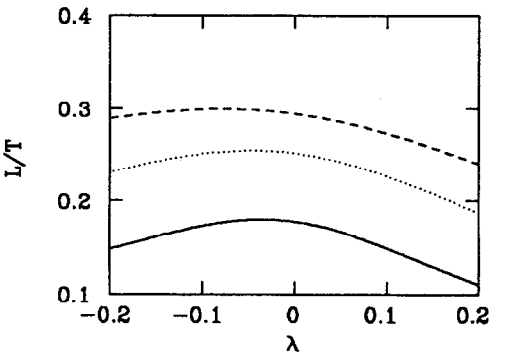

Figure 45. L/T as a function of λ for $\kappa = 1$.

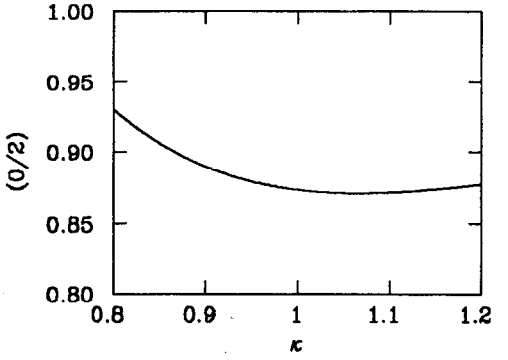

Figure 46. $(0/2)$ as a function of κ for $\lambda = 0$.

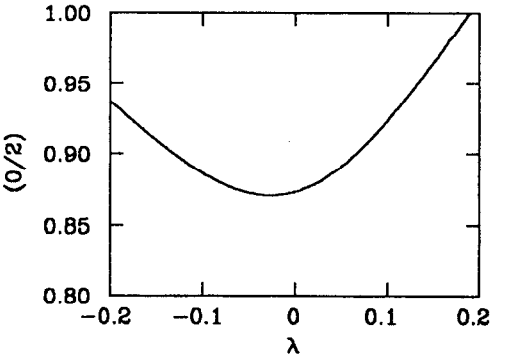

Figure 47. $(0/2)$ as a function of λ for $\kappa = 1$.

and λ.

Finally, with the photon beams polarized, one can measure not only the $|\cos\chi|$ distribution which carries information on the L/T ratio, but also the χ forward-backward asymmetry $\chi_{\rm FB}$ which carries information on the ratio between positively and negatively polarized W bosons (eqn. (5.7).) Here we assume that $\chi_{\rm FB}$ can be

measured with systematic error of 0.03. Figures 48 and 49 show its dependence on κ and λ.

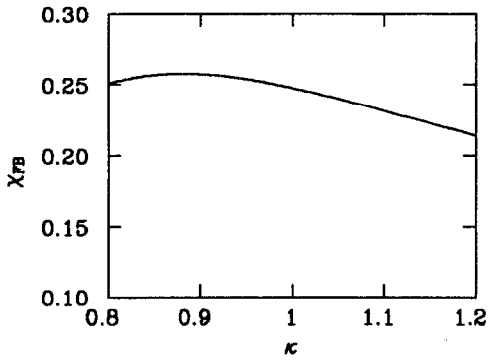

Figure 48. χ_{FB} as a function of κ for $\lambda = 0$.

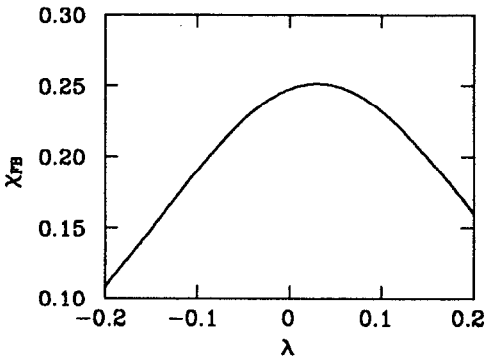

Figure 49. χ_{FB} as a function of λ for $\kappa = 1$.

5.5 Discovery limits

We repeat the analysis described in section 3.5 to the observables described in the previous section. Figures 50 and 51 show the (2σ) regions for each observable discussed in the previous section, as well as the 68% and 90% confidence level bounds. The calculations were repeated for each of the three photon spectra. Note that a dedicated photon collider provides for a much better measurement of λ.

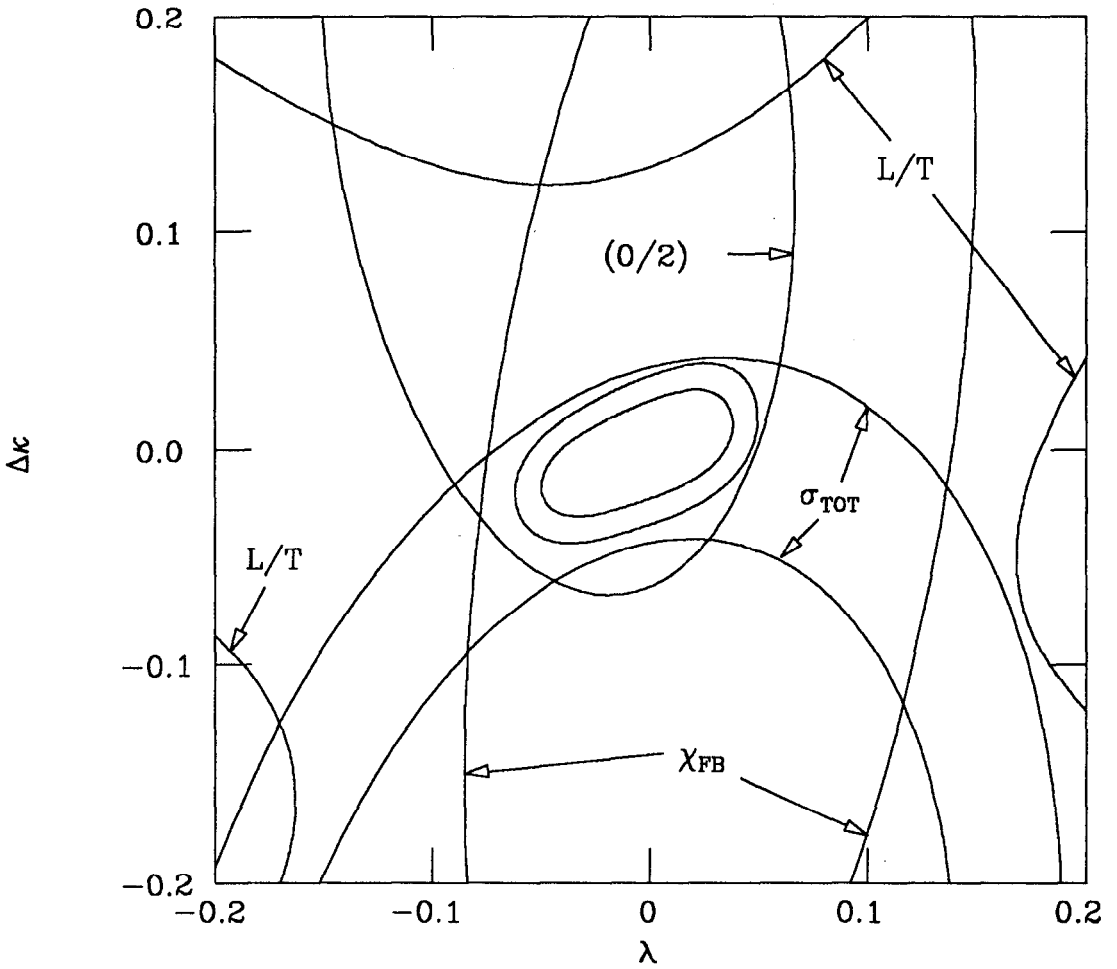

Figure 50. The (2σ) regions in the κ-λ plane from various measurements of $\gamma\gamma \to W^+W^-$: $\sigma_{\rm TOT}$, L/T, (0/2) and $\chi_{\rm FB}$. The center regions correspond to 68% and 90% confidence level bounds from the combination of all measurements. All calculations were done using the Compton backscattered spectrum.

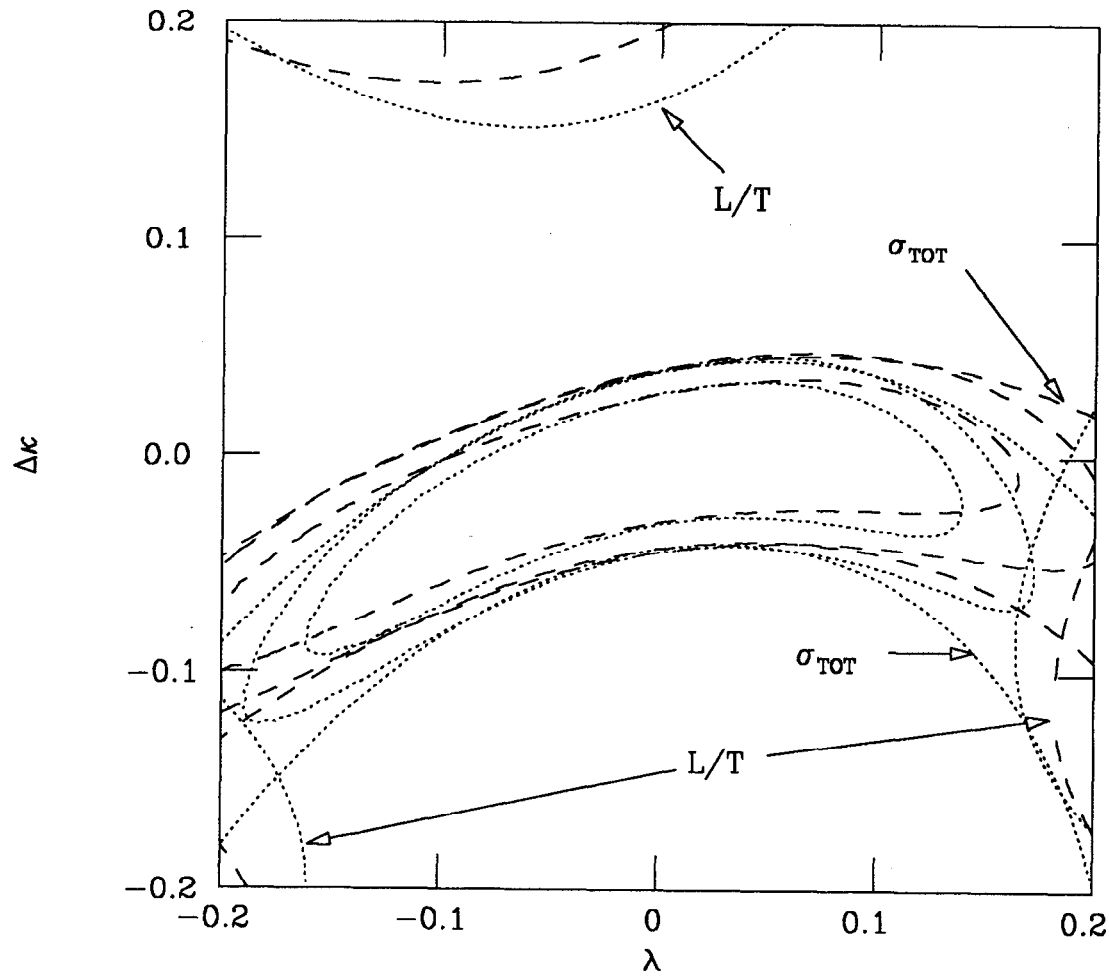

Figure 51. The (2σ) regions in the κ-λ plane from various measurements of $\gamma\gamma \to W^+W^-$ using the beamstrahlung (dashed) and the Weizsacker-Williams (dotted) spectra. The regions in the center correspond to 68% and 90% confidence level bounds from the combination of all measurements.

6. Summary and Conclusions

We summerize our results by displaying the allowed regions taken from figures 15, 32, 33, 50 and 51. Figures 52, 53 and 54 show the 90% confidence limits from the three processes using the Compton backscattering, beamstrahlung and Weizsacker-Williams spectra respectively. Note that the curve from $e^+e^- \rightarrow W^+W^-$ is the same in all three graphs, and does not include any photon radiation effects.

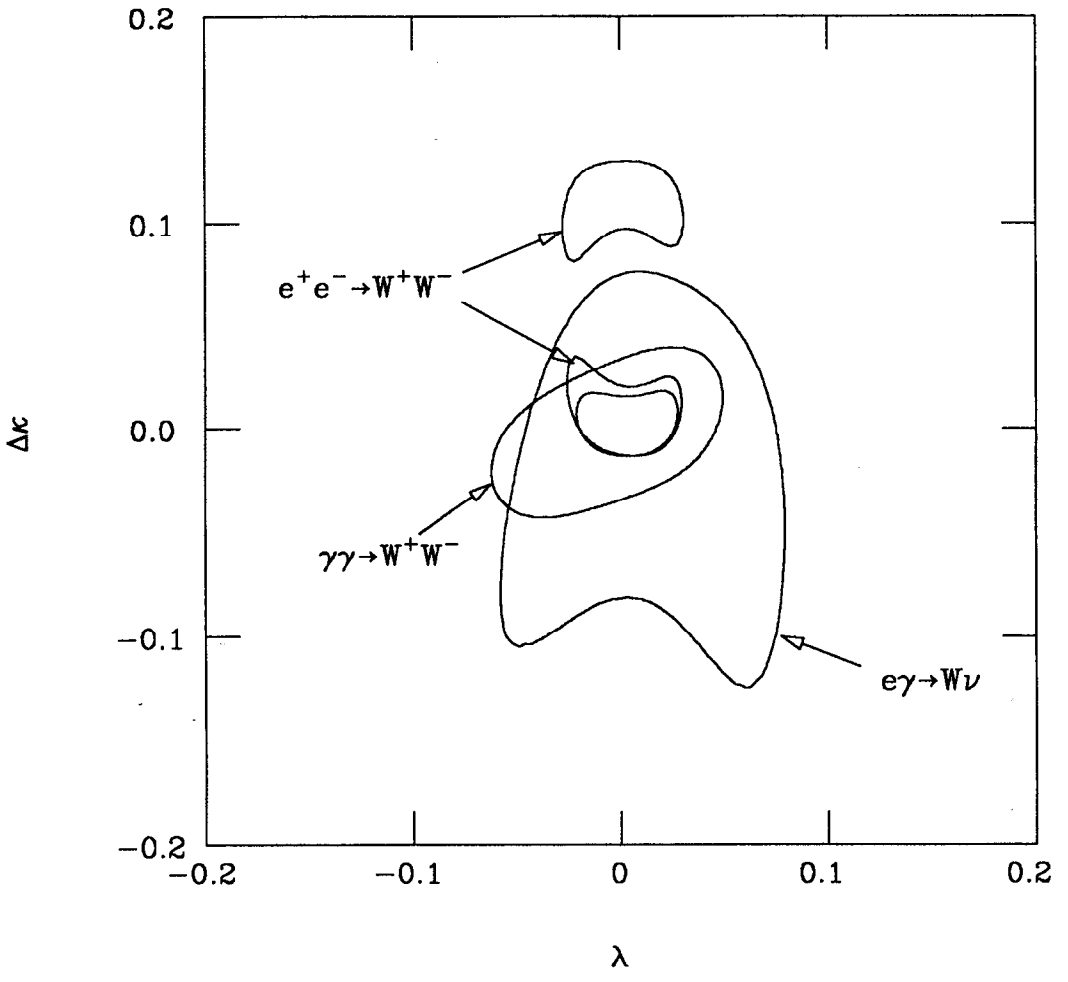

Figure 52. Allowed regions (90% confidence level) in the κ-λ plane from various processes and using the Compton backscattered spectrum. The center region is obtained by combining all three processes.

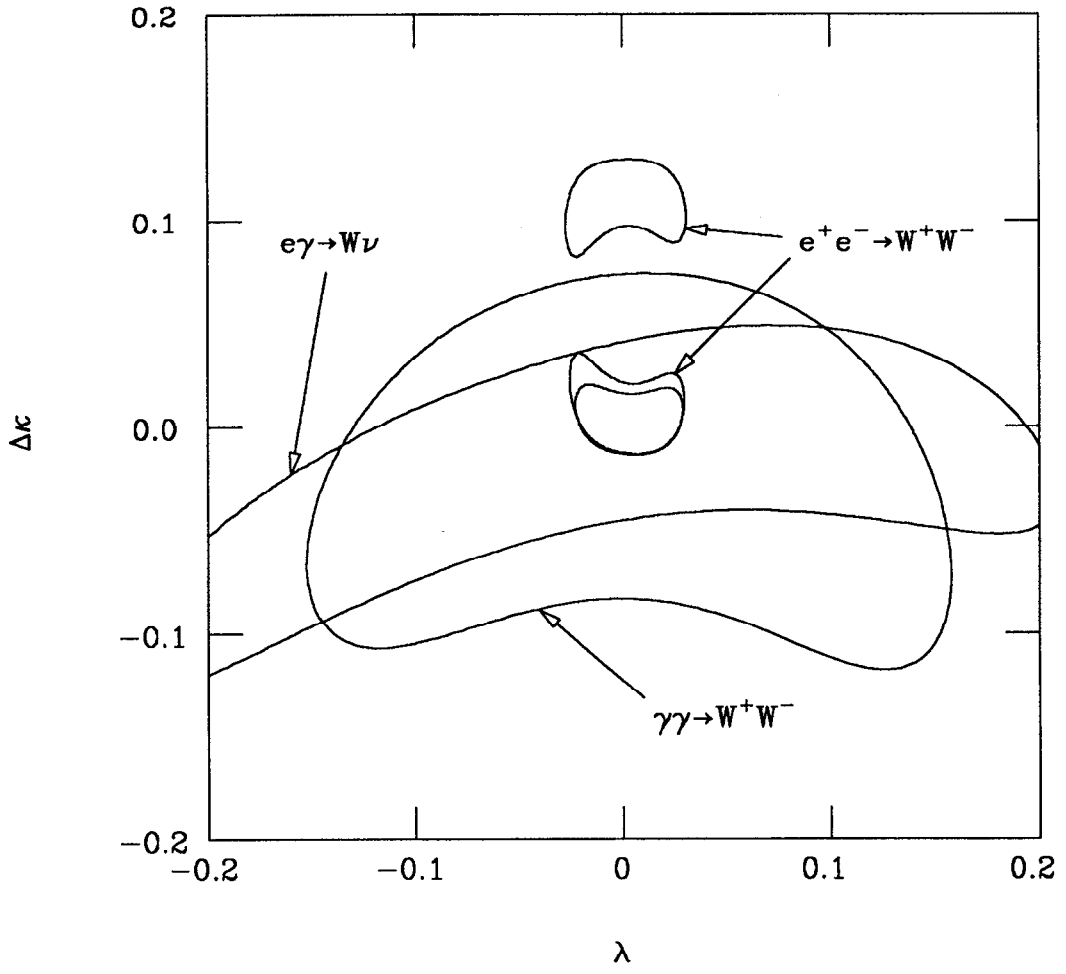

Figure 53. Allowed regions (90% confidence level) in the κ-λ plane from various processes and using the beamstrahlung spectrum. The center region is obtained by combining all three processes.

Finally, we show only the combined limits from all three processes and for the three photon spectra. The combined bounds are dominated by the $e^+e^- \to W^+W^-$ measurement which is common to all three spectra. The importance of the other processes is first in verifying the $e^+e^- \to W^+W^-$ results in a way which does not depend on the WZ couplings, and second in providing good statistics until the full $e^+e^- \to W^+W^-$ data set can be collected.

A 500 GeV e^+e^- collider is a powerful tool for measuring $W\gamma$ and WZ cou-

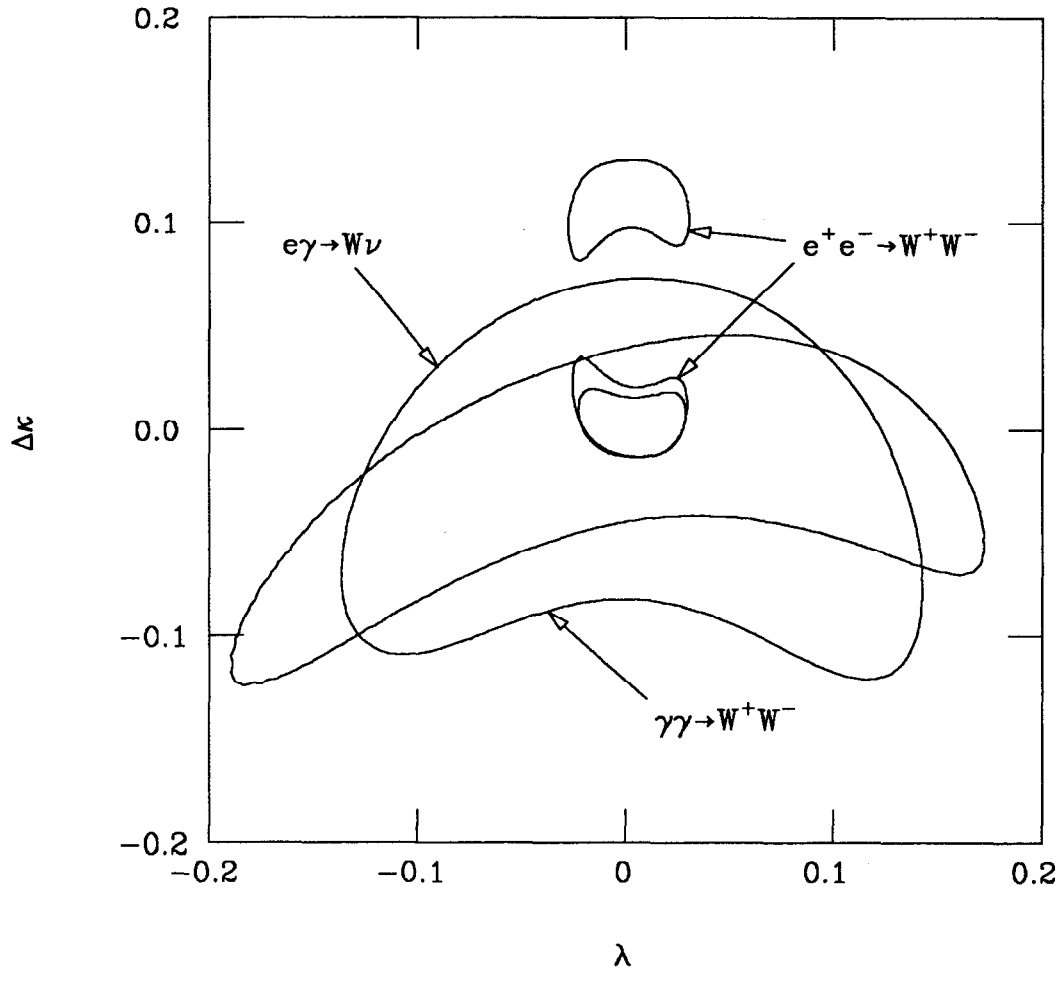

Figure 54. Allowed regions (90% confidence level) in the κ-λ plane from various processes and using the Weizsacker-Williams spectrum. The center region is obtained by combining all three processes.

plings. In this work we concentrated on measuring C and P conserving parameters in the $WW\gamma$ vertex. The process $e^+e^- \to W^+W^-$ is uniquely sensitive to the various couplings under examination. The two other processes we consider, $e\gamma \to W\nu$ and $\gamma\gamma \to W^+W^-$ can significantly add to our knowledge of W interactions. Compared to $e^+e^- \to W^+W^-$, both processes involve only $W\gamma$ vertices, allowing a separation of $W\gamma$ and WZ effects. Their large cross sections allow detailed study even with relatively small integrated luminosity. Useful information can be derived

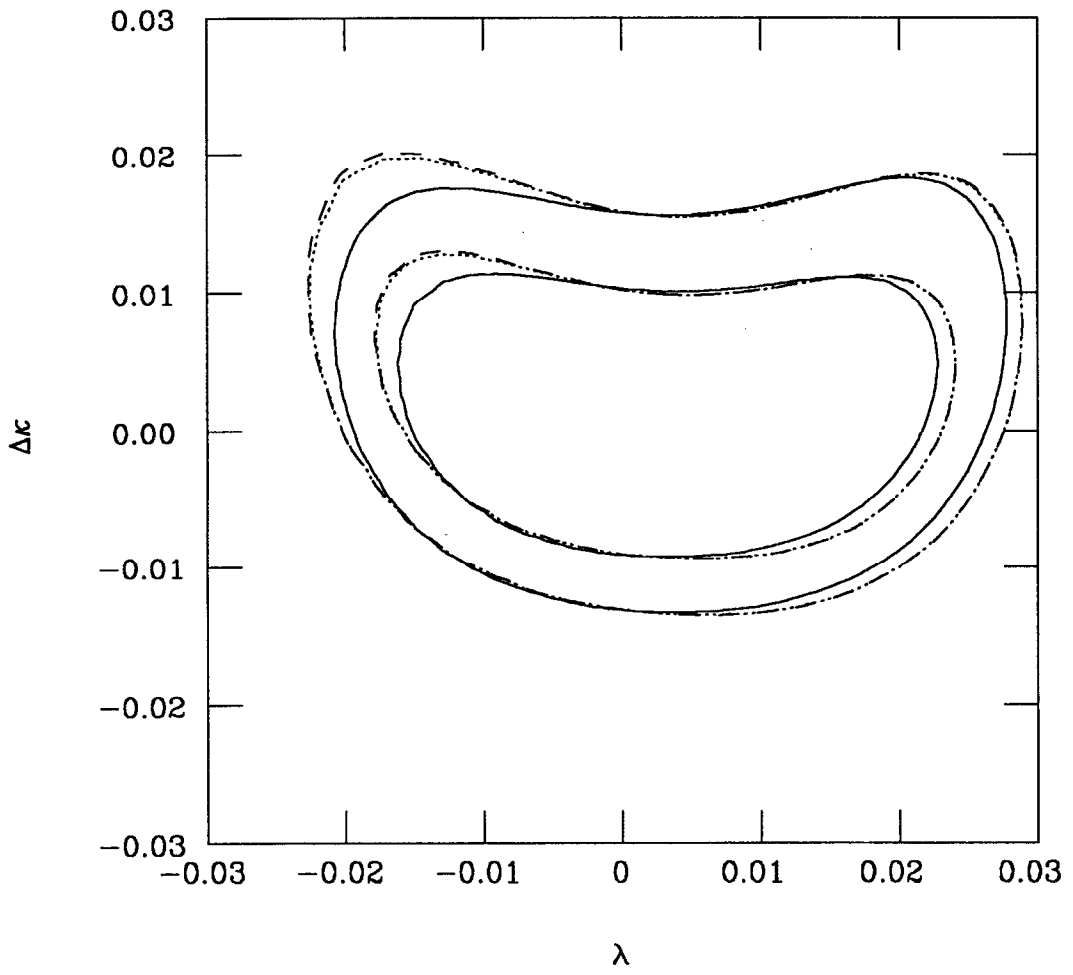

Figure 55. Allowed regions (68% and 90% confidence levels) in the κ-λ plane from the combination of all three processes and using the Compton backscattered (solid), beamstrahlung (dashed) and Weizsacker-Williams (dotted) spectra.

from these processes even in a traditional e^+e^- collider. Constructing a dedicated $e\gamma$ or $\gamma\gamma$ collider can greatly enhance the sensitivity of the two processes. Finally, $\gamma\gamma \to W^+W^-$ involves the $WW\gamma\gamma$ vertex. A careful analysis of experimental results should give us insight into its structure.

Appendix A. The Vector Equivalence Technique

In this appendix we discuss the 'Vector Equivalence' technique for symbolic, matrix element level spinor calculations. As its name implies, the heart of the technique is the calculation of a Lorentz four vector which serves as an equivalent to two external fermions. In further calculations, traces involving this vector replace the matrix element with the external fermions.

In calculating a Feynman diagram with external fermions, one encounters objects of the form

$$\mathcal{M} = \overline{u}(p,s)\Gamma u(p',s'), \tag{A.1}$$

where p and p' are the momenta of the external fermions, and s and s' are their helicities. Γ is an arbitrary string of Dirac gamma matrices. In this discussion we only refer to fermions. Anti-fermions can be treated with the same expressions provided one changes the sign of the particle mass.

The traditional method calls for squaring $\mathcal{M}$ while summing over fermion helicities:

$$\begin{aligned}\sum_{s,s'} |\mathcal{M}|^2 &= \sum_{s,s'} \mathrm{tr}\left\{\overline{u}(p',s')\overline{\Gamma}u(p,s)\overline{u}(p,s)\Gamma u(p',s')\right\} \\ &= \mathrm{tr}\left\{(\not{p}' - m')\overline{\Gamma}(\not{p} - m)\Gamma\right\},\end{aligned} \tag{A.2}$$

where $\overline{\Gamma} = \Gamma^{R*}$ and m and m' are the masses of p and p' respectively.

This method is advantageous in that the final result is expressed in terms of easy to calculate Lorentz invariants. The problem with this method is that the number of terms in the squared amplitude grows as the square of the number of terms in $\mathcal{M}$.

Several authors have proposed methods for calculating the matrix element without squaring.[40,41] We propose yet another such method. Its main advantage is that it allows, much like the traditional method, a relatively simple *symbolic* evaluation of $\mathcal{M}$. Unlike other methods, one is not required to sum over vector

polarizations for massive bosons or to use a real basis for them. Our method also allows calculation of quantities with free Lorentz indices.

We start by rewriting

$$\mathcal{M} = \overline{u}(p,s)\Gamma u(p',s') = \mathrm{tr}\left\{\Gamma u(p',s')\overline{u}(p,s)\right\}. \tag{A.3}$$

Next, decompose

$$u(p',s')\overline{u}(p,s) = \frac{1}{2}\sum_{\lambda}\left[\mathcal{U}_\lambda P_\lambda + \mathcal{V}_\lambda^\mu P_\lambda \gamma_\mu\right] + \frac{1}{4}\mathcal{W}^{\mu\nu}\gamma_{\mu\nu}, \tag{A.4}$$

where $P_\pm = (1 \pm \gamma^5)/2$ and $\gamma_{\mu\nu} = (\gamma_\mu\gamma_\nu - \gamma_\nu\gamma_\mu)/2$. $\mathcal{U}$, $\mathcal{V}$ and $\mathcal{W}$ all depend on p, s, p' and s'.

The coefficients $\mathcal{U}_\lambda$, $\mathcal{V}_\lambda^\mu$ and $\mathcal{W}^{\mu\nu}$ can be calculated using the projections

$$\begin{aligned}
\mathcal{U}_\lambda &= \mathrm{tr}\left\{u(p',s')\overline{u}(p,s)P_\lambda\right\} = \overline{u}(p,s)P_\lambda u(p',s'),\\
\mathcal{V}_\lambda^\mu &= \mathrm{tr}\left\{u(p',s')\overline{u}(p,s)\gamma^\mu P_\lambda\right\} = \overline{u}(p,s)\gamma^\mu P_\lambda u(p',s'),\\
\mathcal{W}^{\mu\nu} &= \mathrm{tr}\left\{u(p',s')\overline{u}(p,s)\frac{\gamma^{\mu\nu}}{2}\right\} = \frac{1}{2}\overline{u}(p,s)\gamma^{\mu\nu}u(p',s').
\end{aligned} \tag{A.5}$$

Given $\mathcal{U}_\lambda$, $\mathcal{V}_\lambda^\mu$ and $\mathcal{W}^{\mu\nu}$, $\mathcal{M}$ may be written as

$$\mathcal{M} = \overline{u}(p,s)\Gamma u(p',s') = \frac{1}{2}\sum_{\lambda}\left[\mathcal{U}_\lambda \mathrm{tr}\left\{\Gamma P_\lambda\right\} + \mathrm{tr}\left\{\Gamma P_\lambda \not{\mathcal{V}}_\lambda\right\}\right] + \frac{1}{4}\mathcal{W}^{\mu\nu}\mathrm{tr}\left\{\Gamma\gamma_{\mu\nu}\right\}. \tag{A.6}$$

At this point, one could proceed by substituting a specific representation for the spinors and Dirac matrices in eqn. (A.5). The general symbolic expressions for $\mathcal{U}_\lambda$, $\mathcal{V}_\lambda^\mu$ and $\mathcal{W}^{\mu\nu}$ are complicated, but managable. The calculation of $\mathcal{M}$ is reduced to an evaluation of traces. This can be done quickly and efficiently with one of several computer algebra systems.[42,43,44]

The expressions (A.5) and (A.6) simplify dramatically when only massless external fermions are involved, and no helicity flip occurs. The second condition is automatic if there are no virtual massive fermions. In high-energy calculations, often, the only massive fermion is the top quark. Diagrams in which the top quark decays by emitting a W also satisfy the helicity conservation condition because only left handed quarks couple to the W. Helicity conservation implies that Γ of eqn. (A.1) contains an odd number of gamma matrices. Consequently, both $\mathcal{U}_\lambda$ and $\mathcal{W}^{\mu\nu}$ vanish. Further, helicity conservation requires $s = s' = \lambda$. Equation (A.6) then takes the form

$$\overline{u}_\lambda(p)\Gamma u_\lambda(p') = \frac{1}{2}\mathrm{tr}\left\{\Gamma P_\lambda \not{\mathcal{V}}_\lambda\right\}, \tag{A.7}$$

and

$$\mathcal{V}^\mu_\lambda = \overline{u}_\lambda(p)\gamma^\mu u_\lambda(p'). \tag{A.8}$$

We substituted the notation $u_\lambda(p) = u_\lambda(p,\lambda)$. The vector $\mathcal{V}^\mu_\lambda$ obeys the following relations:

$$\begin{aligned} |\mathcal{V}_\lambda|^2 &= -4p\cdot p', \\ \mathcal{V}_\lambda\cdot p = \mathcal{V}_\lambda\cdot p' &= 0, \\ \mathcal{V}_\lambda\cdot\mathcal{V}^*_{-\lambda} = \mathcal{V}^2_\lambda &= 0, \end{aligned} \tag{A.9}$$

where we have used $\mathcal{V}^*_\lambda = \mathcal{V}_{-\lambda}$. We write $\mathcal{V}_\pm = R \pm iI$ with both R and I real. Then, assuming both p and p' are real, eqn. (A.9) takes the form

$$\begin{aligned} R^2 + I^2 &= -4p\cdot p', \\ R\cdot p = R\cdot p' &= 0, \qquad I\cdot p = I\cdot p' = 0, \\ R^2 - I^2 &= 0, \qquad R\cdot I = 0. \end{aligned} \tag{A.10}$$

If there are no identical external fermions in the problem, the phase of $\mathcal{V}_\lambda$ is irrelevant. In that case we can arbitrarily choose $\mathcal{V}^0_\lambda$ to be real. Writing $R =$

$(\mathbf{R}, R^0)$ and $I = (\mathbf{I}, 0)$, one easily concludes

$$\begin{aligned} \mathbf{I} \cdot \mathbf{p} &= \mathbf{I} \cdot \mathbf{p}' = 0, \\ \mathbf{R} \cdot \mathbf{p} &= \mathbf{R} \cdot \mathbf{p}' \\ \mathbf{R} \cdot \mathbf{I} &= 0. \end{aligned} \tag{A.11}$$

Geometrically, $\mathbf{I}$ is perpendicular to both $\mathbf{p}$ and $\mathbf{p}'$. $\mathbf{R}$ is perpendicular to $\mathbf{I}$ and thus lies on the $\mathbf{p}$-$\mathbf{p}'$ plane; on that plane it bisects the angle between $\mathbf{p}$ and $\mathbf{p}'$. If $\mathbf{p}$ and $\mathbf{p}'$ are collinear, there is an extra degree of freedom in selecting $\mathbf{R}$ and $\mathbf{I}$. That is because in that case, $\mathcal{V}^0_\lambda = 0$, and the arbitrary phase is not fixed by choosing it to be real.

With $p = E(\hat{n}, 1)$ and $p' = E'(\hat{n}', 1)$, the final expressions for $\mathcal{V}$ is:

$$\mathcal{V}_\pm = \sqrt{\frac{2EE'}{(1 + \cos\theta)}}(\hat{n} + \hat{n}' \mp i(\hat{n} \times \hat{n}'), 1 + \cos\theta). \tag{A.12}$$

Two special cases are $\hat{n} = \hat{n}'$ and $\hat{n} = -\hat{n}'$. The first case gives

$$\mathcal{V}_\pm = 2\sqrt{EE'}(\hat{n}, 1). \tag{A.13}$$

In the second case, choose $\hat{n}_1$ and $\hat{n}_2$ such that $\hat{n}_1 \times \hat{n}_2 = \hat{n}$. Then,

$$\mathcal{V}_\pm = 2\sqrt{EE'}(\hat{n}_1 \mp i\hat{n}_2, 0). \tag{A.14}$$

Detailed examples of the use of the Vector Equivalence techniques is given in sections 3.2 and 4.2. The value of $\mathcal{V}_\lambda$ for particular values of p and p' are given in eqns. (3.8) and (4.6). Special cases of eqn. (A.7) are given in eqns. (3.9) and (4.7).

Appendix B. HIP

B.1 Introduction

Present day pertubative calculations in the Standard Model (SM) and its extensions often require tedious algebra calculations. While tree level calculations of two-body production processes in the SM can certainly be done manually, it is often helpful to have a check in the form of an automatic calculation method. Processes involving the production of more than two particles (*e.g.* $e^+e^- \to W^+W^-\gamma$) or complicated Feynman rules (*e.g.* $\gamma\gamma \to W^+W^-$ with arbitrary $W\gamma$ couplings) involve much more difficult calculations in which computerized aid is almost indispensable.

Two approaches have been used to automate calculations of this type. Hagiwara *et al.*[45] have written a set of Fortran subroutines that calculate matrix elements numerically. This approach allows the automatic calculation of complicated tree level processes, but it is restricted to numeric results. An alternative approach introduced by Veltman[43] with *Schoonship* is to allow symbolic manipulation of expressions. While *Schoonship* was written as a special purpose program, with all the necessary algorithms 'hard-wired' into its assembly code, *Reduce*[42] followed a more general approach. Much more mathematical knowledge (*e.g.* integration rules) is incorporated into the program as higher-level lisp routines. The user, building on that basis of knowledge, can then expand the program by writing his or her own routines. The price for that flexibility is naturally paid in performance.

We follow this latter approach by writing our packages in *Mathematica*,[35] one of the newer and most promising of the new generation of symbolic manipulation languages which also includes *Maple*.[46] Using *Mathematica*'s high-level programming language greatly simplifies the task of writing programs. Additionally, the physics calculations are embedded within a powerful environment in which results can be simplified, calculated numerically and plotted. With the rapid advance in computer performance, the CPU-time needed for the calculations is usually negligible compared with the time needed to prepare the input and process the output

of the programs. This approach is also being used by the Würzburg group in their programs *FeynArts*[47] and *FeynCalc*.[48]

Unlike *Feyn Arts* we do not attempt to automatically generate the necessary Feynman diagrams. Typically, tree-level diagrams can be easily generated manually. HIP takes as input expressions describing the Feynman diagrams. HIP then provides the user with a rich set of operators by which to manipulate the physical objects occurring in these expressions. The user may, for example, substitute explicit four-vectors and particle polarizations, square the matrix elements to give traces that can then be evaluated or convert the expressions to spinor techniques.[49] As an aid in calculating cross-sections and decay widths, phase-space integrals can be automatically constructed and evaluated symbolically, numerically, or converted to a C or Fortran program.

The traditional method of Feynman diagram calculation involves squaring the matrix element symbolically. The number of terms involved increases like the square of the number of Feynman diagrams involved. In contrast, spinor techniques are methods for calculating Feynman diagrams numerically at the matrix element level. The number of terms involved is linear with the number of Feynman diagrams. Photon and fermion polarizations have to be summed explicitly. Spinor techniques are simplest when the fermions involved can be taken to be massless. They are most useful when a large number of Feynman diagrams is involved.

We have used HIP extensively, typically calculating processes with relatively simple topology ($2 \to 2$ and $2 \to 3$ tree-level cross-sections) but with complex Feynman rules.

The paper proceeds as follows. In the next section we give a brief overview of HIP. Some of the major objects and functions are mentioned. In sect. 3 we describe in more detail some of HIP's more important functions, presenting the mathematical relations they use and short examples of their application. In sect. 4 we give two complete examples: the calculation of the width for the muon decay $\mu^- \to \nu_\mu e^- \overline{\nu}_e$ with a finite electron mass, and a calculation of the matrix element

for $e_R^+ e_R^- \to Z \to t\bar{t} \to W^+W^- b\bar{b}$, including the W coupling to light fermions, which preserves all spin and angular correlations. In sect. 5 we summarize and give an outlook. The complete listing of HIP functions, with their usage messages (available as on-line documentation) is given in the appendix.

B.2 Overview

The packages in HIP contain functions that can manipulate various mathematical objects occurring in high-energy physics such as four-vectors, spinors and gamma matrices. Rather than follow one strict path from input to output, the packages allow the user to specify how a calculation proceeds (either interactively or in batch mode). A typical calculation might be to construct a matrix element, square it and sum over polarizations, construct the phase-space integral and evaluate this integral to give a symbolic expression for the total cross-section.

The most fundamental component of any high energy calculation is the manipulation of four-vectors. Basic objects such as the dot-product $(p \cdot q)$ (`DotProduct[p, q]`), the metric $g^{\mu\nu}$ (`G[mu, nu]`) and the completely anti-symmetric tensor $\epsilon^{\mu\nu\sigma\tau}$ (`Eps[mu, nu, sig, tau]`) are defined, with some of their elementary properties (*e.g.* the dot-product is symmetric in its two arguments). Four-vectors can be specified in terms of their components. They can then be boosted (using the function `Boost`), represented as sum of other four-vectors (`Decay`), etc. In addition, four-vectors can also be treated without reference to the explicit components. Dot products can be given explicit values (`SetDotProduct`, `SetMass`), Mandelstam variables defined (`SetMandelstam`), Lorentz indices defined (`PrepareIndex`) and contracted (`Contract`).

The second component in HIP is the Dirac algebra. The basic objects involved are the Dirac gamma matrices γ^μ (`DiracGamma[mu]`), γ^5 (`DiracGamma5`), the projection operators $P_\lambda = (1+\lambda\gamma^5)/2$ (`HelicityProjection[lambda]`) and $\not{p} = p_\mu\gamma^\mu$ (`Slash[p]`). The Dirac matrix product is represented by the *Mathematica* built-in function `NonCommutativeMultiply` (aliased to `**`). The trace of a product of Dirac gamma matrices is computed using the operator `GammaTrace`.

Some programs handling Dirac algebra, notably Reduce, can only deal with gamma matrices. HIP can also work with spinors. The basic spinor objects $u(p)$ and $v(p)$ (`SpinorU[p]` and `SpinorV[p]`) and their conjugates $\overline{u}(p)$ and $\overline{v}(p)$ (`SpinorUbar[p]` and `SpinorVbar[p]`) are defined. The function `AbsSquared` is used to square matrix element expressions which may include these spinors.

Expressions involving spinors do not have to be squared before they are calculated numerically. The HIP function `ConvertToST` converts a suitable expression involving spinors to an expression involving the elementary spinor products $s(p,k) = \overline{u}_R(p)u_L(k)$ and $t(p,k) = \overline{u}_L(p)u_R(k)$ (`SpinorS[p, k]` and `SpinorT[p, k]`) defined in reference 49. The expression produced can then be evaluated numerically by giving explicit values to the components of the four-vectors. Alternatively, it can be squared and converted back to an expression involving traces using the function `STToTraces`.

Given an expression for the matrix element squared associated with a process, the calculation of physical observables such as cross sections and decay widths involves integration over the phase space of the out-going particles. The functions `CrossSection` and `DecayWidth` set up the phase-space integral. The functions return a `PhaseSpaceIntegral` object that can then be evaluated either symbolically using `EvaluatePhaseSpaceIntegral` or numerically using `NEvaluatePhaseSpaceIntegral`. Alternatively, one can write a *Mathematica* program to convert such an object to a C or Fortran program for numeric evaluation. Such a conversion program would be highly specific, depending on the particular programming language, integration routine etc. We have used one such program in our work, but it is not included with HIP.

HIP includes some of the common Feynman rules of the Standard Model which are implemented using the functions `Vertex` and `Propagator`. Constants such as $\sin^2\theta_W$ (`Sin[ThetaW]^2`) and particle masses (*e.g.* `Mass[ZBoson]`) are usually kept as symbolic constants. However, HIP stores a table of their numerical values; these are substituted for the symbolic expression by the *Mathematica* function `N`.

B.3 HIP FUNCTIONS

Strictly speaking, *Mathematica* does not distinguish between data-structures, functions and procedures. In practice, however, the *Mathematica* objects defined in HIP can be divided into several broad categories. In all cases we try to follow the *Mathematica* convention of beginning each name with a capital letter. Further, as far as is practical we use full, descriptive English names rather than cryptic acronyms. Using *Mathematica* utilities, the user can choose his or her own cryptic abbreviations. The major categories are:

1. Objects such as gamma matrices or dot products. These are characterized by the property that they usually remain unevaluated.
2. Declarations and definitions. These do not typically return anything, but are rather invoked as part of the initialization process.
3. Operations such as contracting indices or taking traces. These typically take their input and convert it to an equivalent expression.

In this section we describe the most important members of each class.

Table 7 lists the major functions representing objects with their equivalent in ordinary physical notation.

The most useful declarative functions are:

— `PrepareIndex`: `PrepareIndex[mu, nu]` declares μ and ν and Lorentz indices.

— `SetMass`: `SetMass[p1, p2,..., m]` sets `p1`, `p2`,.. to be four-vectors with invariant mass `m`.*

— `SetMandelstam`: `SetMandelstam[{p1, p2, p3, p4}, {m1, m2, m3, m4},`

---

* Note that the p's are used in a dual mode, both as representing momenta and as representing particles. The mass m associated with p is the mass of the particle carrying the momentum p. For off-shell particles, $p^2 \neq m^2$ (`DotProduct[p, p] != Mass[p]^2`).

Table 1. HIP functions representing *objects*

HIP Function	Example	Physical Equivalent
{}	{px, py, pz, e}	The four-vector (p_x, p_y, p_z, E)
DotProduct	DotProduct[p, q]	$p \cdot q$
G	G[mu, nu]	$g^{\mu\nu}$
Eps	Eps[p, q, mu, nu]	$\epsilon_{\tau\sigma\mu\nu} p^\tau q^\sigma$
DiracGamma	DiracGamma[mu]	γ^μ
Slash	Slash[p]	$\not{p}$
DiracGamma5	DiracGamma5	γ^5
**	DiracGamma[mu]**Slash[p]	$\gamma_\mu \not{p}$
SpinorU	SpinorU[p, lambda]	$u_\lambda(p)$
SpinorUbar	SpinorUbar[p, lambda]	$\overline{u}_\lambda(p)$
HelicityProjection	HelicityProjection[Left]	$P_L = (1-\gamma^5)/2$
SpinorS	SpinorS[p, k]	$s(p,k) = \overline{u}_R(p) u_L(k)$
SpinorT	SpinorT[p, k]	$t(p,k) = \overline{u}_L(p) u_R(k)$

s, t, u] sets p1, p2, p3 and p4 to be on-shell with masses m1, m2, m3 and m4 respectively and sets the DotProducts of p1, p2, p3 and p4 in terms of the Mandelstam variables s, t and u and the masses:

$$(p_1 \cdot p_2) \to \frac{1}{2}(s - m_1^2 - m_2^2) \qquad (p_3 \cdot p_4) \to \frac{1}{2}(s - m_3^2 - m_4^2)$$
$$(p_1 \cdot p_3) \to \frac{1}{2}(-t + m_1^2 + m_3^2) \qquad (p_2 \cdot p_4) \to \frac{1}{2}(-t + m_2^2 + m_4^2)$$
$$(p_1 \cdot p_4) \to \frac{1}{2}(-u + m_1^2 + m_4^2) \qquad (p_2 \cdot p_3) \to \frac{1}{2}(-u + m_2^2 + m_3^2),$$

where m_i is the mass of the particle p_i.

Most of HIP's functionality is implemented as operator-type functions. The main ones are:

— **Boost**: `Boost[fv, rap, dir]` gives a four-vector obtained by boosting the four-vector `fv` by rapidity `rap` in the direction specified by `dir`. Example:

```
In[1]:= Boost[{0, 0, 0, m}, r, {cth, 0}]
```

Boost the four-vector $(0, 0, 0, m)$ by rapidity r in the direction $\cos\theta = \text{cth}$, $\phi = 0$.

```
Out[1]= {Sqrt[1 - cth^2] m Sinh[r], 0, cth m Sinh[r], m Cosh[r]}
```

$$(m\sqrt{1-\cos^2\theta}\sinh r,\ 0,\ m\cos\theta\sinh r,\ m\cosh r).$$

— **Decay**: `Decay[v, dir, {m1, m2}]` gives two four-vectors v_1 and v_2 such that $v_1 + v_2 = v$, $v_1^2 = m_1^2$, $v_2^2 = m_2^2$ and the direction of v_1 in the v center-of-mass frame is given by `dir`. Example:

```
In[1]:= Decay[{0, 0, 0, m}, {cth, 0}, {m1, 0}]
```

Decompose the four-vector $p = (0, 0, 0, m)$ into two four-vectors p_1 and p_2 such that $p_1^2 = m_1^2$, $p_2^2 = 0$ and the direction of p_1 in the p center-of-mass frame is given by $\cos\theta = \text{cth}$ and $\phi = 0$. After some rearrangement one gets:

```
                  2    2    2                  2    2    2    2
        Sqrt[1 - cth ] (m  - m1 )      cth (m  - m1 )  m  + m1
Out[1]= {{-------------------------, 0, --------------, --------},
                    2 m                      2 m          2 m

                   2    2    2                  2    2    2    2
      -(Sqrt[1 - cth ] (m  - m1 ))     -(cth (m  - m1 ))  m  - m1
>     {---------------------------, 0, ----------------, --------}}
                    2 m                      2 m          2 m
```

$$p_1 = \left(\frac{\sqrt{1-\cos^2\theta}(m^2-m_1^2)}{2m}, 0, \frac{\cos\theta(m^2-m_1^2)}{2m}, \frac{m^2+m_1^2}{2m} \right),$$
$$p_2 = \left(\frac{-\sqrt{1-\cos^2\theta}(m^2-m_1^2)}{2m}, 0, \frac{-\cos\theta(m^2-m_1^2)}{2m}, \frac{m^2-m_1^2}{2m} \right).$$

— `Contract`: `Contract[expr, index]` contracts `index` in `expr`. `Contract` with respect to a particular index μ invokes a large set of rules. The basic rules for handling arbitrary tensors and vector are:

$$\begin{aligned} g_\mu^\mu &\to D \\ p_\mu q^\mu &\to p \cdot q \\ g_\mu^\tau T^{\nu_1 \cdots \mu \cdots \nu_n} &\to T^{\nu_1 \ldots \tau \ldots \nu_n} \end{aligned} \tag{B.1}$$

where D is the dimension of space-time.* For handling the completely anti-symmetric ϵ symbol we use

$$\epsilon_{\mu\nu_1\cdots\nu_n}\epsilon^{\mu\tau_1\cdots\tau_n} \to (D-n)\begin{vmatrix} g_{\nu_1}^{\tau_1} & \cdots & g_{\nu_1}^{\tau_n} \\ \vdots & \ddots & \vdots \\ g_{\nu_n}^{\tau_1} & \cdots & g_{\nu_n}^{\tau_n} \end{vmatrix}. \tag{B.2}$$

The rules associated with γ-matrices are:[50]

$$\begin{aligned} p_\mu \gamma^\mu &\to \not{p} \\ \gamma_\mu \gamma^\mu &\to D \\ \gamma_\mu \gamma_\nu \gamma^\mu &\to (2-D)\gamma_\nu \\ \gamma_\mu \gamma_{\nu_1} \gamma_{\nu_2} \gamma^\mu &\to (D-4)\gamma_{\nu_1}\gamma_{\nu_2} + 4g_{\nu_1\nu_2} \\ \gamma_\mu \gamma_{\nu_1} \gamma_{\nu_2} \gamma_{\nu_3} \gamma^\mu &\to -2\gamma_{\nu_3}\gamma_{\nu_2}\gamma_{\nu_1} - (D-4)\gamma_{\nu_1}\gamma_{\nu_2}\gamma_{\nu_3}. \end{aligned} \tag{B.3}$$

* Most of HIP's functions operate well in arbitrary D dimensions. The exceptions are the functions dealing with vectors given in terms of their explicit components (*e.g.* `Boost`), functions associated with phase-space integrals and functions treating γ^5.

For more complicated cases we use

$$\gamma_\mu \Gamma^{(n)} \gamma^\mu \to \begin{cases} 2\Gamma^{(n)} + 2\Gamma_R^{(n)} & (n \text{ even}) \\ -2\Gamma_R^{(n)} & (n \text{ odd}) \end{cases} \quad (D = 4)$$

$$(-1)^n \left((D-4)\Gamma^{(n)} + 2\Gamma_R^{(n)} - 2\sum_{i=4}^{n-3} (-1)^i \gamma_{\nu_i} \Gamma_i^{(n)} \right) \quad (D \neq 4), \tag{B.4}$$

where

$$\begin{aligned} \Gamma^{(n)} &= \gamma_{\nu_1} \cdots \gamma_{\nu_n} \\ \Gamma_R^{(n)} &= \gamma_{\nu_n} \cdots \gamma_{\nu_1} \\ \Gamma_i^{(n)} &= \gamma_{\nu_1} \cdots \gamma_{\nu_{i-1}} \gamma_{\nu_{i+1}} \cdots \gamma_{\nu_n}. \end{aligned} \tag{B.5}$$

Example:

```
In[1]:= Contract[G[mu, nu] p[mu], mu]
```

Contract the index μ in $g_{\mu\nu} p^\mu$.

```
Out[1]= p[nu]
```

$$p_\nu$$

```
In[2]:= Contract[DiracGamma[mu]**Slash[p]**DiracGamma[nu]**
        DiracGamma[mu], mu]
```

$$\gamma_\mu \not{p} \gamma_\nu \gamma^\mu$$

```
Out[2]= (-4 + SpaceTimeDimension) Slash[p] ** DiracGamma[nu] +
>     4 p[nu]
```

$(D-4) \not{p} \gamma_\nu + 4 p_\nu$ where D is the space-time dimension.

— `GammaTrace`: `GammaTrace[expr]` is the trace (in spinor space) of `expr`. tr $\{1\}$ can be left unevaluated as the constant `DiracGammaSize`, but is usually set

to 4. Whenever possible, GammaTrace uses the following simple rules:

$$\begin{aligned}
\mathrm{tr}\left\{\gamma_{\mu_1}\cdots\gamma_{\mu_{2n+1}}\right\} &\to 0 & \mathrm{tr}\left\{\gamma^5\right\} &\to 0\\
\mathrm{tr}\left\{\gamma^5\gamma_\mu\gamma_\nu\right\} &\to 0 & \mathrm{tr}\left\{\gamma^5\gamma_{\mu_1}\cdots\gamma_{\mu_{2n+1}}\right\} &\to 0\\
\mathrm{tr}\left\{\gamma_\mu\gamma_\nu\right\} &\to \mathrm{tr}\left\{1\right\} g_{\mu\nu} & \mathrm{tr}\left\{\gamma^5\gamma_\mu\gamma_\nu\gamma_\tau\gamma_\sigma\right\} &\to \mathrm{tr}\left\{1\right\} i\epsilon_{\mu\nu\tau\sigma}.\\
\mathrm{tr}\left\{\gamma_\mu\gamma_\nu\gamma_\tau\gamma_\sigma\right\} &\to \mathrm{tr}\left\{1\right\}\left(g_{\mu\nu}g_{\tau\sigma}+g_{\mu\sigma}g_{\nu\tau}-g_{\mu\tau}g_{\nu\sigma}\right)
\end{aligned} \tag{B.6}$$

Traces of longer expressions invoke the following recursive rules:

$$\begin{aligned}
\mathrm{tr}\left\{\gamma_\mu\Gamma^{(n)}\right\} &\to \sum_{i=1}^{n}(-1)^{(i+1)}g_{\mu\nu_i}\mathrm{tr}\left\{\Gamma_i^{(n)}\right\}\\
\mathrm{tr}\left\{\gamma^5\Gamma^{(n)}\right\} &\to \sum_{1\le i<j<k<l\le n}(-1)^{(i+j+k+l)}i\epsilon_{\nu_i\nu_j\nu_k\nu_l}\mathrm{tr}\left\{\Gamma_{ijkl}^{(n)}\right\}.
\end{aligned} \tag{B.7}$$

Example:

```
In[1]:= GammaTrace[DiracGamma[mu]**DiracGamma[nu]
```

$$\mathrm{tr}\left\{\gamma_\mu\gamma_\nu\right\}$$

```
Out[1]= 4 G[mu, nu]
```

$$4g_{\mu\nu}$$

```
In[2]:= GammaTrace[DiracGamma5**DiracGamma[mu]**DiracGamma[nu]**
        DiracGamma[sig]**DiracGamma[tau]]
```

$$\mathrm{tr}\left\{\gamma^5\gamma_\mu\gamma_\nu\gamma_\sigma\gamma_\tau\right\}$$

```
Out[2]= 4 I Eps[mu, nu, sig, tau]
```

$$4i\epsilon_{\mu\nu\sigma\tau}$$

```
In[3]:= GammaTrace[DiracGamma[mu]**Slash[p1]**DiracGamma[nu]**
        Slash[p2]**DiracGamma[mu]**Slash[p3]**DiracGamma[nu]**
        Slash[p4]]
```

$$\mathrm{tr}\left\{\gamma_\mu\ \not{p}_1\gamma_\nu\ \not{p}_2\gamma^\mu\ \not{p}_3\gamma^\nu\ \not{p}_4\right\}$$

```
Out[3]= -32 DotProduct[p1, p3] DotProduct[p2, p4]
```

$$-32(p_1 \cdot p_3)(p_2 \cdot p_4)$$

— **AbsSquared**: **AbsSquared[expr]** is the absolute value of **expr** squared. **AbsSquared** sums over polarization of both external spinors and vectors unless their polarizations are explicitly specified:

$$\begin{aligned} |Xu(p)|^2 &\to \sum_\lambda Xu_\lambda(p)\overline{u}_\lambda(p)X^* \to X(\not{p}+m)X^* \\ |Xv(p)|^2 &\to \sum_\lambda Xv_\lambda(p)\overline{v}_\lambda(p)X^* \to X(\not{p}-m)X^* \\ |\epsilon_\mu(p)|^2 &\to \begin{cases} -g_{\mu\mu'} & (m=0) \\ -g_{\mu\mu'}+\dfrac{p_\mu p_{\mu'}}{m^2} & (m\neq 0), \end{cases} \end{aligned} \tag{B.8}$$

where m is the mass associated with p. Example:

```
In[1]:= AbsSquared[SpinorUbar[p]**SpinorV[q]]
```

$$|\overline{u}(p)v(q)|^2$$

```
Out[1]= 4 DotProduct[p,q] - 4 Mass[p] Mass[q]
```

$$4p \cdot q - 4m_p m_q$$

```
In[2]:= AbsSquared[SpinorUbar[p, Right]**SpinorV[q, Left]]
```

$$|\overline{u}_R(p)v_L(q)|^2$$

```
Out[2]= 2 DotProduct[p,q]
```

$$2p \cdot q$$

```
In[3]:= AbsSquared[SpinorUbar[p]**DiracGamma[mu]**SpinorU[q]]
```

$$|\overline{u}(p)\gamma_\mu u(q)|^2$$

```
Out[3]= -4 DotProduct[p, q] G[mu, Conjugate[mu]] +
>     4 G[mu, Conjugate[mu]] Mass[p] Mass[q] +
>     4 p[Conjugate[mu]] q[mu] + 4 p[mu] q[Conjugate[mu]]
```

$$-4(p\cdot q)g_{\mu\mu'} + 4g_{\mu\mu'}m_p m_q + 4p_{\mu'}q_\mu + 4p_\mu q_{\mu'}$$

`Conjugate[mu]` (μ' is the new index needed on squaring the expression).

— `ConvertToST`: `ConvertToST[expr]` attempts to convert `expr` to SpinorS and SpinorT objects. Unless instructed otherwise, the program assumes every massive vector `q` is the sum of two massless vectors `LightlikeVectorDecayedFrom[q, 1]` and `LightlikeVectorDecayedFrom[q, 2]`. Example:

```
In[1]:= ConvertToST[
          SpinorUbar[p, Right]**Slash[q]**SpinorU[k, Right]]
```

Convert $\overline{u}_R(p)\,\not{q}\,u_R(k)$ to spinor techniques. p and k have previously been set massless.

```
Out[1]= -(SpinorS[p, LightlikeVectorDecayedFrom[q, 1]] *
>         SpinorT[k, LightlikeVectorDecayedFrom[q, 1]]) -
>     SpinorS[p, LightlikeVectorDecayedFrom[q, 2]] *
>      SpinorT[k, LightlikeVectorDecayedFrom[q, 2]]
```

The result is $s(p, q_1)t(k, q_1) - s(p, q_2)t(k, q_2)$ where $q_1^2 = q_2^2 = 0$ and $q_1 + q_2 = q$ are assumed.

— `Vertex`: `Vertex[line1, line2, ...]` is the Feynman rule for a vertex. Each line is of the form `particle` or `{particle, p}` or `{particle, p,`

indices} where particle is the particle type, p is the particle's momentum, and indexes are the appropriate Lorentz or gauge group indexes. Example:

```
In[1]:= Vertex[Electron, Electron, {ZBoson, p, mu}]
```

The eeZ vertex for Z boson carrying momentum p_μ

```
Out[1]= (-2 I Sqrt[Alpha] Sqrt[Pi] DiracGamma[mu] **
          -HelicityProjection[Left]                2
>        (------------------------- + Sin[ThetaW] )) /
                     2
>     (Cos[ThetaW] Sin[ThetaW])
```

$$\frac{-2i\sqrt{\alpha}\sqrt{\pi}}{\cos\theta_W \sin\theta_W}\gamma_\mu\left(-\frac{1}{2}P_L + \sin^2\theta_W\right)$$

where α is the electromagnetic fine structure constant and θ_W is the Weinberg angle.

— CrossSection and DecayWidth: CrossSection[me2, q1->{q1x, q1y, q1z, e1}, q2->{q2x, q2y, q2z, e2}, outGoing] returns an expression for the phase space integral to be evaluated by EvaluatePhaseSpaceIntegral. me2 is the expression for the matrix element squared, {p1x, p1y, p1z, e1} and {p2x, p2y, p2z, e2} are the explicit four-vectors of the incoming particles, and outGoing specifies the order of phase-space evaluation as explained below. DecayWidth[me2, p -> {px, py, pz, e}, outGoing] similarly returns an expression for the phase space integral resulting in the decay width given matrix element squared me2 and initial momentum {px, py, pz, e}.

The formula used for cross-section calculations is

$$\sigma = \frac{(2\pi)^4}{2s}\frac{2|q_1|}{\sqrt{s}}\int |\mathcal{M}|^2 d\Phi_n(q_1+q_2; p_1,\ldots,p_n), \qquad \text{(B.9)}$$

and for the decay width it is

$$\Gamma = \frac{(2\pi)^4}{2M} \int |\mathcal{M}|^2 \, d\Phi_n(P; p_1, \ldots p_n). \tag{B.10}$$

Phase-space integration is performed by a recursive use of the relations

$$\begin{aligned} d\Phi_n(P;\, p_1, \ldots, p_n) &= d\Phi_{n-1}\,(P;\, p_{12}, p_3, \ldots, p_n)\, d\Phi_2(p_{12}; p_1, p_2)\, (2\pi)^3 dm_{12}^2 \\ &= d\Phi_{n-1}(P;\, p_{12}, p_3, \ldots, p_n)\, \frac{1}{8(2\pi)^3} \frac{2|p_1|}{m_{12}}\, d\Omega_{12}\, dm_{12}^2, \end{aligned} \tag{B.11}$$

where $p_{12}^2 = m_{12}^2$ and Ω_{12} represents the direction of the 'decay' of the vector p_{12} to p_1 and p_2 in its center-of-mass frame. The factor $2|p_1|/m_{12}$ is given by

$$\frac{2|p_1|}{m_{12}} = \begin{cases} \dfrac{\left[(m_{12}^2 - (m_1+m_2)^2)\,(m_{12}^2 - (m_1-m_2)^2)\right]^{1/2}}{m_{12}^2} & \\ \sqrt{1 - \dfrac{4m_1}{m_{12}}} & (m_1 = m_2) \\ 1 - \dfrac{m_1^2}{m_{12}^2} & (m_2 = 0) \\ 1 & (m_1 = m_2 = 0). \end{cases} \tag{B.12}$$

The argument `outGoing` tells HIP how to build the phase space element $d\Phi_n$. It specifies both the order that the momenta $p_1 \cdots p_n$ are paired (eq. (B.11)) and, optionally, the symmetry of the individual two-body phase-space elements. By default, the complete angular integral over Ω_{12} is constructed. Often, due to the symmetry of the process, one can reduce the dimension of this integral (in the case of cylindrical symmetry), or eliminate it completely (in the case of spherical symmetry). This is done using the keywords `Cylindrical` and `Spherical`.

For example, let us consider the decay process $\mu^-(p) \to e^-(p_1)\overline{\nu}_e(p_2)\nu_\mu(p_3)$. If the μ is unpolarized, the decay process is spherically symmetric. The direction of ν_μ may be chosen arbitrarily. Once that is done, the direction of the electron with

respect to the $(e^-\overline{\nu}_e)$ system has cylindrical symmetry about the ν_μ direction. The `outGoing` argument is given by `Spherical[Cylindrical[p1, p2], p3]`. If the μ is polarized, the spherical symmetry of the decay is reduced to a cylindrical symmetry about the polarization axis. `outGoing` is then given by `Cylindrical[{p1, p2}, p3]`.

B.4 Example

In this section we give an example showing step by step how a HIP calculation is carried out. We compute the decay width of a muon in the process $\mu^-(p_\mu) \to e^-(p_e)\nu_\mu(p_\nu)\overline{\nu}_e(p_{\overline{\nu}})$ and with a non-zero electron mass. We use a low-energy approximation in which the W-propagator is a constant and is absorbed, along with the coupling constant g into the Fermi constant G_F.

```
In[1]:= PrepareIndex[sig]
```

Instruct *Mathematica* to treat `sig` as an index.

```
In[2]:= SetMass[{pnub, 0}, {pe, me}, {pnu, 0}, {pmu, mmu}]
```

Set the masses of the four external particles. The neutrinos (ν_μ and $\overline{\nu}_e$ carrying momenta `pnu` and `pnub` respectively) have zero mass. The electron (`pe`) is set to have mass `me` while the muon (`pmu`) is set to have mass `mmu`. Later on, these masses can be given numerical values.

```
In[3]:= matrixelement = 2 Sqrt[2] FermiGF *
        SpinorUbar[pnu] ** DiracGamma[sig] ** SpinorU[pmu, Left] *
        SpinorUbar[pe] ** DiracGamma[sig] ** SpinorV[pnub, Left];
```

$$\mathcal{M} = 2\sqrt{2}G_F\overline{u}(p_\nu)\gamma_\sigma u_L(p_\mu)\overline{u}(p_e)\gamma^\sigma u_L(p_{\overline{\nu}})$$

```
In[4]:= me2 = AbsSquared[matrixelement]/2;
```

Square the matrix-element using the *Mathematica* function `AbsSquared`. We suppress the printing of the long intermediate result.

```
In[5]:= me2 = Contract[me2, {sig, Conjugate[sig]}] // Factor
```

Contract over the indices σ and σ'. `// Factor` instructs *Mathematica* to the factor the expression.

```
Out[5]= 128 FermiGF^2 DotProduct[pe, pnu] DotProduct[pmu, pnub]
```

$$128 G_F^2 (p_e \cdot p_\nu)(p_\mu \cdot p_{\overline{\nu}})$$

```
In[6]:= width = DecayWidth[me2, pmu -> {0, 0, 0, mmu},
        Spherical[Cylindrical[pe, pnub], pnu]]
```

Ask *Mathematica* to construct the phase-space integral to compute the decay-width. The expression `Spherical[Cylindrical[pe, pnub], pnu]` indicates a cylindrical symmetry in the phase-space integral over the pair $(e^-, \overline{\nu}_e)$ and a spherical symmetry over pair $(\nu_\mu, (e^-, \overline{\nu}_e))$ (here $(e^-, \overline{\nu}_e)$ is the combined system of e^- and $\overline{\nu}_e$.)

```
Out[7]= -PhaseSpaceIntegral-
In[8]:= width = EvaluatePhaseSpaceIntegral[width];
```

Evaluate the phase-space integral symbolically. Again we suppress the long intermediate result.

```
In[9]:= Factor[width /. me->x mmu /. Log[a_ b_] :> Log[a]+Log[b]]
```

Use some *Mathematica* rules to tidy up the expression. We express the mass of the electron in terms of the mass of the muon $m_e = x m_\mu$ and combine logarithms using the rule $\log(ab) \to \log a + \log b$.

```
                 2    5                2      6    8        4      2
        -(FermiGF  mmu  (-1 + 8 x  - 8 x  + x  + x  + 12 x  Log[x ]))
Out[10]= ------------------------------------------------------------
                                    3
                              192 Pi
```

$$\Gamma(\mu^- \to e^- \nu_\mu \overline{\nu}_e) = \frac{G_F^2 m_\mu^5 (1 - 8x^2 + 8x^6 - x^8 - 12x^4 \log(x^2))}{192\pi^3}$$

B.5 Conclusion and Outlook

We developed HIP as an aid in the calculation tree-level processes in high energy physics which would otherwise be much more difficult. HIP's main feature is in providing an environment within *Mathematica* in which one can refer to objects and perform operations that occur frequently in this field. One can use HIP interactively to assist with small calculations, or set it up to automatically perform massive 'symbol crunching'.

We have checked HIP against hand calculations of $e^+e^- \to W^+W^-$, $e\gamma \to W\nu$, both with arbitrary (C and P conserving) $W\gamma$ couplings, and of numerous simple electroweak processes. We also checked them against published results for $e^+e^- \to W^+W^-\gamma$, $e^+e^- \to W^+W^-Z$, $e^+e^- \to \gamma\gamma\gamma$ and $e^+e^- \to ZZZ$.

In the future, we hope to extend HIP's capabilities into performing loop integrals, calculating color factors and incorporating other techniques for symbolically calculating Feynman diagrams at the matrix element level. We also hope to translate HIP to other symbolic languages such as *Maple*, so as to maximize the group of its potential users.

HIP is available for distribution. The distribution includes the various component *Mathematica* packages, the online documentation as listed in the appendix, and several files containing sample calculations done by HIP.

REFERENCES

1. M. A. Samuel, *et al.*, *Phys. Rev. Lett.* **67**(1991), 9.
2. K. Hagiwara, R. D. Peccei, D. Zeppenfeld and K. Hikasa, *Nucl. Phys.* **B282**(1987), 253 and references therein.
3. C. Ahn *et al.*, *Nucl. Phys.* **B309**(1988), 221.
4. G.L. Kane, J. Vidal and C.P. Yuan, *Phys. Rev.* **D39**(1989), 2617.
5. G. Couture and J. N. Ng, *Z. Phys* **C35**(1987), 65.
6. G. Couture *et al.*, *Phys. Rev.* **D36**(1987), 859.
7. T.M. Aliyev, *Phys. Lett.* **155B**(1985), 364; S. Alam, S.N. Biswas and A. Goyal, *Phys. Rev.* **D33**(1985), 168; G. Couture *et al.*, *Phys. Rev.* **D38**(1988), 860.
8. T.G. Rizzo and M.A. Samuel, *Phys. Rev.* **D35**(1987), 403; M. Suzuki, *Phys. Lett.* **153B**(1985), 289.
9. U. Baur, D. Zeppenfeld, *Phys. Lett.* **B201**(1988), 383.
10. A. Grau and J.A. Grifols, *Phys. Lett.* **B154**(1989), 283.
11. J.J. van der Bij, *Phys. Rev.* **D23**(1987), 1088.
12. R. Alcorta, J.A. Grifols, S. Peris, *Mod. Phys. Lett.* **A2**(1987), 23.
13. U. Baur and E. L. Berger, *Phys. Rev.* **D41**(1990), 1476.
14. J. Layssac *et al.*, Report No. PM/90-42 (1991).
15. E. N. Argyres *et al.*, *Phys. Lett.* **B259**(1991), 195.
16. D. Zeppenfeld, *Phys. Lett. B* **183**(1987), 380.
17. U. Baur and D. Zeppenfeld, *Nucl. Phys.* **B325**(1989), 253.
18. S. Zeppenfeld, Report No. OCIP-C-91-2 (1991).
19. U. Baur and D. Zeppenfeld, *Nucl. Phys.* **B308**(1988), 127.

20. R. D. Ruth, Report No. SLAC-PUB-5406 (1991).

21. We use machine design G from R. B. Palmer,
Ann. Rev. Nucl. Part. Sci. **40**(1990), 529.

22. P.B. Wilson, SLAC-PUB-3985 (1986);
R. Blankenbecler and S.D. Drell, *Phys. Rev.* **D36**(1987), 277;
P. Chen, in *Proceedings of the Workshop on Physics at Future Accelerators*,
La Thuile(Italy) and Geneva(Switzerland) CERN 87-07 (1987);
R. Blankenbecler and S.D. Drell, *Phys. Rev.* **D37**(1988), 3308.

23. D. V. Schroeder, Report No. SLAC-Report-371, 1990 (Ph.D. dissertation).

24. I. F. Ginzburg *et al.*, *Nucl. Instrum. Meth.* **205**(1983), 47;
I. F. Ginzburg *et al.*, *Nucl. Instrum. Meth.* **219**(1984), 5.

25. V. I. Telnov, *Nucl. Instrum. Meth.* **A294**(1990), 72.

26. I.F. Ginzburg *et al.*, *Nucl. Phys.* **B228**(1983), 285.

27. K.O. Mikaelian, *Phys. Rev.* **D30**(1984), 1115.

28. J.A. Robinson and T.G. Rizzo, *Phys. Rev.* **D33**(1986), 2608;
G. Couture, S. Godfrey and P. Kalyniak, *Phys. Lett.* **B218**(1989), 361.

29. E. Yehudai, *Phys. Rev.* **D41**(1990), 33.

30. G. Couture, S. Godfrey and R. Lewis, Report No. PRINT-91-0047 (1991).

31. E. Yehudai, Report No. SLAC-PUB-5495 (1991).

32. H. Aronson, *Phys. Rev.* **186**(1969), 1434.

33. D. Levinthal, F. Bird, R. G. Stuart and B. W. Lynn, CERN-TH-6094-91-REV.

34. A. Hsieh and E. Yehudai, Report No. SLAC-PUB-5576. The packages are available from the author upon request.

35. S. Wolfram, *Mathematica – A System for Doing Mathematics by Computer*
(Addison-Wesley, Redwood City, 1988).

36. L. D. Landau and E. M. Lifshitz, *Quantum Mechanics* (Pergamon Press, Oxford, 1977), pages 213-219.

37. C. Ahn, *et al.*, Report No. SLAC-329 (1988);
T. Barklow, *et al.*, to be published as a SLAC Report.

38. J. Steinberger, *Phys. Rep.* **203**(1991), 345 and references therein.

39. T. L. Barklow, Report No. SLAC-PUB-5364, 1990.

40. H. W. Fearing and R. B. Silbar, *Phys. Rev.* **D6**(1972), 471;
K. Hagiwara and D. Zeppenfeld, *Nucl. Phys.* **B274**(1986), 1.

41. R. Kleiss, W. J. Stirling, *Nucl. Phys.* **B262**(1985), 235.

42. *Reduce* by A. C. Hearn, see Reduce User's Manual, version 3.2, Rand Crop., 1985.

43. *Schoonship* by M. Veltman, see H. Strubbe, *Comp. Phys. Comm* **8**(1974), 1.

44. *Form* by J. A. M. Vermaseren, unpublished.

45. H. Murayama, I. Watanabe, K. Hagiwara, "HELAS: HELicity Amplitude Subroutines for Feynman diagram evaluations", to appear in KEK-Report.

46. *Maple* by Waterloo Maple Corp., see MAPLE Reference Manual, Fifth Edition, Waterloo Maple Publishing, 1988.

47. J. Küblbeck, M. Böhm and A. Denner, *Comp. Phys. Comm.* **60**(1990), 165.

48. R. Mertig, M. Böhm and A. Denner, *Comp. Phys. Comm.* **64**(1991), 345.

49. R. Kleiss, W. J. Stirling, *Nucl. Phys.* **B262**(1985), 235.

50. M. Veltman, *Nucl. Phys.* **B319**(1989), 253.